Kerstin Schmoltner, BSc

Ions in Organic Field-Effect Transistors – Fundamental, Fabricational and Sensing Aspects

MASTER THESIS

For obtaining the academic degree
Diplom-Ingenieurin

Master Programme of
Technical Physics

Graz University of Technology

Supervisor:
Ao.Univ.-Prof. Dipl.-Ing. Dr.techn. Emil J. W. List
Institute of Solid State Physics
in cooperation with:
NanoTecCenter Weiz Forschungsgesellschaft mbH
Graz, November 2010

Deutsche Fassung:
Beschluss der Curricula-Kommission für Bachelor-, Master- und Diplomstudien vom 10.11.2008
Genehmigung des Senates am 1.12.2008

EIDESSTATTLICHE ERKLÄRUNG

Ich erkläre an Eides statt, dass ich die vorliegende Arbeit selbstständig verfasst, andere als die angegebenen Quellen/Hilfsmittel nicht benutzt, und die den benutzten Quellen wörtlich und inhaltlich entnommene Stellen als solche kenntlich gemacht habe.

Graz, am ……. ……..
(Unterschrift)

Englische Fassung:

STATUTORY DECLARATION

I declare that I have authored this thesis independently, that I have not used other than the declared sources / resources, and that I have explicitly marked all material which has been quoted either literally or by content from the used sources.

……. ……..
date (signature)

Acknowledgement

First of all I would like to thank my supervisor Prof. Emil J. W. List for giving me the opportunity to work in his team on this interesting field of research and for his guiding ideas.

I would also like to thank Andreas Klug for his co-supervision and guidance, for fruitful discussions and intense cooperation within the whole work as well as for proof reading this thesis and especially for arousing my enthusiasms for OFETs.

Special thanks go to Karl Popovic for the support with inkjet-printing and Alex Blümel for several AFM measurements. Moreover I would like to thank the group of Prof. Slugovc for providing the novel polymer dielectric materials, the group of Prof. Müllen and the group of Prof. Fumio for providing the organic semiconducting materials. For financial support the research project cluster ISOTEC (RP DEVFAB) is acknowledged.

Futhermore I would like to thank Gerhild Wurzinger, who supported me with the first fabrications and measurements of OFETs and Sonja Larissegger and Stefan Sax for their support. I also have to thank the people that share the office with me, in particular Sebastian Nau and Johannes Kofler for great discussions and a great time during this thesis. Moreover I would like to thank the whole team of the NanoTecCenter Weiz Forschungsgesellschaft mbH for the great collaboration and their assistance.

I want to thank also my parents and my sister for their love and continuous encouragement as well as my grandparents for their support. Last but not least I would like to thank Roland for his tremendous support, his understanding, and his endless love.

Abstract

Organic field-effect transistors (OFETs) offer a great deal of promise for chemical and biological sensing. Concerning their fabrication, many organic compounds are solution-processable at low temperatures on a variety of substrates. This allows for cost-effective fabrication methods, leading to smart (disposable) sensors for applications in health-, food- and environmental monitoring and diagnostics. Moreover, organic (semiconducting) materials can be tailored with respect to their chemical and physical properties, being another important advantage for analyte detection. Besides the evaluation of novel organic semiconductors in OFETs, one focus of this work concentrated on OFETs as transducers for ions. Therefore the effects of mobile ions on the device performance of poly(3-hexylthiophene)-based OFETs in bottom-gate architecture were investigated by deliberately adding ions to the semiconductor. In detail, poly(3-hexylthiophene) was blended with dibenzo-18-crown-6 as ion conductor and sodium trifluoromethanesulfonate as salt. The underlying mechanisms for the observed source-to-drain channel current drifts upon bias stress were attributed to electric double layer formation at the electrodes and/or electrochemical doping. Moreover, the influence of ions was thoroughly studied, when polymer electrolyte dielectrics including polyvinyl alcohol and a novel polymer functionalized with dibenzo-18-crown6 were applied in top-gate/bottom-contact OFETs. Within this frame various polyvinyl alcohol grades and the novel dielectric polymer material were also electrically characterized in capacitor structures. In addition, well-performing OFETs with inkjet-printed silver source/drain electrodes were fabricated after proper process optimization and compared with corresponding devices based on evaporated gold source/drain electrodes. Finally ionic drifts were also investigated with flexible top-gate/bottom-contact OFETs including inkjet-printed source/drain electrodes.

Kurzfassung

Organische Feldeffekt-Transistoren (OFETs) stellen vielversprechende Bauelemente im Bereich chemische und biologische Sensor-Anwendungen dar. Hinsichtlich der Herstellung sind organische Substanzen auf einer Vielzahl von Substraten aus der Lösung bei niedrigen Temperaturen prozessierbar. Dies ermöglicht eine kostengünstige Herstellung von intelligenten (Einweg-) Sensoren für Anwendungen in der Medizin-, Lebensmittel- und Umweltüberwachung wie auch in der Diagnostik. Weiters können organische Materialien in Bezug auf ihre chemischen und physikalischen Eigenschaften maßgeschneidert werden, was einen weiteren wichtigen Vorteil für die Detektion von Analyten darstellt. Neben der Untersuchung von neuartigen organischen Halbleitern in OFETs beschäftigte sich ein Schwerpunkt dieser Arbeit mit OFETs als Signalumwandler für Ionen. Folglich wurden die Effekte von mobilen Ionen auf die Bauteilfunktion von Poly(3-hexylthiophen)-basierenden OFETs mit „Bottom-Gate"-Architektur untersucht, wobei Ionen gezielt dem organischen Halbleiter hinzugefügt wurden. Im Einzelnen bestand die verwendete aktive Schicht aus Poly(3-hexylthiophen) gemischt mit dem Ionenleiter Dibenzo[18]Krone-6 und dem Salz Natrium Trifluoromethansulfonat. Die zugrundeliegenden Mechanismen für die beobachten Drifts des Kanalstroms unter Spannung wurden der Bildung einer elektrischen Doppelschicht bei den Elektroden und/oder dem elektrochemischen Dotieren zugeordnet. Darüber hinaus wurde der Einfluss von Ionen in „Top-Gate/Bottom-Contact" OFETs mit polymeren elektrolytischen Dielektrika, nämlich Polyvinylalkohol und einem neuartigen Polymer funktionalisiert mit Dibenzo[18]Krone-6, untersucht. In diesem Zusammenhang wurden verschiedenartige Polyvinylalkohole wie auch das neuartige dielektrische Polymer in Kapazitätsstrukturen elektrisch charakterisiert. Weiters wurden leistungsfähige OFETs mit inkjet-gedruckten Silber Source/Drain-Elektroden nach entsprechender Prozessoptimierung hergestellt und mit OFETs basierend auf aufgedampften Gold-Elektroden verglichen. Schließlich wurden ionische Drifts auch in flexiblen „Top-Gate/Bottom-Contact" OFETs mit inkjet-gedruckten Source/Drain-Elektroden untersucht.

Content

1 Fundamentals

1.1 Organic Semiconductors

More than 80% of all known chemical compounds are of organic nature. In general organic materials are referred to as carbon-containing compounds with constituting elements like hydrogen, oxygen, nitrogen, sulfur, phosphor, but also halogens (fluorine, chlorine, bromine) and metals can be involved. Until the pioneer work of Friedrich Wöhler 1828 with the synthesis of urea it was believed that organic substance can only be formed by the "vital force" in living organisms.[1] Nowadays organic materials can be found in numerous applications in our everyday's life as a result of their specific mechanical, optical and electrical properties. The intriguing discovery of electrical conductivity can be traced back to the beginning of the 20th century, when the photoconductivity of anthracene crystals was reported.[2] Nevertheless, until the 1950s there was only little interest, which changed by several reports of investigations of semiconducting properties of different organic substances.[3,4] Another milestone was set by the discovery of the high electrical conductivity of doped polyacetylene by Hideki Shirakawa, Alan G. Mac.Diarmid, Alan J.Heeger and co-workers in 1977.[5] This work induced a lot of research in the field of organic electronics and was awarded with the Nobel Prize in Chemistry in the year 2000. Today the applications of organic semiconductors are ranging from light-emitting diodes[6], field-effect transistors[7,8], light-emitting electrochemical cells[9] , solar cells[10], organic photodiodes to organic lasers.[11]

Organic semiconductors are van der Waals bonded solids which consist of either conjugated polymers or small molecules. Examples of some organic semiconductors are depicted in Figure 1.1.

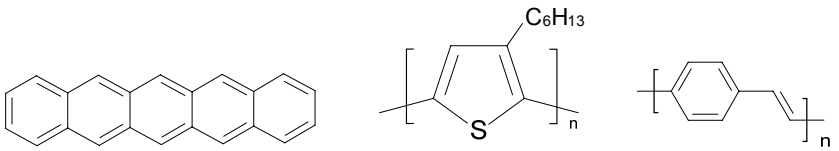

Figure 1.1: Chemical structure of pentacene (left), regioregular poly(3-hexylthiophen) (rr-P3HT) (middle), polyparaphenylenevinylene (right).

Carbon as the central element in organic chemistry can be found in the 4th main group in the periodic table of elements comprising 4 electrons in the outermost electron shell. The electronic configuration of carbon in its ground state is $1s^2 2s^2 2p^2$, where two electrons of the 2p orbital are unpaired (see Figure 1.2). The energy difference between the 2s and the 2p state is small so that an electron can be easily transferred from the 2s orbital to the unoccupied 2p state, resulting in four

energy levels to form chemical bonds (see Figure 1.2, middle). According to the involved orbitals (one, two or three p-orbitals), either a sp-, sp^2 or sp^3 hybrid orbital can be formed.

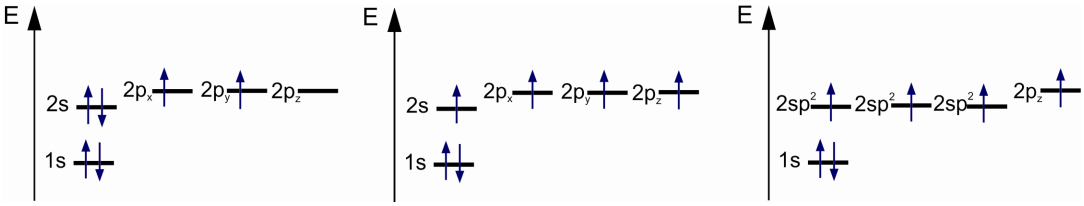

Figure 1.2: Electronic configuration of atomic carbon in its ground state ($1s^2 2s^2 2p^2$, left), excited state (middle) and in sp^2-configuration.

This concept of hybridization was introduced by L.C. Pauling. The sp^2-hybridization of carbon is the base of alkene molecules (C_nH_{2n}) and is very important for organic semiconductors. Here the 2s orbital is linearly combined with two 2p orbitals, forming two sp^2-hybrid orbitals and the third 2p orbital remains unaltered (see Figure 1.3). These sp^2-hybrid orbitals form covalent σ-bonds and the unaltered p_z orbitals form π-bonds by overlapping, leading to a double bond. This double bond exhibit shorter bond length in comparison to the single bonds. Figure 1.3 (right) depicts the molecular structure of ethylene (C_2H_4).

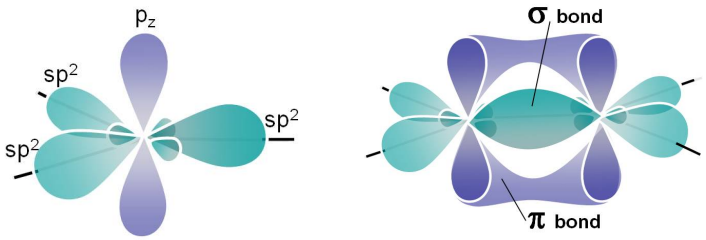

Figure 1.3: sp^2-hybridization (left) and chemical bonding in ethylene (right) (taken from [12] and modified).

Conjugated polymers exhibit alternating single and double bonds between the carbon atoms, where the π-electrons are highly delocalized due to overlapping of the orbitals along the chain. A famous example is the aromatic hydrocarbon benzene, shown in Figure 1.4. All semiconducting organic materials are conjugated π-systems, where the Peierls distortion[13] leads to an alternation between single and double bond length and hence an energy gap between the filled π-band and an empty π^*-band. In contrast, carbon atoms with sp^3-hybridization exhibit no delocalized π-electrons, thus making these materials electrically insulating with large band gaps. In organic semiconductors the **h**ighest **o**ccupied **m**olecular **o**rbital of the π-band is called HOMO level, whereas the **l**owest **u**noccupied **m**olecular **o**rbital in the π^*-band is called LUMO.

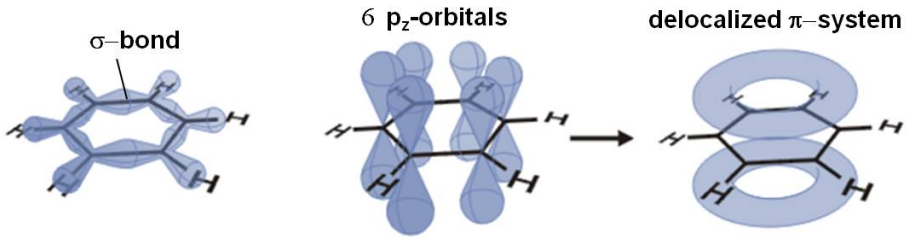

Figure 1.4: Formation of a delocalized π-electron system by overlap of the p orbitals in a benzene molecule (taken from [14] and modified).

1.1.1 Excited States

There is a large difference in charge carrier transport as well as in the excited states found in organic semiconductors compared to their inorganic counterparts. This is a result of different bonding forces. While the latter (e.g. Si, Ge) form strong covalently bonded lattice structures and reveal delocalized excited states, the organic solids are bound by weak van der Waals forces, which results in localized states along the polymer chain due to associated structural relaxation. There are different charge carriers such as excitons, polaron, bipolarons and solitons, which can move as quasi-particles along the polymer chain or between macromolecules. Solitons can only be formed in conjugated polymers with degenerated ground states. This is the case when the total energy of the ground state does not alter by interchanging single and double bonds. They are usually generated during synthesis when two structures are combined with different bond order. However, most used polymers in organic electronics have a non-degenerated ground state.

1.1.1.1 Polarons and Bipolarons

In such non-degenerated polymers the charge carriers are not solitons but polarons and bipolarons. A polaron is formed when an electron is added to the lowest occupied orbital in the π^*-band (LUMO) or removed from the highest unoccupied molecular orbital of the π-band (HOMO) with an accompanied structural deformation of the chain around the charge. This happens when the decrease of the electronic energy is higher than the elastic energy needed for the deformation of the lattice, yielding to a minimum of the total energy. The involved charges (electrons or holes) are interacting with the lattice and are therefore not free but localized (electron-phonon coupling). Corresponding to their charge $\pm$e, either a positive or a negative polaron is formed, exhibiting a spin of $\pm 1/2$ (see Figure 1.5). Moreover, if two charges are involved, a bipolaron is formed with zero spin. The polarons generate electronic states within the $\pi\pi^*$-gap between LUMO and HOMO. By adding more electrons (holes) to the polymer chain (e.g. by doping) energy bands within the gap can be created. For a more detailed description see also Ref. [13],[15].

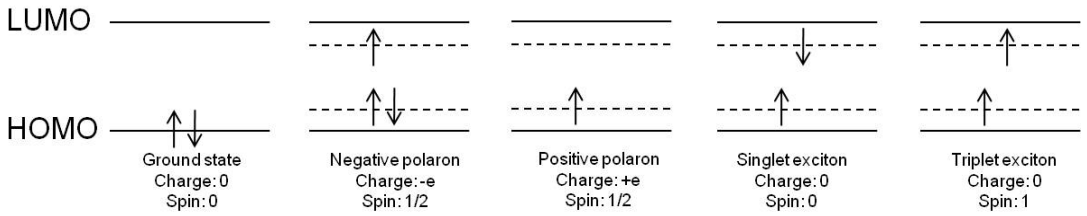

Figure 1.5: Energy levels of the ground state, the negative and positive polaronic states and the singlet/triplet excitonic states of organic semiconductors.

1.1.1.2 Excitons

Excitons are another important type of excited states in organic semiconductors, especially in OLED application, where the recombination of a hole and an electron leads to emission of a photon. Basically an electron-hole pair is generated by transferring an electron from the HOMO to the LUMO, leaving a hole in the HOMO. This electron-hole pair is bound by Coulomb interaction and forms a neutral quasi-particle, the exciton, which can move as entity. This excitation is also accompanied by a structural relaxation and can be induced by absorption of a photon or by the injection of a positive and negative polaron. Excitons can extend over several monomer units. Such small radius excitons, so-called “Frenkel excitons” are usually localized on the same molecule and are mainly found in organic materials. In contrast, “Wannier-Mott” excitons are more delocalized, exhibiting intermolecular character and are usually observed in inorganic materials. Depending on the electronic configuration the excitons exhibit a spin of zero (singlet) or one (triplet) (see Figure 1.5).

1.1.2 Charge Carrier Transport

The charge carrier transport in a material is strongly related to its electrical conductivity σ. The electrical conductivity is defined as the product of the density of mobile charge carriers (electron density n; hole density p) and the charge carrier mobility μ times the elementary charge e:

$$\sigma = en\mu_n + ep\mu_p \tag{1.1}$$

In contrast to metals the conductivity of semiconductors is increasing with increasing temperature due to excitation of an increased number of charge carriers from the valence to the conduction band. Moreover, charge carriers can be added to the π-backbone by several doping mechanisms, such as charge injection, light exposure, chemical and electrochemical doping, leading to (semi)-conducting properties.

In organic semiconductors one of the most important parameter for describing the charge transport is the charge carrier mobility, which is given by:

$$\mu = \frac{|\vec{v}|}{|\vec{E}|} \tag{1.2}$$

with $|\vec{v}|$ as the average drift velocity and $|\vec{E}|$ as the electric field. This equation is only valid as long as the applied electric field is small. Otherwise when the electric field is increasing the drift velocity tends to saturate due to scattering effects at impurities, phonons or other charge carriers. In comparison to inorganic semiconductors the mobilities (μ ~ 1000 cm^2/Vs for silicon at room temperature) found for organic semiconductors are much smaller (μ ~ 15 cm^2/Vs for rubrene).[16] Another approach to obtain the charge carrier mobility is by applying Newton's law and considering that a charge carrier (charge q, effective mass m^*) is scattered after a time τ:

$$\mu = \frac{q\tau}{m^*} \tag{1.3}$$

Experimentally the charge carrier mobility can be determined among other techniques by time of flight measurements (TOF), Hall measurements, field-effect measurements and space charge limited current measurements.[13]

$$\mu = \frac{|\vec{v}|}{|\vec{E}|} \tag{1.4}$$

Through several doping mechanisms charges can be generated and transported in form of quasi-particles, e.g. polarons. However there is a difference in the charge carrier transport between conjugated materials and inorganic single crystal semiconductors. The latter exhibits band transport in wide energy bands (valence and conduction band) formed by strong covalent forces on the basis of the inverse power law of mobility on temperature, whereas organic semiconductors are bonded

by weak van der Waals forces leading to wide band gaps and narrow energy bands. Nevertheless it was found that the charge carrier mobility in ultra pure organic single crystal also decreases with increasing temperature. This is explained by the theory of polaronic transport[7], where for low temperature delocalized charge carriers are assumed to move in bands. When the temperature is increasing the electron-phonon interaction becomes stronger and a so called “large polaron” is formed. This results in a narrowed band gap and the mobility decreases with increasing temperature. At even higher temperature a so called “small polaron” is formed, where the charge transport is dominated by phonon-assisted hopping between neighboring sites.

The charge transport mechanisms in organic semiconductors strongly depend on the degree of order. Although the progress in the field of organic electronics during the last three decades is impressive, the topic of charge transport remains controversial. There exist several models to describe the charge transport in different systems.

In polycrystalline structures, which are found in thin films of small molecules, the charge transport depends on the size and morphology of the crystallites separated by grain boundaries. The charge transport in such materials can be described by the multiple trapping and release model (MTR)[17] and the grain boundary model (GB)[18]. First predicts a thermal activated mobility and suggests that charges can move in narrow delocalized band but can be trapped in localized trap states formed by structural or chemical defects. The effective mobility is then determined by the trapping and releasing of the charges. However, this model could not explain the often observed temperature dependence of the mobility at low temperatures, which led to the development of the GB model. This model assumes that the grains are trap free, whereas the grain boundaries exhibit a high trap density. At very low temperature the charge transport mechanism is explained by tunneling across the grain boundaries, which is temperature independent but at intermediate temperature the tunneling is thermally activated. For high temperature the charge carriers can overcome the energy barrier at the grain boundaries due to thermal excitation.

Models for the charge transport in disordered organic semiconductors, which basically comprise conjugated polymer films, are based on hopping transport between localized sites. For these materials the mobility usually increases with increasing temperature. For example one model was developed by Vissenberg and Matters[19] which assumes variable range hopping in an exponential distribution of traps states. This model describes a thermally activated mobility and also accounts for the dependence of the mobility on the gate voltage.

1.2 Organic Field-Effect Transistors and Sensing Applications

In 1925 Julius Edgar Lilienfeld first proposed the theoretical description for field-effect transistors (FETs), which was realized by Oskar Heil in 1934, who fabricated the first FET. Nowadays these devices constitute one of the most important devices in modern electronics, including metal-insulator-semiconductor FET (MISFET), metal-semiconductor FET (MESFET) and thin film transistors (TFTs). For the latter most commonly amorphous hydrogenated silicon (a-Si:H) is used as inorganic semiconductor, whereas silicon, germanium and galliumarsenide are applied for MESFETs and MISFETs. In correspondence to findings in the field of organic semiconductors, organic field-effect transistors where introduced on an adopted TFT concept. Until 1987, when Koezuka et al. first reported on OFETs based on polythiophene, these devices were considered for having only little potential. Due to intense studies, these days OFETs are comparable with a-Si:H TFTs, which find their applications as drivers in large area flat panel displays. In literature various examples for applications of OFETs are reported e.g switching devices in active matrix flat panel displays[20], in large area applications, electronic papers (e-paper),[21,22] in printed logic circuits for RFID tags[23] etc. Besides the target applications as switching devices, OFETs are also promising devices for sensing applications, thus the integration of OFET-based sensors with organic electronics will open new opportunities for enabling cheap reliable sensor tags.

1.2.1 OFET – Device Architectures

OFETs are usually fabricated as thin film transistors (TFTs), since these devices operate in accumulation regime and too thick semiconducting layer would result in high off-currents. Different OFET architectures are depicted in Figure 1.6:, including the bottom-gate structure (or inverted staggered configuration) and the top-gate structure (or staggered configuration).

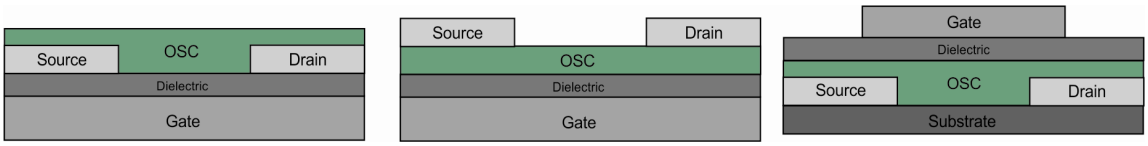

Figure 1.6: bottom-gate/bottom-contact architecture (left); bottom-gate/top-contact architecture (middle), top-gate/bottom-contact architecture (right).

For the bottom-gate/bottom-contact (BG/BC) architecture the source/drain electrodes are directly structured on the dielectric layer, which can be done for example with the well-estabilshed photolithographic techniques, yielding highly defined channels. This is followed by the deposition of the organic semiconductor, which can be done for solution processable compounds by means of spin-casting, drop-casting or inkjet-printing. In contrast the bottom-gate/top-contact (BG/TC) structure, where the semiconductor is directly applied on the dielectric layer followed by the

deposition of the source/drain electrodes on top, exhibit very homogeneous films in comparison to the BG/BC structure where the film morphology near the electrodes can differ from that within the channel.[24] This leads to a better device performance for BG/TC OFETs. Another architecture, which was also used within this thesis, is the top-gate/bottom-contact structure, where the source/drain electrodes are structured on a substrate. The deposited organic semiconductor is covered by the dielectric layer, which is then followed by the deposition of the gate electrode. For this architecture the semiconductor is encapsulated by the dielectric and not direct exposed to the environment. Moreover the use of functionalized dielectrics enables possible sensor applications.[25]

1.2.2 Working Principle

Basically the conductivity of the organic semiconductor, which is situated between the source and the drain electrode, is influenced by the electric field at the so called gate electrode. In particular, by applying a voltage at the gate electrode (V_G) charge carriers are injected from the electrodes into the organic semiconductor, which accumulate at the interface to the dielectric, forming a conductive channel (see Figure 1.7, example for p-type semiconductor). Upon applying a voltage between source and drain (V_D) a current is flowing across the channel. Hence by varying the electric field across the dielectric layer the device can be switched between an "on" and "off" state, for which ideally no current is needed, leading to very low power consumption. In contrast to MISFETs and MESFETs, OFETs are operating in accumulation regime, thus charge carriers which are responsible for the off-current conduction and the on-current are from the same type. By increasing the drain voltage V_D to values larger than the applied gate voltage V_G, a depletion region is formed near the drain contact and the source-to-drain current saturates. Figure 1.7 (bottom) illustrates the operation in saturation regime and the corresponding pinch off of the channel.

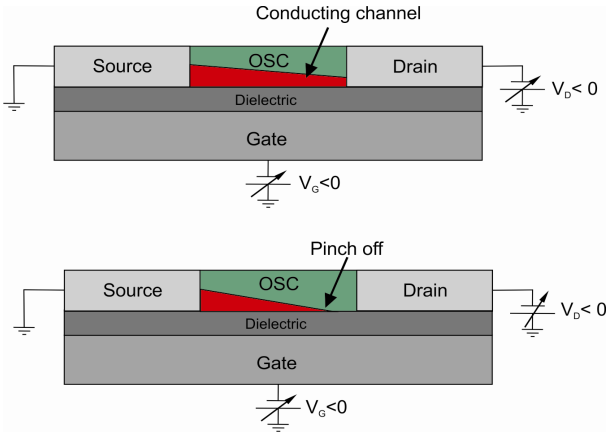

Figure 1.7: Scheme of OFET operating in linear regime ($|V_D|<|V_G-V_{th}|$, top) and in saturation regime ($|V_D|>|V_G-V_{th}|$, bottom); for p-type semiconductor.

In a rough approximation an OFET is operating in the linear regime when $|V_D|<|V_G|$ and in saturation regime when $|V_D|>|V_G|$. A model for the theoretical description of OFETs operating in these two regimes was proposed by Horowitz et al.[26] This model is based on the gradual channel approximation (GCA) developed by Schockley in the year 1961.[27,28] It states that the charge density related to a variation of the lateral field F_x within the field is much smaller than that related to a variation of the vertical field F_y, i.e. $\frac{\partial F_x}{\partial x} \ll \frac{\partial F_y}{\partial y}$. Hence the channel potential changes gradually and therefore only slightly over a distance of the insulator thickness d_i. This requires that the inslutator thickness is much smaller than the channel length L ($d_i<<L$). Moreover, this model does not consider the influence of contact resistance, which leads to a dependence of the mobility on the channel length L. The gate and drain voltage dependence of the mobility is also not taken into account within this model. Nevertheless the derived equations are often used to quantify the OFET performance.

For the linear regime ($|V_D|<<|V_G|$) the source-to-drain current is described by equation (1.5) and shows that for small V_D a linear dependence of I_{Dlin} on V_D is obtained, since the quadratic term can be neglected.

$$I_{Dlin} = \frac{W}{L}\mu_{FE}C_i\left[(V_G - V_{th})V_D - \frac{V_D^2}{2}\right] \tag{1.5}$$

W…channel width, L…channel length, μ_{FE}…field-effect mobility, C_i…capacitance per unit area of the dielectric, V_{th}…threshold voltage

For the saturation regime ($|V_D|>|V_G|$) the source-to-drain current can be calculated from:

$$I_{Dsat} = \frac{W}{2L}\mu_{FE}C_i(V_G - V_{th})^2 \tag{1.6}$$

Figure 1.8 illustrates the dimensions of the channel, namely the channel length L and the channel width W. According to equation (1.5) and (1.6) small L and large W are desirable for low voltage operation, whereupon for too small L the gradual channel approximation is not valid leading to short channel effects.[29]

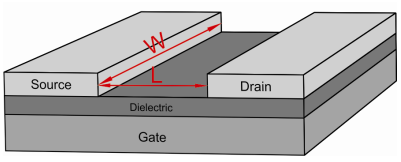

Figure 1.8: Dimensions of a device: channel length (L) and channel width (W).

1.2.3 Sensing Applications and OFET Device Parameters

Organic field-effect transistors (OFETs) offer a great deal of promise for chemical and biological sensing. Concerning their fabrication, many organic compounds are solution-processable at low temperatures on a variety of substrates. This allows for cost-effective fabrication methods, leading to smart (disposable) sensors for applications in health-, food- and environmental monitoring and diagnostics. This aspect, together with a unique property of organic compounds that they can be tailored with respect to their chemical and physical properties makes them attractive for future sensing applications, since high sensitivity and selectivity toward an external chemical stimulus can be obtained due to functionalizing of the active layer. This sensitive part can comprise one of the layers that form the device. Besides the determining sensor parameters sensitivity and selectivity, the response time, reliability and detection range are also important. The switching speeds are usually rather low, since many organic semiconductors are affected by low mobility. However, this doesn't lower the potential of OFETs for sensing applications, because many sensing events happen on the order of seconds. Moreover the detection limit and sensitivity also benefits from the inherent signal amplification, being another advantage in comparison to chemiresistors or other amperometric and potentiometric sensors. Furthermore, the fact that the operation of an OFET is influenced by the chemical ambient, namely oxygen and humidity, has conveniently turned into an advantage by using it for oxygen or humidity sensor applications.

In addition, it is possible to simultaneously extract different parameters such as mobility, switch-on voltage, on-currents etc. from the electrical characterization of an OFET, being directly correlated to the identification of a chemical species in an analyte (see Figure 1.9).

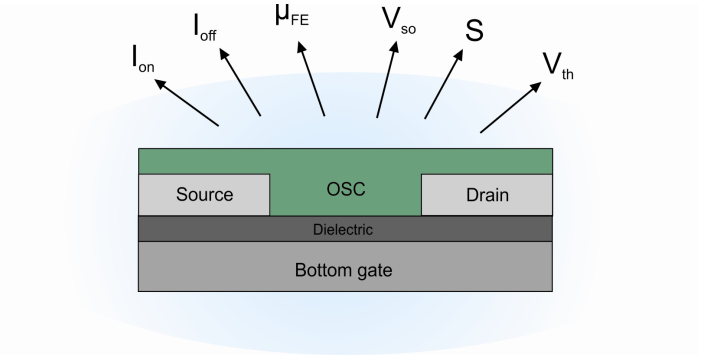

Figure 1.9: Scheme of a BG/BC OFET, illustrating the different parameter which can be extracted from the device characteristics.

Basically the electrical characterization of an OFET reveals two important characteristics, namely the transfer and the output characteristics, from which the following device parameters are extracted. The transfer characteristics of an OFETs are obtained by measuring the source-to-drain channel current for constant drain voltage values V_D while sweeping the gate voltage V_G. Figure

1.10 (left) shows the corresponding transfer curves, where forward and reverse sweep are recorded, to investigate the operational stability. Accordingly the output curves are recorded by sweeping the drain voltage V_D for various fixed gate voltages V_G. In Figure 1.10 (right) the linear ($|V_D| << |V_G|$) and the saturation regime ($|V_D| > |V_G|$) become obvious.

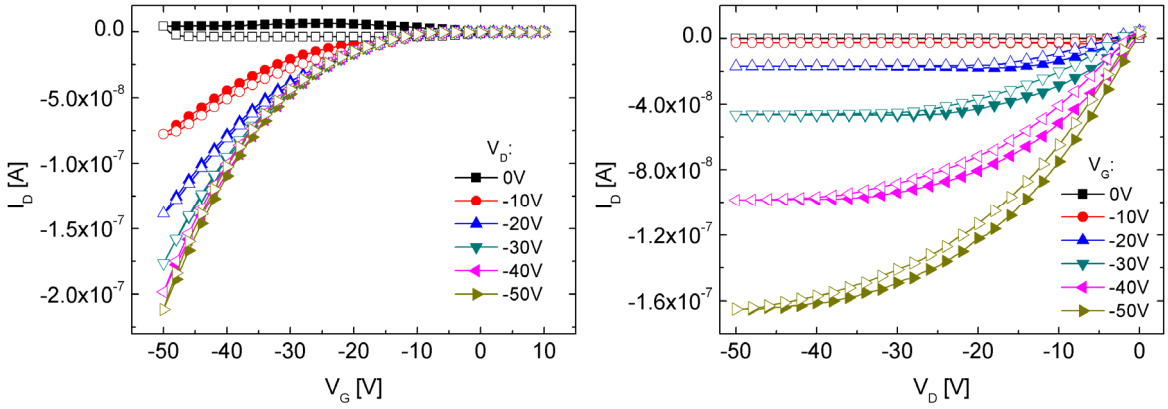

Figure 1.10:Transfer (left) and Output (right) characteristics of an rr-P3HT based OFET (L ~ 25 µm, W ~ 2.85mm).

Regarding sensing applications of OFETs, a sensor is obtained when an analyte affects one of the layers of the device and results in a variation of one or more of the electronic parameters, that can be extracted from the device characteristics. In the following these device parameters are described.

1.2.3.1 Field-Effect Mobility

The equations of the field-effect mobility in the linear and the saturation regime can be derived from equation (2.1) and (2.2) to:

$$\mu_{lin} = \frac{L}{WC_iV_D}\left(\frac{\partial I_D}{\partial V_G}\right)_{V_D=const} \tag{1.7}$$

$$\mu_{sat} = \frac{2L}{WC_i}\left(\frac{\partial\sqrt{I_D}}{\partial V_G}\right)^2_{V_D=const} \tag{1.8}$$

Since these equations are based on the model presented above, the dependence of the mobility on the temperature and on the gate voltage is not considered. Moreover the contact resistance is also not taken into account. Nevertheless the mobility values obtained from these equations are good estimates to compare the device performance and were also used within this thesis.

1.2.3.2 Threshold Voltage

For inorganic MISFETs the threshold voltage is an important device parameter and is defined as the voltage needed for the onset of strong inversion. However, OFETs operate in accumulation regime and therefore this concept of threshold voltage cannot be applied. Nevertheless the

threshold voltage is extracted as a fit parameter from the transfer curves. It is obtained from the intersection of the linear fit of the absolute value (linear regime) or the square root of the source-to-drain current I_D (saturation regime) with the V_G axes (see Figure 1.11). The threshold voltage strongly depends on the quality of the semiconductor/dielectric interface, therefore different surface modifications e.g. self-assembled monolayer can be applied, to change the threshold voltage.

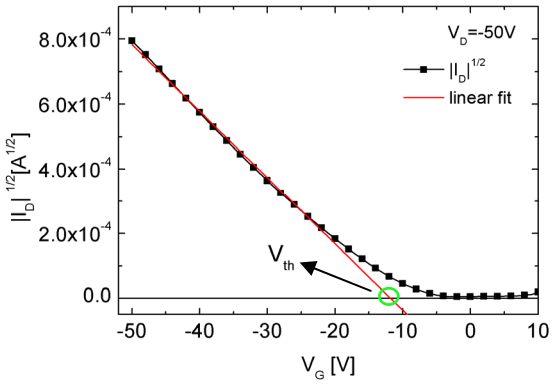

Figure 1.11: Linear fit of the square root of the source-to-drain current to obtain the threshold voltage V_{th}.

1.2.3.3 Switch-On Voltage and Subthreshold Solpe

Since the threshold voltage is only a fit parameter, Meijer et al. introduced the switch-on voltage V_{so}, below which the variation of the channel current with V_G is zero but increases with $V_{so}>V_G$. The switch-on voltage represents the gate voltage at which all traps are filled and the conducting channel starts to form. It can be extracted from the semilogathmic transfer curve, illustrated in Figure 1.12.

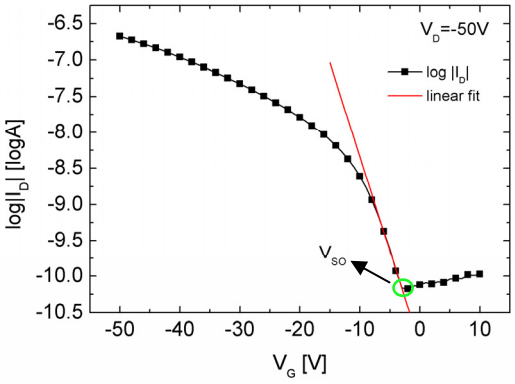

Figure 1.12: Semilogarithmic transfer curve to obtain the switch-on voltage and the subthreshold slope by liner fit in the subthreshold regime.

Moreover form the semilogarithmic transfer curve, the subthreshold slope S in V/decade can be obtained from the inverse slope of the linear fit of $\log|I_D|$ vs V_G in the subthreshold regime. It is a measure of how much gate voltage has to be applied in order to increase I_D to one decade. Small S

values are favorable, because the steeper the subthreshold solpe is, the faster the switching happens. Figure 1.12 illustrates the extraction of S, which can be calculated by:

$$S = \frac{dV_G}{d(\log I_D)} \tag{1.9}$$

Altering S values can indicate changes in the doping or trapping density and it is strongly related to the quality of the semiconductor/insulator interface. S can be used to obtain an estimation for the maximum interface trap density N_{max}^{IF}, with the assumption that the density of the deep bulk state and the interface states are independent of energy:

$$N_{max}^{IF} \approx \left[\frac{S \cdot q \cdot \log(e)}{kT} - 1\right] \cdot \frac{C_i}{q} \tag{1.10}$$

S…subthreshold slope, e…Euler's constant, k…Boltzmann's contant, T…temperature, C_i…insulator capacitance per area, q…elementary charge

1.2.3.4 On/Off-Current Ratio

The on-current I_{on} is given by the source-to-drain current in on state at high gate and drain voltages, whereas the off-current I_{off} is defined as the source-to-drain current at high drain voltages but zero gate voltage $V_G = 0$ V. The on/off-current ratio I_{on}/I_{off} is obtained by the ratio of the channel currents in the on state to the corresponding off state. For well-performing OFETs the on/off-current should be on the orders of ~10^6.

1.2.3.5 Contact Resistance

According to the charge carrier movement, including the injection from the source into the semiconductor channel, the migration across the channel and the extraction form the channel into the drain, the corresponding resistances in series can be grouped in contact resistance R_p and channel resistance R_{ch}, yielding the total device resistance R_{on}:

$$R_{on} = R_p + R_{ch} \tag{1.11}$$

In an ideal OFET this contact resistance is ohmic, meaning that e.g. for a p-type semiconductor the work function of the contact is higher than that of the organic semiconductors. In reality not for all material combination this condition can be met, leading to the formation of injection barriers. Besides the correlation of the contact resistance to the work function difference and the barrier height and width, the contact resistance also depend on the morphology of the materials, trap concentrations, doping level near the interface, interfacial dipole layers, chemical and physical reactions near the interface region, temperature and sample geometry. Moreover the contact resistance decreases with increasing gate voltage due to higher charge carrier densities near the

semiconductor/metal interface. Nevertheless the relative influence of the contact resistance might increase with increasing gate voltage since the channel resistance also decreases due to higher mobilities at high V_G. The determination of the device parameters, considering also the contact resistance can be done by means of transfer line method (TLM)[30] and gated-four measurements.[15]

1.2.4 Examples of OFETs in Chemical Sensing Applications

In literature several OFET-based sensors are reported with applications ranging from chemical vapor sensors to transducers for ions and biological substances.[31,32] Chemical sensors based on OFETs were demonstrated for different gases such as N_2, O_2,[33] NO_2[34] or organic vapors[35] like alcohols. For these sensors the semiconducting layer is used as sensitive part and mostly bottom-gate architecture is used to ensure the direct contact of the semiconductor with an analyte. The OFET gas sensors have several advantages compared to the conventional chemiresistors, including that more information of a particular analyte is obtained since changes in several device parameters are monitored (bulk and field-induced conductivity, threshold voltage, field-effect mobility).[36] Moreover OFET sensors exhibit an inherent signal amplification which leads to enhanced sensitivity and signal to noise ratios. In general, the transduction of the chemical signal occurs when the interaction of the analyte with the sensing layer changes the channel current. Basically there are three regions where an analyte can influence the OFET performance: The semiconducting bulk, where a modulated conductivity occurs or changes in mobility are caused by interaction with the analyte; the semiconducting/dielectric interface, where modified conductivities are a result of chemical reaction of molecules such as H_2O or alcohols; and the semiconducting/electrode interface, where modulated contact resistance lead to the sensing effect.

Furthermore pH-senstive OFETs have been demonstrated by several groups. [37] These ion-sensitive OFETs belong to the big group of ion sensors and will be discussed in detail in the following section. In the contrast to the mentioned gas sensors, for these devices the gate dielectric is used as sensitive layer.

1.2.4.1 Ion-Sensitive Organic Field-Effect Transistors (ISOFETs)

The idea to use field-effect transistors (FETs) as pH sensors first came up independently by Bergveld and Matsuo et al. in the early 1970s. Nowadays applications of conventional ion-sensitive field-effect transistors (ISFETs) manufactured by CMOS technology on silicon can be found in medical diagnostics, environmental and food quality control.[38] Considering a conventional MOSFET device architecture, for ISFETs the gate electrode is removed and the gate insulator is directly exposed to the electrolyte solution (see Figure 1.13). The detection mechanism is based on

the change of the potential drop across the dielectric/electrolyte interface modifying the channel current, when pH values change. The development of ISFETs for detection of other ions followed the path of the already well established ion selective electrodes (ISE)[39], where ion selective membranes are the key component of such devices. Few years after the introduction of ISFETs, ion selective membranes were also directly placed on the gate dielectric (Moss et al. 1975)[40], enabling sensing application for ions other than H^+.

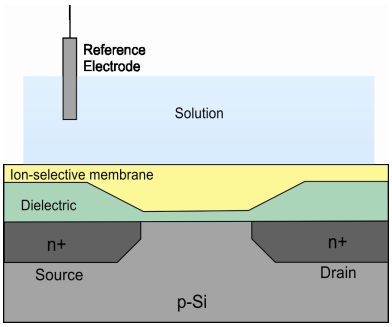

Figure 1.13: Schematic representation of an ISFET.

Nevertheless ISFETs based on inorganic semiconductors exhibit limiting factors for practical applications such as high fabrication cost and long-term stability problems. For many applications disposable sensors are desirable as much as compatibility with flexible substrates and biocompatibility. All these requirements can be met by the use of organic field-effect transistors for sensing.

The first ion-sensitive organic field effect transistor (ISOFET) for pH-sensing was developed by Bartic et al in 2000.[37] Similar to ISFETs the dielectric layer is in direct contact with an aqueous solution and a reference electrode (Ag/AgCl) is used as gate. The electric field across the insulating gate dielectric is influenced by the ions at the electrolyte/insulator interface, thus modulating the channel current. By applying a voltage to the Ag/AgCl electrode and monitoring the source-to-drain current it was possible to receive a stable and reproducible pH-dependent response. This first ISOFET prototype consists of poly(3-hexylthiophene) P3HT as semiconductor and silicon nitride (Si_3N_4) as proton sensitive layer exposed to the solution (see Figure 1.14).

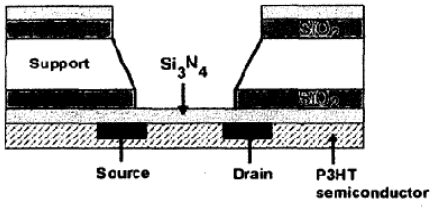

Figure 1.14: Schematic representation of the device configuration of a pH sensitive OFET (taken from [37]).

Furthermore, a simple glucose biosensor was realized based on a pH-sensitve OFET.[41] Here tantalium oxide was used as dielectric layer with an immobilized enzymatic layer of glucose oxidase. The pH values were shown to change upon conversion of the immobilized glucose oxidase to gluconic acid, leading to an increased proton concentration at the dielectric surface.

Gao et al. proposed a disposable ISOFET on a polymer mechanical support with integrated reference electrode and integrated microfluidic system to measure pH changes, enabling the integration to lab-on-a-chip platforms. Besides the use of inorganic dielectrics as proton sensitive layers, sensing of pH variations with OFET based on Mylar® foils as sensitive layer and mechanical support was demonstrated.[42]

In general, the selectivity towards a certain analyte can be induced by modifying the gate dielectric with a proper functionalization e.g. with an ion-selective membrane for certain ion detection or with enzymatic layers. Moreover, chemical sensitive FETs with incorporated layers of antibodies or antigens, or even with whole tissues layers and DNA oligonucleodites were reported.[32,43]

Aside from OFETs, also organic electrochemical transistors (OECTs) find their application in biosensing but exhibit significant lower switching speeds. In OFETs the source-to-drain current is modulated by field-effect doping, whereas in OECTs the source-to-drain current is modulated by electrochemical doping or de-doping. OECTs are composed of an organic semiconductor an electrolyte and a gate electrode. First example of chemical sensing with OECTs was reported by Wrighton et al., where transistors based on polyaniline operate in an aqueous electrolyte solution which responds to small changes in pH as well as to redox reagents.[44] In OECTs the active layer also serves as ion selective layer. Moreover, by incorporation of 18-crown-6 ethers into the polyaniline films a detection of low concentration of potassium ions (K^+) was possible.[45] OECT-based sensors are mentioned but are not discussed in detail, since this would exceed the framework of this thesis.

1.2.5 OFETs and Ions

Talking about ion-sensing applications of OFETs implies the understanding of effects of ions on the transistor performance. In general, ions within OFETs are often associated with device instabilities increasing the conductivity and decreasing or distorting the performance. As a matter of fact the effects of ions are not often discussed in literature and systematic investigations are rare.

Nevertheless, different approaches of investigations of OFETs and ions are reported. Determining parts of an OFET are the dielectric and the organic semiconductor. Correspondingly, the effects of ions within the dielectric and semiconductor layer will be separately discussed: Ions within the semiconductor can have different origins e.g. impurities, an electrolyte dielectric, electrodes, substrate, and contact with analytes, or can also originate from deliberately added salts. The latter find the application in light emitting electrochemical cells (LECs).[46] Edman and coworkers reported on an electrochemical method to improve charge injection in OFETs based on an active layer commonly used in LECs, including an organic semiconductor, a salt as ion source and an ion conductor.[47]

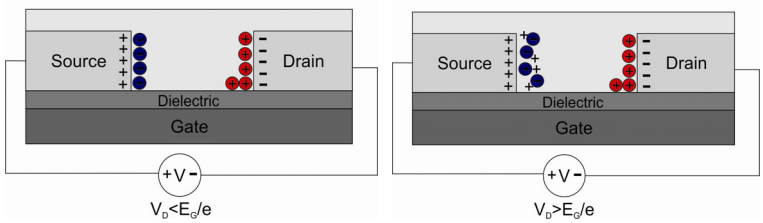

Figure 1.15: Scheme of the formation of charge double layer (left) and corresponding electrochemical doping (right).

Mobile ions within the organic semiconductor will migrate to the electrodes when a voltage is applied between source and drain. They form electric double layers at the semiconductor/electrode interface and screen the bulk electrically (flat band condition). Due to the high electric fields at the interfaces the injection barrier is reduced and the hole injection/ejection is enhanced. Figure 1.15 illustrates the formed electric double layer at the interfaces and Figure 1.16 shows the corresponding schematic energy band diagrams.

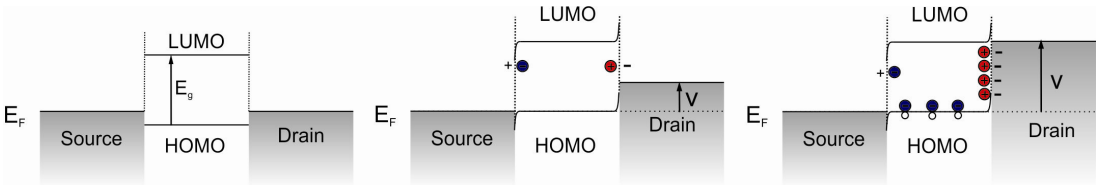

Figure 1.16: Schematic energy band diagrams of a semiconductor in contact with two electrodes illustrating the conditions at V=0V (left) and the formation of electric double layer for $V<E_g/e$ (middle) and electrochemical p-doping for $V= E_g/e$ (right); circles with + and – represents the ions and open circles represents the "stabilized" holes by anions.

In general, when the applied voltage between source and drain exceeds the band gap energy of the polymer ($V>E_g/e$), electrochemical p- and/or n-doping occurs. In detail, electrochemical p-doping happens when a hole is injected from an electrode onto the polymer chain (polymer is oxidized) and at the same time the hole is counterbalanced on the polymer backbone by a negative ion, which is associated with a weak bond between ion and hole (see Figure 1.16, right). Similar to that, n-doping occurs when the injected electron onto the polymer chain is counterbalanced by a positive ion. In principle the operation of organic electrochemical transistors (OECTs) is based on this effect.[48] The electrochemical reactions can be described as follows with *n* representing the number of monomer units in the polymer chain P_n; *y* standing for the number of involved counterions *X* and e^- for the electrons.

$$P_n + ny(X)^- \rightarrow \left[P^{y+}\,(X)_y^-\right]_n + (ny)e^- \qquad \text{p-doping} \qquad (1.12)$$

$$P_n + ny(X)^+ + (ny)e^- \rightarrow \left[P^{y-}\,(X)_y^+\right]_n \qquad \text{n-doping} \qquad (1.13)$$

Basically the formation of an electric double layer at the electrode/semiconductor interface lead to higher on-currents due to the mentioned decreased injection barrier and increased tunneling rate. This was observed by Edman et al., who added ions to the active material of a TFT, which are mobile at elevated temperatures (see Figure 1.17).[47] In particular the active material consists of poly(para-phenylene vinylene) (superyellow) blended with dibenzo-18-crown-6 (DCH18C6) and lithium trifluoromethanesulfonate (lithium triflate). Moreover, he showed that electrochemical doping due to the presence of ions, is responsible for higher off-currents (see Figure 1.17, right).

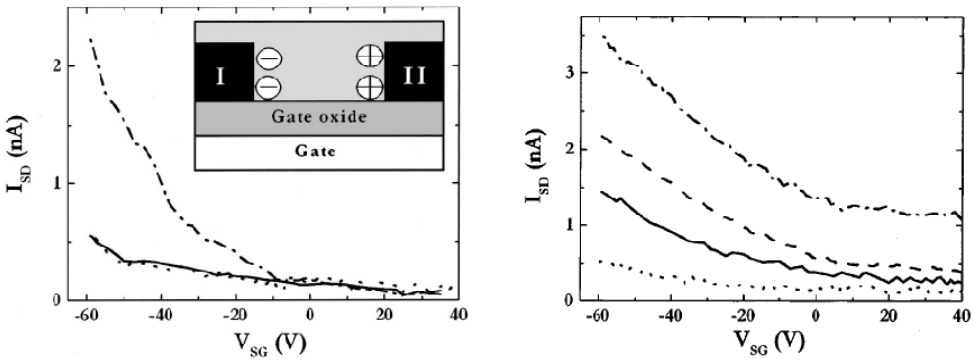

Figure 1.17: Left: Inset shows the TFT structure with the formed ionic layers after charging by applying V_{I-II}=-2 V for 5 min at T=85°C; Transfer characteristics at V_{SD}=-10V of a charged device (dash dotted, V_I=source), a charged device "reverse-biased"(V_I =drain, solid line) and uncharged device (dotted); right: Transfer characteristics V_{SD}=-10V of a charged device at V_{I-II}=-3 V at T=85°C for 5min (solid), 10min (dashed),15min (dash dotted) and a discharged device at short circuit conditions at 85°C (dashed line) (taken from [47]).

Bäcklund and coworkers investigated the modulation of the current by ions through electrochemically oxidizing and reducing of the polymer near the interface to the insulator.[49] Furthermore the redistribution of mobile ions due to an electric field causes hysteresis effects. Rep et al. who reported on mobile Na^+ ions originating from glass substrates observed an increase of current under the influence of applied voltage.[50] The motion of these positive ions also leads to a change of the electrostatic field inside the film and therefore a change of the charge carrier density. Contact and bulk resistance also changes under bias stress since both are sensitive to the local doping level.[51,52]

Mobile ions in the organic semiconductor can also originate from the gate dielectrics, causing also effects in the latter. On the one hand mobile ions within the dielectric lead to mostly undesired hysteresis effects.[a] This tracing of ionic impurities within the dielectric was for example investigated in detail for mobile Na^+ ions within polyvinyl alcohol by us and others.[53,54] On the other hand ionically conducting dielectrics (electrolytes) are applied on purpose to gain high capacitance values and therefore improve the transistor performance. This high capacitance values result from the formation of electric double layers (EDLs) at the interface to the gate and semiconductor, yielding to high charge carrier densities at low voltages (see Figure 1.18).[55,56] Due to the large field at the semiconductor/dielectric interface originating from the EDL, a shift in chemical potential of the semiconductor occurs. This lead to the injection of holes into the semiconductor from the source, to balance the negative charge of an anionic layer, which is formed by a negative applied gate voltage.[57] Moreover ions can also diffuse into the semiconductor causing electrochemical doping, which is schematically shown in Figure 1.18 (right).

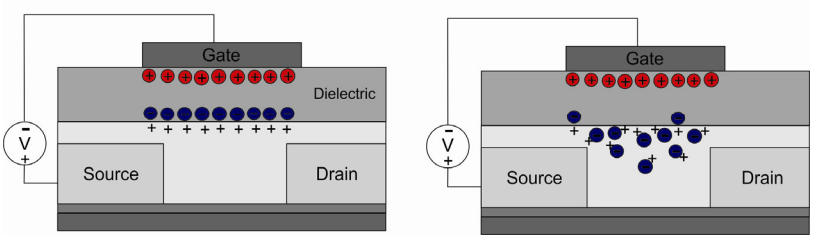

Figure 1.18: Schematic representation of OFETs with electrolyte dielectrics and the formation of electric double layers under applied voltages (left) and the migration of ions into the semiconductor causing electrochemical doping when $V > E_g/e$ (right).

[a] The effect of hysteresis is strongly dependent of the effective measurement time.

2 Experimental

2.1 Equipment at NTC Weiz and Fabrication Processes

In this chapter the device fabrication of bottom-gate/bottom-contact (BG/BC) and top-gate/bottom-contact (TG/BC) OFETs, including photolithography and inkjet printing for structuring the source/drain electrodes, solution preparation and deposition methods, will be presented. Except for the inkjet printer, the applied equipment for sample fabrication and analysis is situated in an ISO-class 6 clean room or gray room at NTC Weiz.

2.1.1 Photolithography for Source/Drain Electrode Structuring

Optical lithography is a well established patterning method for different substrates in today's integrated circuit fabrication based on inorganic semiconductors. The main steps of a photolithographic process include: preparation of the substrate surface, coating of a photoresist, softbake, alignment and exposure through a shadow mask, post-exposure bake, development and removal. The structuring of source/drain electrodes of OFETs presented within this work was also done photolithographically via lift-off process.

The source/drain (S/D) electrodes were structured on highly n-doped silicon (n^{++}-Si) substrates with thermally grown 200 nm thick silicon dioxide (SiO_2), exhibiting a dimension of 1 inch x 1 inch. The n^{++}-Si is used as a common bottom gate and SiO_2 represents the gate dielectric. The first step in the process is scratching at the backside at several spots of the substrate to remove the native SiO_2 and obtain contacts to the n^{++}-Si. This and further process steps were mainly carried out in the wet bench shown in Figure 2.1. It consists of a water purification system (Millipore Elix 3) providing de-ionized water, an ultra sonic bath (Powersonic P1100D), two spin coaters (Süss Delta 6 RC), a hotplate for HMDS application (SSE Optihot VB20) and a standard hotplate (Süss Delta 8 HP). After scratching a standard cleaning process was applied, consisting of: rinsing with acetone and drying with N_2; rinsing with isopropanol and drying with N_2; cleaning in an ultra sonic bath (at level 2) for 2 min at room temperature; rinsing with de-ionized water; spin drying with 5000 rpm for 100 s.

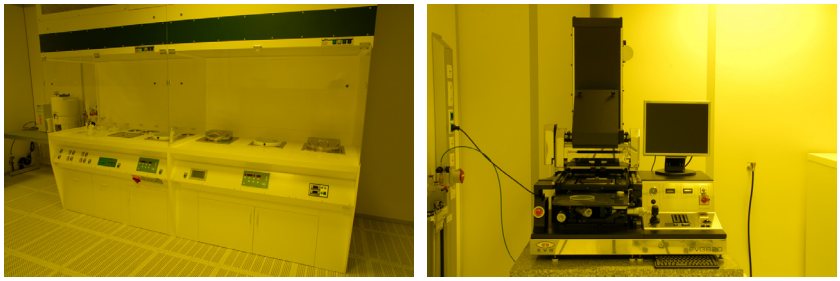

Figure 2.1: Wet bench and EVG 620 mask aligner for photolithography in the clean room at NTC Weiz.

Afterwards a dehydration bake at 200°C for 3 min was performed on the HMDS hotplate, in which vacuum and flushing with N_2 was applied alternately. The substrate was cooled down to room temperature and then 400 µl of the photo resist AZ nLof 2035 (MicroChemicals)[58] was spin-cast with 5000 rpm and 30 s, resulting in a ~2.8 µm resist thickness. Before UV-light exposure a pre-exposure bake at 100°C for 180 s was performed and the sample was cooled down to room temperature. This softbake was done in order to densify the film and remove residual solvents. The exposure of the photoresist to UV-light through a Cr patterned shadow mask made of quartz was carried out in proximity mode with a EVG 620 mask aligner (see Figure 2.1, right), equipped with a 500 W mercury lamp, where substrates with diameters of up to 4 inch can be easily structured with a resolution of 2.5 µm. Proximity mode means that the distance of the mask to the substrate was chosen to be 2 µm. The irradiation was done with a dose of 75 mJ/cm^2 to 80 mJ/cm^2 and as the applied photoresist was of negative type, the exposed parts were cross-linked. Subsequently a post-exposure bake at 110°C for 1 min was performed, for enhanced crosslinking initiated by UV-light exposure. The substrate was developed by immersing it into an AZ® 826 MIF (MicroChemicals) developer for 2 min, obtaining a structure of 12 structures with varying channel lengths (L ~ 2.5 µm, ~ 10 µm, ~ 25 µm, ~ 50 µm). The sample was rinsed with de-ionized water and again dried with the spin coater (5000 rpm, 100 s). Afterwards the substrate with the patterned photoresist was mounted in the small evaporation chamber and evacuated to pressure < 1x10^{-6} mbar. First a 2 nm thick Cr adhesion layer was evaporated with a deposition rate of 0.2 Å/s and afterwards a 50 nm Au layer was deposited with 2 Å/s. The deposition rates had to be adjusted manually for the process in the small evaporation chamber. Finally, the lift-off was done by immersing the sample into the NMP (1-methyl-2-pyrrolidone; MicroChemicals) remover at 65°C in an ultrasonic bath for 5 min. Afterwards the substrates were rinsed with de-ionized water and spin-dried. The obtained source/drain structures were then evaluated with the Olympus BX51 optical microscope (see Figure 2.2, right).

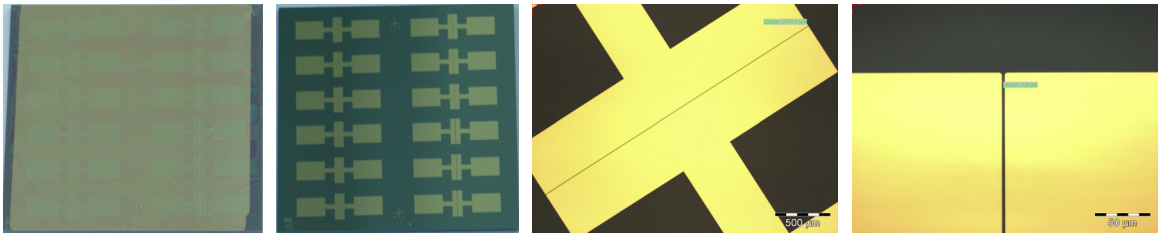

Figure 2.2: From left to right: Photolithographically structured sample after evaporation of Cr and Au; final sample with 12 strucutres of varying channel lengths, micrographs of a device with L = 2.8 µm and W = 2.84 mm; from left to right.

2.1.2 Inkjet Printing of Source/Drain Electrodes

Aside from structuring the source/drain electrodes with photolithography, several electrodes within this thesis were also defined by inkjet-printing a conductive ink. Inkjet-printing represents one of the low cost and large-area manufacturing methods for organic electronics. In literature several reports on this fabrication method for printed organic electronics can be found.[59,60,63] Devices can be fabricated by all-solution based processing techniques. Considering organic field-effect transistors, organic semiconductors, dielectrics and electrode materials are required to be processable in liquid form. For source and drain electrodes high resolution patterning is required and thin homogeneous layers are important for the semiconductor and dielectric layer. With state of the art inkjet printing equipment pattering with dimensions of 10 to 100 µm can be achieved.[61]

With regards to on all inkjet-printed OFET, also suitable printable electrode materials have to be chosen. Such conductive inks include conductive polymers[62] e.g. doped poly(ethylenedioxythiophene) PEDOT:PSS, metals in form of nanoparticle dispersions and solutions of organo-metallic precursor molecules.[63] In general, inks are comprised of a liquid vehicle and a dispersed or dissolved component. Critical characteristics for conductive ink formulations are viscosity, surface tension, wettability drying rate and low resistivity. The desired viscosity depends on the used inkjet-printing technology and is between 8 to 25 cPs for piezo-based technologies.[64] Accordingly the surface tension of an ink is defined by the compatibility with the printhead and by the desired interaction with the substrate surface. The drying rate of the ink influences the speed of possible printing. On the one hand fast drying enables fast printing but on the other hand fast drying can also lead to blocking of the nozzles. Thus it is crucial to choose the ink, printhead and the substrate properly in order to obtain high resolution printing.

For printing electronic materials the most common inkjet technology is drop-on-demand (DOD) printing. One differs between thermal DOD printing and piezoelectric DOD printing. While for the first the wall of the ink chamber is heated, yielding to the formation of vapor bubbles which lead to an ejection of droplets through the nozzle, the piezoelectric DOD printing utilizes the piezoelectric

effect. Thereby a voltage pulse is applied to the piezoelectric stack or a plate and pressure wave is generated, resulting in formation of droplets at the nozzle (see Figure 2.3).

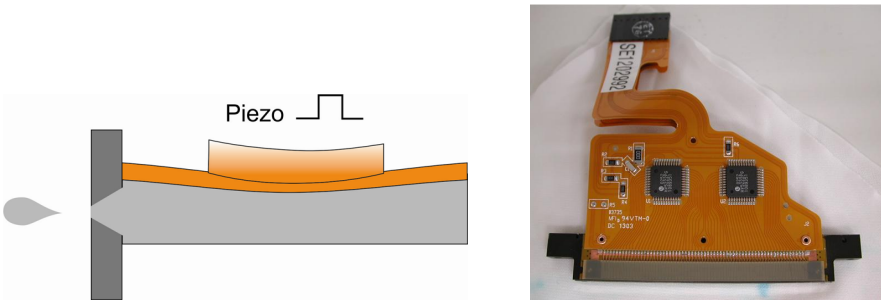

Figure 2.3: Schematic illustration of a piezoelectric printhead (left, redrawn from [64]) and Spectra® SE-128AA printing heat with 128 nozzles (right).

In this work the inkjet-printing technology is also based on piezoelectric DOD printing. For structuring source/drain electrodes, an ITI XY MDS Printer with Apollo II printhead support kit (see Figure 2.4) with a multi-nozzle industrial standard printhead from Spectra (SE-128 AA, S-class), exhibiting 128 nozzles with each with 30 pl drop size, was used. With this equipment printing with a resolution up to 900 dpi is possible.

The chosen ink was a silver nanoparticle (NP) ink (Cabot CCI 300)[65], engineered for piezoelectric inkjet printing to obtain high resolution and low resistivity conductive features. This Ag NP ink has reduced melting and sintering temperature, which are necessary for inkjet printing applications. Aside from other metal nanoparticle dispersions and organo-metallic solutions,[63] in our group a similar ink from CABOT was already successfully used in combination with soft lithography for the fabrication of silver source/drain electrodes in well-performing BG/BC OFETs.[66]

Moreover, for substrate surface modification a Femto plasma etch plant (diener electronic) with oxygen as process gas was used and for further surface evaluation a contact angle meter (Krüss DSA 100), an optical microscope (Olympus BX51) and a stereomicroscope (Olymppus SZX-10) in the laboratories at NTC Weiz were applied.

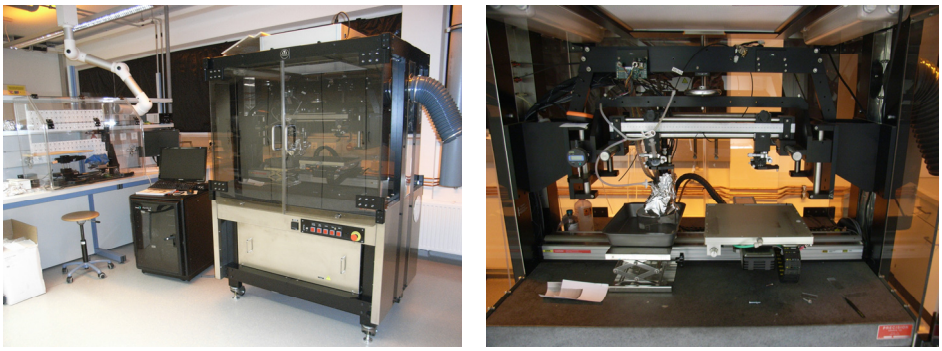

Figure 2.4: ITI XY MDS Printer with Apollo II printheat support kit (left) and interior of the inkjet printer with separated heating units for ink and substrate (right).

When 1 inch x 1 inch $n^{++}Si/SiO_2$ substrates were used, the standard cleaning process described in chapter 2.1.1 was applied with a following dehydration bake at 200°C for 3 min. When, on the other hand flexible substrates like PET films (Mylar®, Melinex® ,Tetoron®), PEN films (Teonex®) and PI films (Kapton®) were used the acetone rinsing and ultra sonic bath cleaning steps as well as the dehydration bake were skipped.

The structure for printing was designed with AutoCAD and then converted to a tagged image file format (TIF) (Figure 2.5). To be in accordance with the photolithograpically structured electrodes, similar structures were designed, except that the dimensions were chosen according to the restricted printing resolution. For example when we used a resolution of 800 dpi, devices with channel length from L = 32 µm to L = 127 µm were designed.

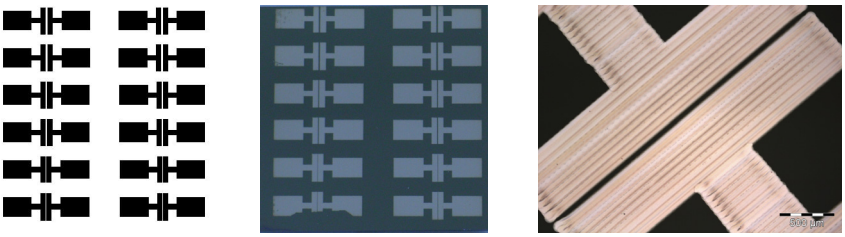

Figure 2.5: Design of S/D structures with 400 dpi (left) and sample with inkjet-printed silver S/D electrodes on Si/SiO_2 (middle) with 3 different channel lengths; device 6 on the left side is not fully printed due to substrate fixing during printing, micrograph of one device with L ~ 30 µm and W ~ 3.1 mm (left).

All the parameters for the print file were set and the substrate was positioned on the heatable stage. At the same time the oven (Heraeus vacutherm) was heated up to 150°C or 200°C for the 30 min sintering step afterwards. Figure 2.5 shows a $n^{++}Si/SiO_2$ substrate with inkjet-printed Ag electrodes with 400 dpi. The detailed optimization process of inkjet printing of source/drain electrodes on different substrates is shown in chapter 6.1.

2.2 Solution Preparation

2.2.1 Organic Semiconductors

Besides the evaluation of new semiconductor materials in OFETs, regioregular poly(3-hexylthiophene) (rr-P3HT, Plexcore® OS)[67,b] was used as organic semiconductor for all further investigations. The preparation of the solutions and further fabrication steps were carried out under inert atmosphere in the argon box (see Figure 2.8) and was similar for most of the semiconductors, differing only in heating processes. The rr-P3HT used exhibits a number average

[b] Materials were bought from Sigma Aldrich

molecular weight of M_n ~ 25000 g/mol, a polydispersity of ~ 2, a HOMO energy level at 4.3-6 eV and a bandgap of E_g=2.3-3 eV

Poly(3-hexylthiophene) is a very common conjugated polymer used as p-type semiconductor in OFETs and is depicted in Figure 1.1. Mobilities up to 0.1 cm/Vs are reported with rr-P3HT approaching values of inorganic counterparts based on amorphous silicon.[68] The performance of OFETs strongly depends on the chemical and structural ordering of the polymer chains at the semiconductor/insulator interface.[69] The high mobility values found for P3HT are ascribed to the self-organizational behavior which results in nano- or even microcrystalline structures. The laminar structure formed exhibits a good π-π-interaction, hence good interchain charge transport is the result. Two orientations of regioregular-P3HT are obsereved depending on the degree of head to tail coupling and the molecular weight. The molecules can be oriented with thiophene rings flat on the surface or with the thiophene chain edge on the surface (see Figure 2.6). The latter exhibits lower mobility values in comparison to the former.

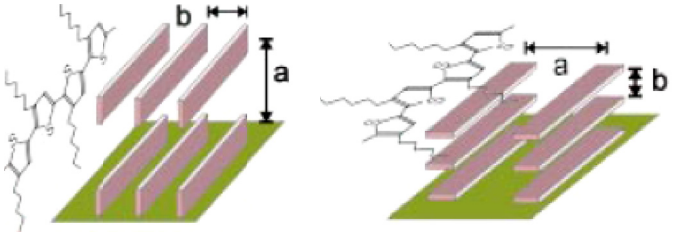

Figure 2.6: rr-P3HT with edge-on (left) and flat-on (right) surface orientation (Schemes taken from [69]).

The preparation of a rr-P3HT solution was performed in the following manner: first the raw material was weighed in a small glass vial and a dehydration bake at 120°C for 2 h under high vacuum was performed to remove residual water and oxygen.[70,71] After ca. 1h cooling to room temperature the vial was weighed again to make sure that no material was lost and spectrally clean (HPLC grade) chloroform ($CHCl_3$) or toluene ($C_6H_5CH_3$) was pipetted to obtain a 2 mg/ml solution. When toluene was used as solvent the solution was stirred and heated up to 60°C for 10 min, otherwise it was not possible to achieve good solubility. For storage it was sealed with parafilm and wrapped with aluminum foil to avoid ambient light exposure of the solution.

2.2.2 Dielectric Materials

For top-gate/bottom-contact (TG/BC) OFETs polyvinyl alcohol was chosen as dielectric layer. In addition for OFETs where the effects of ions within the dielectric layer were investigated, a novel functionalized polymer was applied as well (see for solution preparation chapter 5.1). PVA is soluble in water, exhibits resistance to many organic solvents and can be solution deposited due to low viscosity. Moreover, smooth films exhibit a dielectric constant in the range of 6-10, hence

making it a good candidate for gate dielectrics in OFETs. Polyvinyl alcohol is basically a polymer of vinyl alcohol (see Figure 2.7). It is manufactured by polymerization of vinyl acetate in methanol, where a subsequent hydrolysis converts the polyvinyl acetate to polyvinyl alcohol with sodium hydroxide as catalyst. Its technical properties strongly depend on the molar mass and the residual acetyl groups. According to the content of residual acetyl a distinction between fully and partially hydrolyzed PVAs is made. Examples for the fully hydrolyzed PVA in this work were Mowiol 4-98 and 6-98, whereas Mowiol 5-88 is partially hydrolyzed (see Table 2.1).[72] All three Mowiol grades were used within this work.

Table 2.1: Technical data of different Mowiol grades [taken from 72]

	$\overline{M_w}$ [g/mol]	Viscosity[c] [mPa · s]	Degree of hydrolysis [Mol%]	Residual acetyl content [wt%]	Max ash content[d] [%]
Mowiol 5-88	37000	5.5±0.5	88±1	10.8±0.8	0.5
Mowiol 4-98	27000	4.5±0.5	98.4±0.4	1.5±0.4	0.5
Mowiol 6-98	47000	6.0±0.5	98.4±0.4	1.5±0.4	0.5

The PVA granules were dissolved in de-ionized water with a concentration of 15-20 wt% and then stirred at 90°C for 45 min to 3h, depending on the Mowiol grade. Afterwards dialysis was performed to reduce the acetyl group content. The prepared solution was filled into dialysis tubes (Spectra/Por®, MWCO=3500 Dalton)[73] and put into a de-ionized water basin. Consistently the conductivity of the water was measured and changed respectively.[25] The dialyzed solutions exhibit a concentration of 8-9 wt%.

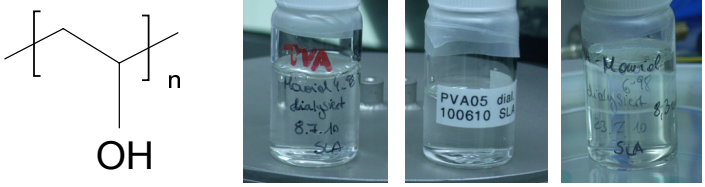

Figure 2.7: Chemical structure of polyvinyl alcohol (left) and prepared dialyzed PVA solutions (left: Mowiol 4-98 with 8.3 wt%; middle: Mowiol 5-88 with 9 wt%, right: Mowiol 6-98 with 8.3 wt%).

[c] Viscosity of a 4% aqueous solution at 20°C
[d] It is calculated as NaO_2. The ash content is a percentage of inorganic matter and therefore a measure for the purity of an organic material.

2.3 Device Fabrication

After structuring the source/drain electrodes for the bottom- and top-gate/bottom-contact OFETs, the samples were transferred into the argon boxes to proceed with device fabrication (see Figure 2.8). In the following the fabrication of OFETs based on rr-P3HT are described in detail. The process steps are similar for almost all OFETs within this thesis, differing mainly in different heating steps. After a dehydration bake at 120°C for 1 h in high vacuum to remove adsorbed water on the surface, the samples were cooled to room temperature. The organic semiconductor (rr-P3HT solution) was deposited on the substrate by spin-casting at 1500 rpm for 40 s to obtain ~30 nm thick films (see Figure 2.8). Then the samples were dried in the sealable hotplate for 1h at 120°C in high vacuum (p~ $5x10^{-5}$ mbar) to remove residual solvents and water.

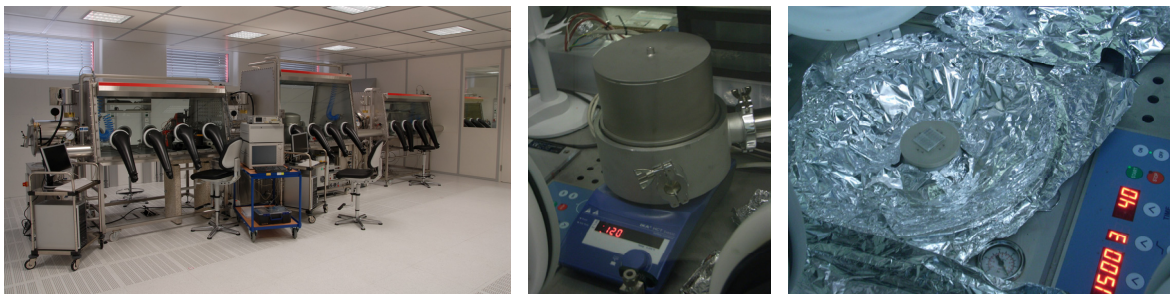

Figure 2.8: From left to right: glove box cluster with 4 interconnected argon boxes; sealable hotplate connected with a vacuum pump; spin coater (Süss Delta 6RC).

BG/BC OFETs were transferred to another glove box for the last step before measurements were done, whereas for TG/BC OFETs the deposition of the gate dielectric and electrode was performed. Before that frames were scratched around the devices to minimize leakage current. Then the prepared PVA solution was spin-cast on a sample at 1500 rpm for 60 s at room temperature and dried first at 60°C for 30 min which was increased to 100°C in high vacuum for 3 h or overnight. This step was followed by the deposition of the gate electrodes (see Figure 2.9) in the fully automatic evaporation chamber. 100 nm thick meander-shaped silver gate electrodes were evaporated with a deposition rate of 10 Å/s in high vacuum (p<10^{-6} mbar). OFETs on $n^{++}Si/SiO_2$ substrates were mounted on cooper plates with conductive silver to contact the bottom gate and frames were also scratched for BG/BC OFETs (see Figure 2.9, left).

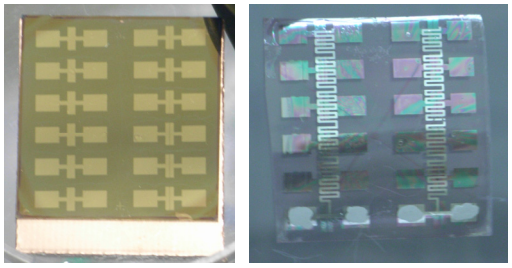

Figure 2.9: Completed rr-P3HT BG/BC OFETs attached to the cooper plate (left) and rr-P3HT TG/BC OFETs with inkjet-printed source/drain electrodes on PEN film.

2.4 Measurement Techniques

The electrical characterization of the fabricated devices was done in argon on a PM5 (Süss) probe station which can be connected with feedthroughs to the measurement units.

2.4.1.1 Capacitors

Within this work also capacitors were fabricated for analysis. A detailed explanation of the fabrication process can found in the corresponding chapter (5.2.1.) The samples were connected on the probe station with an Agilent E4980A LCR Meter to perform capacitance measurements. First a frequency sweep was performed by recording the absolute impedance |Z| and phase angle Θ as a function of frequency. The frequency was applied from 100 Hz to 100 kHz increasing logarithmically at a test signal amplitude of 1V. After that DC-bias dependence of the capacitors was investigated by sweeping a superimposed DC bias from 0 V to 40 V to -40 V and back to 0 V at a test signal amplitude of 1 V and test signal frequency of 1 kHz. With this measurement the capacitor was tested for operational stability.

2.4.1.2 OFETs

In order to electrically characterize the fabricated OFETs transfer and output characteristics were recorded in forward and reverse sweep with an Agilent B1500 parameter analyzer with a E5250A/E5252A switch matrix. Usually for rr-P3HT based OFETs the transfer measurements were performed by sweeping the gate voltage in 1 V steps from +10 V to -50 V and backwards by constant drain voltages of -10 V, -20 V, -30 V, -40 V and -50 V. The positive voltages were applied to release trapped charge carriers at the semiconductor/dielectric interface. Subsequently after measuring the transfer characteristics, the output characteristics were recorded. Further measurement proceedings are varying according to the effects to be investigated. Preferably representative devices with L = 10 µm and 25 µm were chosen for the device characterization.

3 Basic Evaluation of Novel Organic Semiconductor (OSC) Materials

In this chapter, the results of the investigation of novel organic semiconductors in bottom-gate/bottom-contact (BG/BC) OFET architecture on n^{++}-Si/SiO_2 substrates will be presented. This includes the fabrication and the electrical characterization of OFETs based on new conjugated polymers containing carbazole units and denrimers with pyrene core units. Besides the well established organic semiconductors for OFETs, such as P3HT and Pentacene, it is interesting to investigate other novel organic compounds with new properties, since the properties of many established organic materials are strongly influenced under operation in ambient conditions, which is a crucial factor for many applications.

3.1 Carbazole-based OSCs

Two novel conjugated polymers containing a 3,9-linked carbazole unit in the main chain from the group of Fumio Sanda[74] were investigated. In general carbazole is a well known conjugated unit, which shows interesting electrical and optical properties. Moreover carbazole derivates exhibit high charge carrier mobilites, thus often used as hole-transporting layer in electroluminescent devices; they are thermally stable and have large band gaps. Therefore much effort has been done to synthesize polymers with carabazole units in the main chain. The properties of such polymers strongly depend on the position of the linkages to the carbazole. Compared to 2,7-linked and 3,6-linked polymers, less attention has been paid to 3,9-carbazole, probably due to their difficult synthesis.[75] However the latter have a C-N bond in the main chain, hence an unshared electron pair of the nitrogen, which is interesting for investigations. From differently synthesized poly(3,9-carbazolyleneethynylenearylene)s the bis(thienyl)benzothiadiazole-linked polymer, referred to as polymer P7 in the paper of Tamura et al.[75] and here. The chemical structure of polymer P7 is depicted in Figure 3.1 (left).

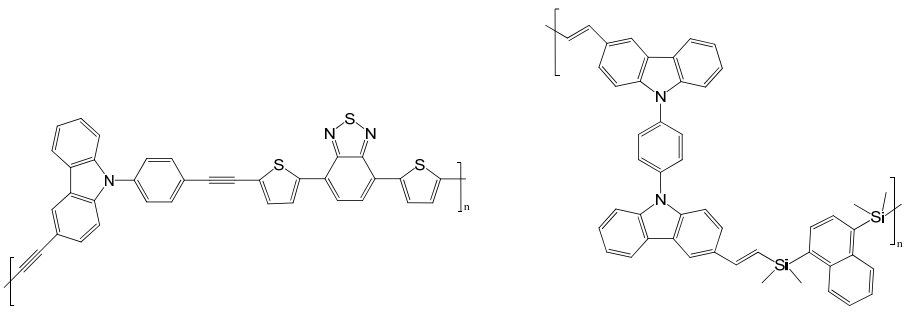

Figure 3.1: Chemical structure of carbazole based polymer P7 (left) and polymer 3c (right).

The second conjugated polymer, containing 3,9-linked carbazolyene has additional silylene moieties (see Figure 1.1).[76] These silylene moieties are considered to be responsible for an extended σ-π conjugation through the main chain. In this work this polymer will be referred to as polymer 3c.

It is expected that these polymers have an extended conjugated length, therefore interesting for applications in OFETs. For p-type materials, being stable under ambient conditions the ionization potential should be as high as possible, in consequence the HOMO level should be as low as possible. In literature it was reported that for air-stable materials the HOMO level should be at least < 5 eV below the vacuum level.[77] For the poly(3,9-carbazolyleneethynylenearylene)s it was reported to have a HOMO level at 5.26 eV[78], giving a motivation to apply the novel conjugated polymers in OFET structures.

3.1.1 Sample Preparation

First a solution of the carbazole based polymer P7 was prepared. The polymer was baked for 2 h at 80°C in vacuum ($p < 1x10^{-5}$ mbar) and a solution of 1 mg/ml in $CHCl_3$ and 2 mg/ml THF was prepared. The material was not completely soluble, which can be seen in Figure 3.2. This may be ascribed to the low content of side groups of the polymer. Agitating the solution at 40°C for 1 h did not show any difference and thus filtering of the solution with a 0.45 µm PTFE filter was necessary.

Figure 3.2: Solutions of carbazole-based polymer P7 with 2g/l in THF (left) and 1g/l in $CHCl_3$ (right).

In comparison, the dehydration bake of the rough material of polymer 3c was skipped and was dissolved with 4g/l in $CHCl_3$ without any solubility problems.

As OFET substrate an n^{++}-Si/SiO_2 was used with photolithographically structured gold source/drain electrodes (see chapter 2.1.1.). After measuring the channel lengths and widths the samples were transferred to the argon glove box to perform a dehydration bake at 120°C for 1 h in high vacuum. The following device fabrication is already depicted in chapter 2.3, including the deposition of the active layer (1500 rpm, 40 s) and drying of the film (see Figure 3.3). The polymer P7 film was

dried at 80°C for 1h in high vacuum, whereas the film based on the polymer 3c was dried on the hotplate at 50°C for 15 min in argon. Finally to contact the gate electrode the samples were mounted to a cooper plate with conductive silver.

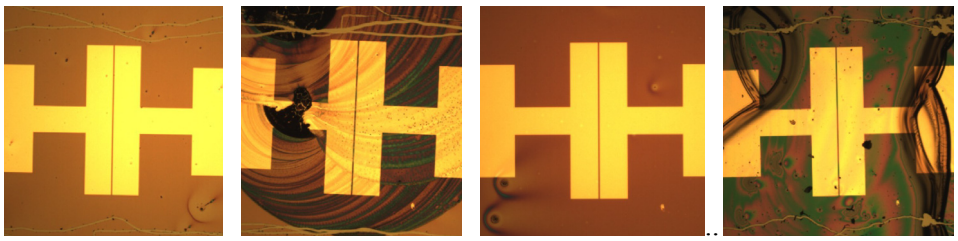

Figure 3.3: From left to right: devices (L=25 µm) after spin and drop-casting of 2 g/l polymer P7 in THF and of 4 g/l of polymer 3c in $CHCl_3$.Figure 3.4

3.1.2 Electrical Characterization

The electrical characterization was carried out under inert atmosphere in an argon glove box on a Süss PM5 probe station. Transfer measurements were performed where the gate voltage was increased up to 100 V while the drain voltages had constant values of 0 V, 25 V, 50 V, 75 V, 100 V. The measurements revealed no field-effect and hence no semiconducting behavior of polymer P7 and 3c. The obtained currents were in the range of pA and nA and can only be ascribed to gate leakage currents. As a consequence more material was deposited over the source/drain structure by drop-casting (dried at 50°C for 10 min, see Figure 3.3). Even after drop-casting the characterization of the devices did not show a field-effect. One reason can be that due to the structure of the polymers no proper alignment of the polymer chains was possible to obtain a non disturbed percolation path for charge carriers.

3.2 Conjugated Dendrimers

Furthermore conjugated dendrimers from the group of Klaus Müllen of the Max Planck Institute for Polymer Research[79] were investigated in respect to their usability in OFETs. These dendrimers are specially designed for blue emitting diodes, exhibiting a blue fluorescent pyrene as core and a triphenylene shell forming an efficient energy transfer system.[80] Moreover, on the surface of the shell are triphenylamine units which serve as a charge trapping sites. The chemical structures of the two novel conjugated dendrimers PYG2CAP and PYG2TPA are depicted in Figure 3.5.

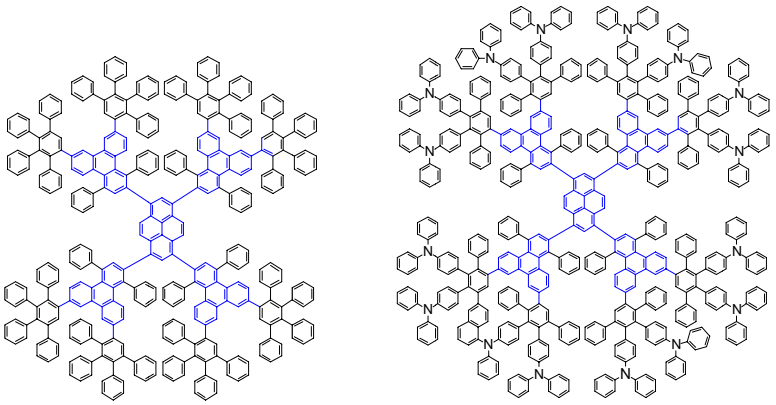

Figure 3.5: Chemical structure of PYGCAP (left) and PYGTPA (right).

The application of these dendrimers yielded stable deepblue emitting organic light emitting diodes. It is also interesting to investigate these novel materials in OFET structures, assuming that dendrimers align to each order.

The dendrimers PYGTPA and PYGCAP were dissolved in spectrally clean (HPLC) toluene with a concentration of 5 mg/ml and no dehydration bake of the rough material was performed. The solutions were spin-cast (1500 rpm, 40 s) on n^{++}-Si/SiO_2 substrates (KSC24, KSC25), after performing a dehydration bake of the latter, as described in chapter 2.3. The films were dried for 10 min on a hotplate at 60°C. Afterwards the samples were mounted to a cooper plate with conductive silver. Figure 3.6 shows the corresponding devices after spin-casting.

Figure 3.6 From left to right OFET devices (L ~ 25 µm) with PYGCAP after spin-casting (5 g/l toluene; KSC24) and drop-casting (5 g/l cyclohexanon; KSC12), PYGTPA after spin-casting (5 g/l toluene; KSC25) and drop-casting (5 g/l cyclohexanon; KSC13);.

The electrical characterization was carried out under inert atmosphere. First investigations did not reveal any field-effect for OFETs based on dendrimer PYGTPA and PYGCAP. The reason for that can be that the dendrimers were not aligned properly and therefore no percolation bath for charge carriers could be achieved. Hence for the second batch of OFETs the dendrimers were dissolved in cyclohexanon (5 mg/ml), which exhibits a boiling point at 140°C. This was expected to allow the dendrimers for a extended time to better align or assemble. 5 µl of the dendrimer solutions were drop-cast and the samples were dried in the sealable hot plate at 60°C for 10 min in argon and then at 80°C for 1 h in high vacuum (p ~ $7x10^{-4}$) (see Figure 3.6).

OFETs based on dendrimer PYGCAP did not reveal any functioning devices, no field-effect could be observed. Most of the devices revealed an ohmic behavior. In contrast few devices based on dendrimer PYGTPA showed a distinct field-effect. Figure 3.7 shows the recorded transfer characteristics, exhibiting a very low device performance, with source-to-drain channel currents in the range of pA. The switch-on voltage was obtained to ~ -60 V. Moreover the leakage currents are in the same range as the channel currents and the field-effect mobilities in the saturation regimes are about ~10^{-5}cm^2/Vs. A reason for the very low device performance is most likely ascribed to the worse or even not present alignment of the dendrimers. Moreover ongoing AFM and STM experiments showed that, dendrimers exhibit no particular ordering.

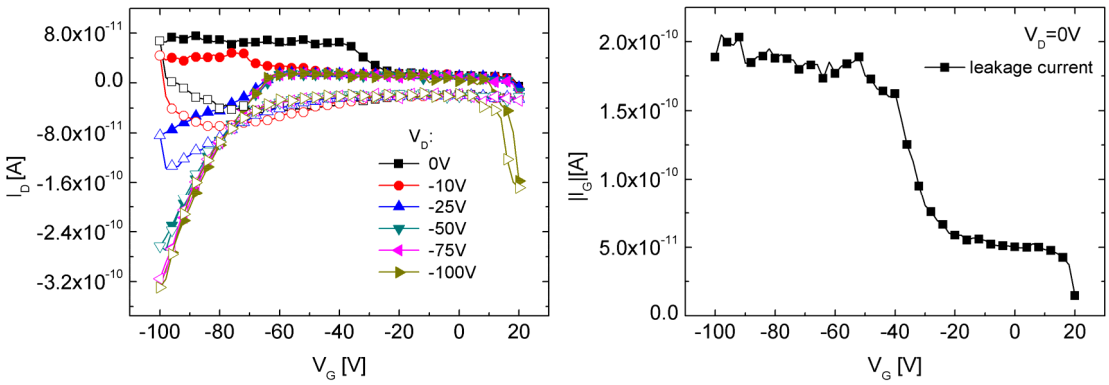

Figure 3.7 Transfer characteristics (left) of a device based on dendrimer PYGTPA (5 g/l in cylcohexanon) and corresponding gate leakage (right)current for V_D = 0 V; (L = 25µm, W = 2.85 mm ,KSC13).

Another attempt to improve the device performance of the OFET was by drop-casting the dendrimere solutions and drying of the films under saturated atmosphere. However, following measurements showed that no improvement was obtained.

3.3 Summary and Conclusions

In summary, novel organic semiconductors were evaluated in a bottom-gate/top-contact OFET architecture. It was found that the OFETs with novel conjugated polymers based on carbazole units did not reveal a field-effect, hence no semiconducting behavior. This can probably be ascribed to a improper alignment of the polymer chain. Besides that solubility problems were faced for the polymer P7. In contrast, OFETs based on dendrimere PYGTPA yielded a distinct field effect but showed rather low performance by exhibiting source-to-drain channel currents in the range of ~10^{-10} nA and a switch-on voltage of about ~ -60 V. On the other hand the OFETs based on PYGCAP did not reveal any functioning devices, most likely due to non existing alignement of the dendirmers in the film. To conclude, the investigated novel semiconductors are not very appropriate for applications in OFETs.

4 Mixed Ionic-Organic Semiconductor – OFETs based on rr-P3HT – DCH18C6 – CF_3SO_3Na Blend

4.1 Introduction

As mentioned in the fundamental section, OFETs are promising devices for sensing applications. In this work the main focus is set on ion sensing. The presence of ions within an OFET results in several effects and it is crucial to understand the underlying mechanisms to develop corresponding sensor concepts. Therefore, in order to investigate the behavior and effects of ions within the organic semiconductor in more detail, bottom-gate/bottom-contact OFETs including deliberately added ions within rr-P3HT were fabricated on n^{++}-Si/SiO_2 wafer substrates. This mixed ionic-organic semiconductor layer is a blend film of regioregular poly(3-hexylthiophene-2,5-diyl) (rr-P3HT), sodium trifluoromethanesulfonate (CF_3SO_3Na, sodium, triflate) and dibenzo-18-crown-6 (DCH18C6, crown ether). Such a combination of an organic semiconductor, a salt and an ion-solvent or rather ion conductor is commonly used for light-emitting electrochemical cells, where the injection barrier is significantly reduced by the formation of an electric double layer and electrochemical doping, leading to improved charge injection.[46] In this chapter the influence of ions within the organic semiconductors are thoroughly analyzed and compared with OFETs based on rr-P3HT solely. Moreover, in preliminary work bottom-gate/bottom-contact OFETs based on DCH18C6 and rr-P3HT were fabricated and analyzed with respect to a rr-P3HT reference device to investigate the influence of the additionally added ion conductor. Parts of the presented data can also be found in a publication ("*Organic field-effect transistors applicable for gas and ion detection*", A. Klug, K. Schmoltner, E. J. W. List).

4.2 Materials and Sample Fabrication

The materials used for the blend solution were rr-P3HT as semiconducting polymer, sodium trifluoromethanesulfonate (CF_3SO_3Na; sodium triflate) and dibenzo-18-crown-6 (DCH18C6).[e] The chemical structures are depicted in Figure 4.1. Sodium triflate represents the ion source (Na^+ ions) and the crown ether acts as ion conductor. With its closed ring of ethylene oxide units the latter forms an attractive cavity for certain cations (mostly alkali metal ions). The stability of such a formed complex and therefore the ion mobility depends on the size of the cations in relation to the size of the crown ether cavity.[81] Moreover, salts are not soluble in non-polar solvents and hence the crown ether unit acts also as a phase transfer catalyst[82] and prevents a recrystallization.

[e] Materials were bought from Sigma Aldrich: CF_3SO_3Na (Product no. 367907-5G), DCH18C6 (Product no. 158399-10G).

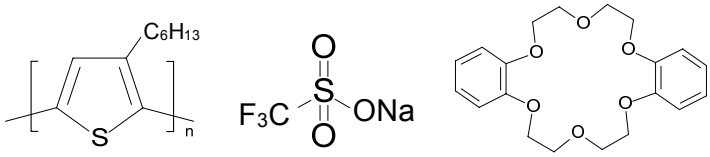

Figure 4.1: Chemical structure of regioregular poly(3-hexylthiophene-2,5-diyl) (rr-P3HT), sodium trifluoromethanesulfonate (CF_3SO_3Na) and dibenzo-8-crown-6 (DCH18C6).

Therefore sodium triflate and the DCH18C6 were weighed in a mass ratio of approximately 1:5[f], which corresponds to a mol ratio of 1:2.5 (CF_3SO_3Na:DCH18C6) and was dissolved in spectrally clean (HPLC) toluene, yielding a 2 mg/ml solution of DCH18C6. Afterwards the solution was stirred on a hotplate at 60°C for 10 min. Moreover a small amount of rr-P3HT was weighed and a dehydration bake was performed as described in chapter 2.2.1. At room temperature it was dissolved in the CF_3SO_3Na-DCH18C6 blend solution at a concentration of 2 mg/ml. The overall mass ratio of the solution was about 5:1:5 (rr-P3HT:CF_3SO_3Na:DCH18C6). This solution was then stirred at 60°C for 10 min to obtain good solubility. Besides the blend solution a standard rr-P3HT solution (see chapter 2.2.1) was prepared for reference devices. Both solutions are depicted in Figure 4.2. Aside from the ion-containing solution a rr-P3HT-DCH18C6 blend solution based on spectrally clean (HPLC) chloroform ($CHCl_3$) was prepared with a mass ratio of 1:1. A corresponding reference solution was fabricated as well. $CHCl_3$ was afterwards replaced by toluene because of solubility problems for the $CHCl_3$ blend solution containing the salt.

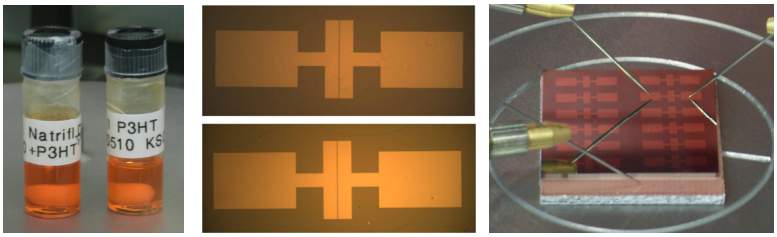

Figure 4.2: Left: Prepared rr-P3HT - CF_3SO_3Na - DCH18C6 blend solution and rr-P3HT reference solution; middle: micrographs of 25µm devices of ion-containing sample (KSC13, top) and of reference sample (KSC12, bottom); right: contacted device on sample KSC13.

The bottom-gate/bottom-contact OFETs were fabricated on n^{++}-Si/SiO_2 wafer substrates. The 50 nm Cr/Au source/drain electrodes were structured photolithographically as described above (chapter 2.1.1). The substrates were then transferred into the glove box where a dehydration bake was performed at 120°C for 1 h in high vacuum (p~ $5x10^{-5}$mbar). The blend solution was spin-cast (1500 rpm, 40 s) after heating at 60°C in order to prevent a phase separation within the solution. Then the samples were dried in the sealable hotplate for 1 h at 80°C in high vacuum

[f] Three batches were fabricated and the mass ratio between the CF_3SO_3Na: DCH18C6 is varying between 1:5.4 and 1:4.8 due to limited accuracy of weighting out.

(p~ $5x10^{-5}$mbar). The reference samples were fabricated in a similar way, except that the solution was not heated for spin-casting and the annealing temperature of the layer was set to 120°C instead of 80°C. Edman et al. described similar film preparation for light-emitting devices.[83] The samples were transferred into the argon glove box for electrical characterization on the probe station via locks (no air exposure in between). The samples were mounted on cooper plates with conductive silver to contact the gate electrode and frames were scratched around the devices to minimize leakage currents. Figure 4.2 shows a typical fabricated sample with 12 devices of varying channel lengths (3 x ~2.5 µm, 3 x ~10 µm, 3 x ~25 µm, 3 x ~50 µm) (right) and the comparison of micrographs (middle) of 25 µm devices of an ion-containing sample (top) and of a reference sample (bottom).

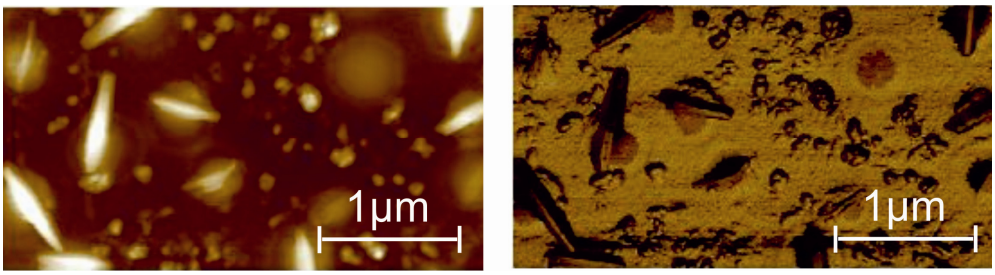

Figure 4.3: Topographic AFM image (left) and corresponding phase image (right) of the P3HT - CF_3SO_3Na - DCH18C6 blend film in the channel; scan size: 5µm; color code from black to white corresponds to a z-data with a maximal range of 100nm.

In order to investigate the rr-P3HT-CF_3SO_3Na-DCH18C6 blend films and possible phase separation of the salt with the nonpolar polymer rr-P3HT, atomic force microscopy (AFM) was used. Figure 4.3 (left) shows the height image of a rr-P3HT-CF_3SO_3Na-DCH18C6 blend film within an OFET channel. Needle like features with a length up to ~800 nm and widths up to ~250 nm could be observed and most likely can be assigned to sodium triflate particles. The investigation of the surface indicates that the materials, especially the salt were not completely dissolved due to the bad solubility of salts in nonpolar solvents or that recrystallization occurred. The topographic image also revealed circle-shaped agglomerations with diameter d between 50 nm and 200 nm, which are also observable in the phase image (Figure 4.3, right). As expected also phase separations in form of circular shaped features (d ~ 70 nm to ~ 300 nm) were identiefied.[83]

4.3 Comparison of rr-P3HT-DCH18C6 based OFET with rr-P3HT based Device

The electrical characterization was carried out under inert atmosphere in an argon glove box on a Süss PM5 probe station. Transfer and output measurements were performed with drain and gate voltages up to -100V. For further measurements maximum voltages were reduced to -50V. Transfer characteristics depicted in Figure 4.4 reveal similar performance of the devices based on rr-P3HT-DCH18C6 and P3HT solely in terms of on-current, off-current and mobility, which indicates that the added DCH18C6 doesn't disturb the percolation path within P3HT. Moreover, both samples show a distinct hysteresis due to trapping of charges at the semiconductor/dielectric interface or within the semiconductor layer. A possible reason is that for this device series no annealing step under high vacuum was performed after deposition of the films; only drying on the hotplate for 15min was done. Therefore residual water or oxygen at the SiO_2 interface can result in additional trapping sites, causing a hysteresis.

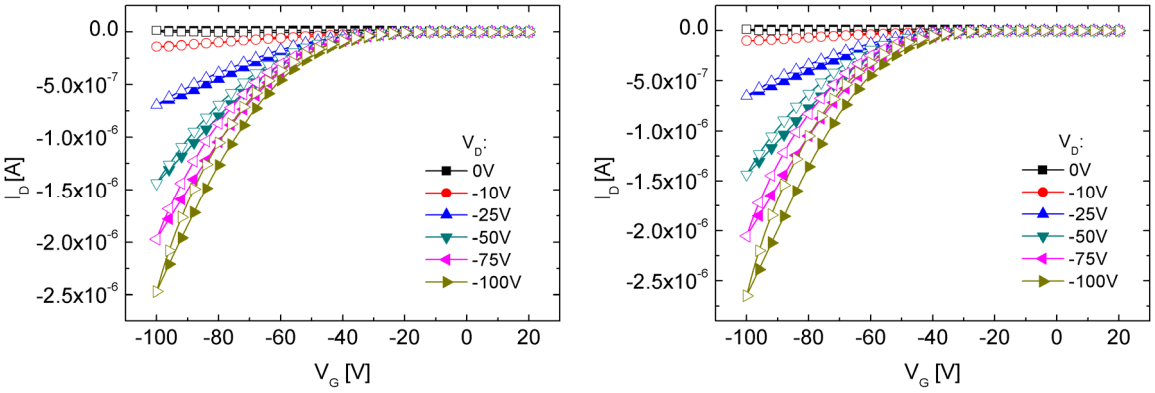

Figure 4.4: Transfer characteristics of 25 µm OFETs; left: device based on rr-P3HT-DCH18C6 blend (sample KSC19); right: reference device based on rr-P3HT solely (sample KSC18); closed symbols: forward sweep; open symbols: reverse sweep.

Figure 4.5 shows similar mobility values, which at V_G=-60V are about μ_{Sat}~4x10^{-4} cm^2/Vs for the saturation regime and μ_{Lin}~5x10^{-4} cm^2/Vs for the linear regime. The switch-on voltage was determined at around -12V for both samples and the subthreshold slope was around 5 V/dec.

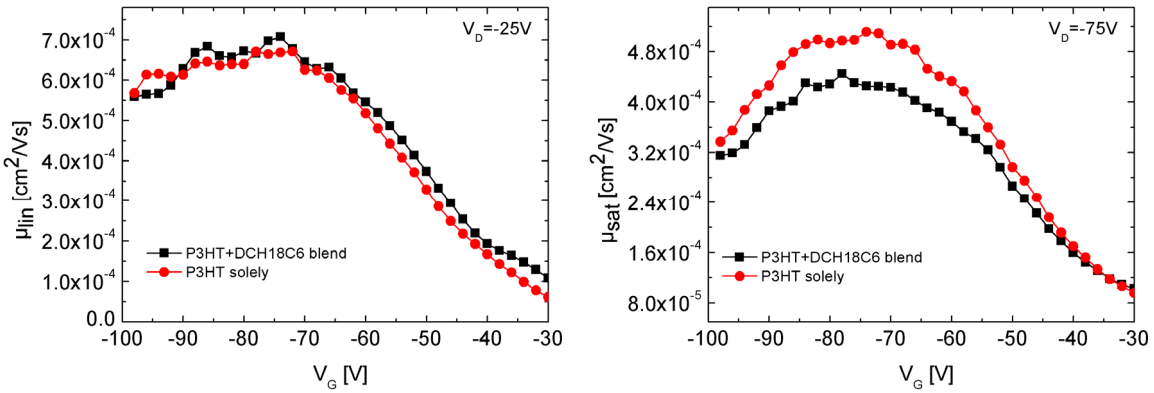

Figure 4.5: Field-effect mobility in linear (left) and saturation (right) regime of an OFET based on rr-P3HT-DCH18C6 blend (squares) and of a rr-P3HT reference device (circles).

4.4 Comparison of a rr-P3HT-DCH18C6-CF_3SO_3Na based Sample with a rr-P3HT based Reference Device

This section describes the results of the detailed investigation of OFETs with deliberately added ions in comparison with OFETs based on rr-P3HT solely. Transfer and output characteristics of every device were recorded with forward and reverse sweeps. To ensure reproducibility of the results three batches were fabricated. This section mainly describes the results of one representative series with devices exhibiting 25 µm channel length and 2.85 mm channel width.

Figure 4.6 depicts the transfer and output characteristics of a typical ion-containing OFET (top) and a reference device (bottom). The latter yielded slightly larger on-currents for the transfer curves. This can be described with the higher trap density within the ion-containing OFET due to a phase separation of the sodium triflate:DCH18C6 and rr-P3HT and a possibly disturbed alignment of the organic semiconductor. Compared to the transfer curves, the I_D values in the output characteristics are smaller at the same working point for both samples. Here high gate voltages are longer applied and bias-induced charge carrier trapping is the predominant effect. However the difference between the maximum values of the channel currents in transfer and output characteristics is much larger for the ion-containing OFETs, which also indicates the presence of a larger trap density. Moreover, the transfer curves of both devices exhibit lower channel currents in the reverse sweep due to charge carrier trapping. However when mobile ions (Na^+) are present the amount of hysteresis is larger.[50] In contrast to the transfer curves the output curves for the ion-containing devices exhibits larger channel currents for the reverse sweep. One explanation could be the non-existing release of trapped charge carriers upon application of positive V_G, which take place during the measurement of each transfer curve. As a consequent the effect of ions (described below) become more dominant in the output characteristics, leading to an increase of current with time. Furthermore, positive ions

can move to the dielectric/semiconductor interface upon applied negative gate voltage, which can possibly lead to a release of trapped charge carriers.

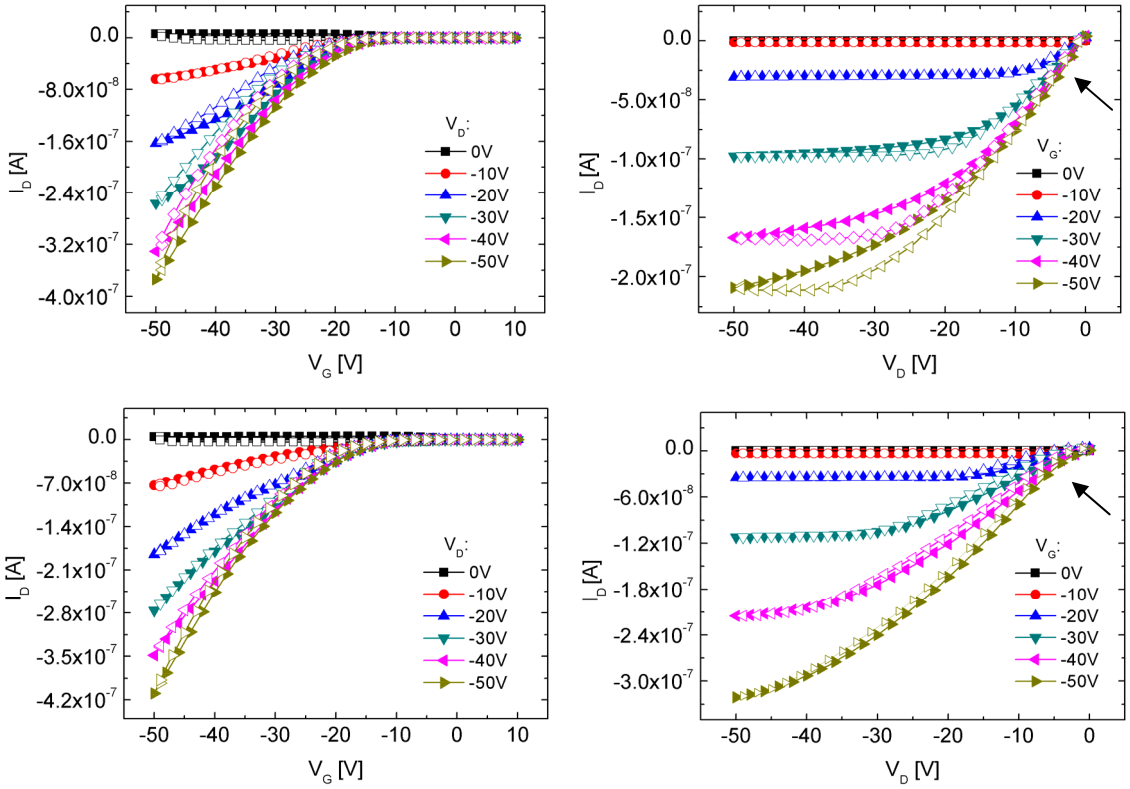

Figure 4.6: Transfer (left) and output (right) characteristics of typical OFETs (L = 25 µm, W = 2.85 mm); top: device based on P3HT-CF_3SO_3Na -DCH18C6 blend (sample KSC13); bottom: reference device based rr-P3HT solely (sample KSC12); closed symbols: forward sweep; open symbols: reverse sweep; arrows are indicating the change in curvature.

In order to investigate the ion movement and the corresponding effects in more detail, the channel currents were measured at a certain fixed working point in the saturation regime (V_G=-30V, V_D=-40V) for 200 s. Figure 4.7 depicts the corresponding graph. The reference device exhibits the expected decreasing channel current I_D due to charge carrier trapping at chemical and/or structural impurities near the rr-P3HT/SiO_2 interface and/or within the SiO_2 and rr-P3HT.[84,85] On the contrary the OFET including ions showed, after a short "charge carrier trapping period" and/or possible charging of the gate capacitance, a distinct increase of the channel current. Upon bias stress the mobile, positively charged sodium ions (Na^+) are assumed to move to the negative biased drain electrode, whereas the negatively charged counter ions from sodium triflate are pushed into the direction of the source electrode. The latter however are assumed to be less mobile due to their size.

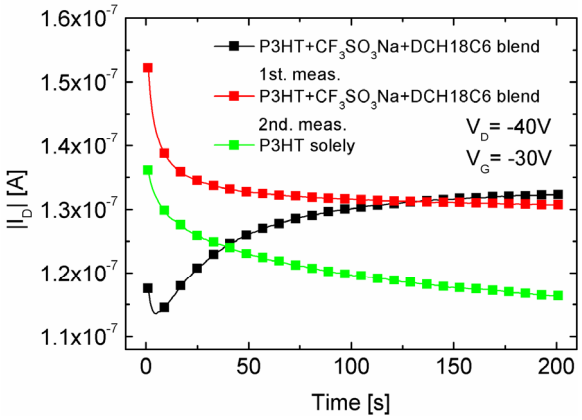

Figure 4.7: Channel current I_D at V_G=-30V and V_D=-40V as a function of time (L = 25 µm, W = 2.85 mm).

The less mobile counter ions form a negative space charge near the source electrode. As a consequence most likely electric double layers arise at the rr-P3HT/electrode interfaces, which reduce the injection and ejection barriers due to the associated high electric fields (see chapter 1.2.5 and Figure 4.8). This leads to an improved injection of mobile charge carriers at the source side, which would explain the observed increasing channel current. In addition to the electric double layer formation, electrochemical doping near the source/drain electrodes might also be responsible for the increasing channel currents.

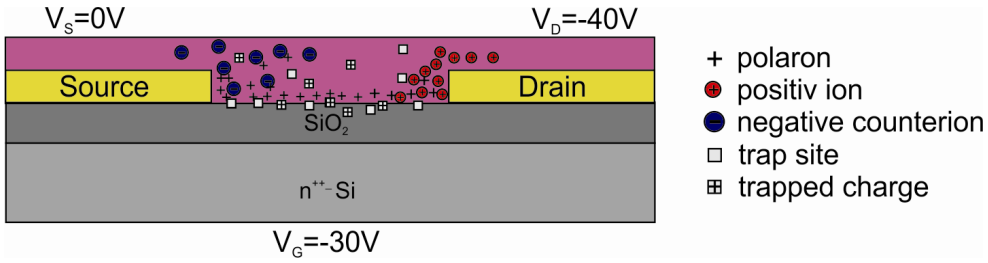

Figure 4.8: Scheme with possible explanation for channel current increase during time measurement at a certain working point.

The proposed explanation is supported by Edman and coworkers, who reported on an electrochemical method to improve charge carrier injection by mobile ions in the active layer of a thin film transistor.[47] They also mentioned the influence of the charge double layer on the contact resistance, which strongly depends on the width of the injection barrier. Accordingly, by reducing the latter due to the formation of a charge double layer, the contact resistance is decreased. This corresponds with our results, in particular when looking at the output characteristics of the ion-containing OFETs in Figure 4.6 (marked with an arrow) and at Figure 4.9. The reference device exhibits a change in curvature of a single output curve at low V_D, which results from the existence of a contact resistance. This is clearly not visible for the ion-containing OFET.

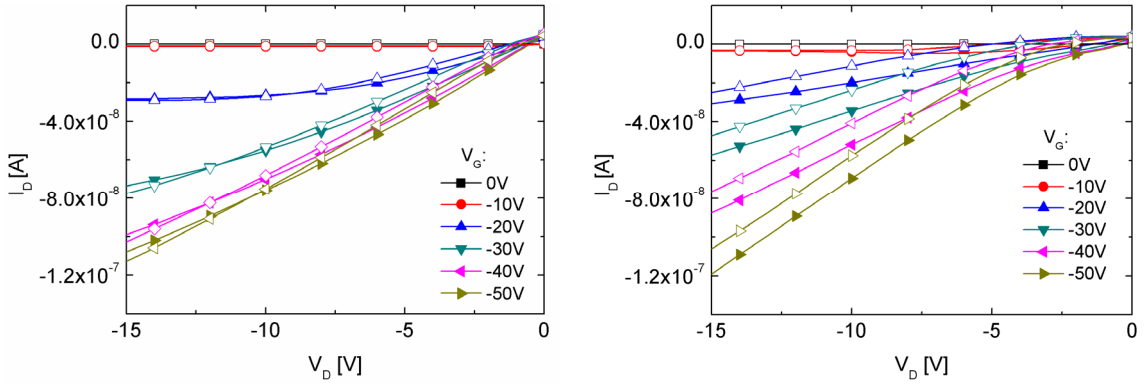

Figure 4.9: Zoomed output characteristics for low V_D of an ion-containing (left) and a reference device (right) for illustrating the difference in contact resistance (L = 25 µm, W = 2.85 mm).

After the first time measurement of the ion-containing OFETs a second measurement was performed, where only charge carrier trapping behavior could be observed. This might have resulted from the finite mobility of ions and therefore slow redistribution to gain equilibrium (between the measurements), meaning that the ions are still at the rr-P3HT/electrode interface and therefore charge carrier trapping is the dominant effect. That explains also the similar maximum channel current at 200s.

Moreover, field-effect mobilities μ_{FE} in the linear and saturation regime were extracted from the device characteristics (see Figure 4.6). In the saturation regime both devices exhibit similar mobility values, whereas the linear mobility of the rr-P3HT reference device is increasing with applied V_G, while the ion-containing device exhibit decreasing μ_{FE} with increasing V_G. For the latter, this might be attributed to higher trap densities within the active layer. Correspondingly the mobility decreases at higher V_G, because charge carriers are increasingly attracted to the dielectric/semiconductor interface, where trap densities are higher.[15]

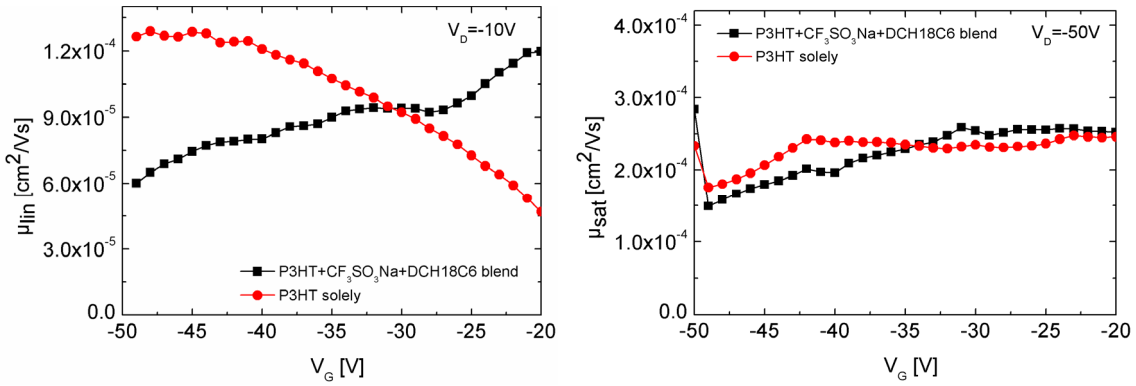

Figure 4.10: Field-effect mobility in linear (left) and saturation (right) regime of an OFET with incorporated ions (squares) and of a rr-P3HT reference device (circles) (L = 25 µm, W = 2.85 mm).

Figure 4.11 shows that the threshold voltage V_{th} for the OFET with deliberately added ions is more negative compared to the corresponding values of the reference device. Accordingly, also the switch-on voltage V_{so} is more negative for the ion-containing OFET (see Figure 4.12). This is attributed to more traps at the semiconductor/dielectric interface and/or within the bulk for ion containing OFETs.

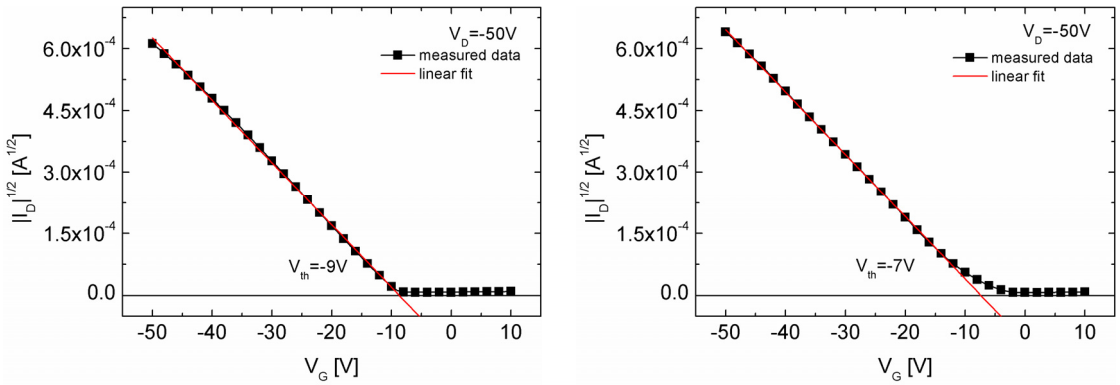

Figure 4.11: Transfer curves at V_D=-50V and corresponding linear fits; left: device based on rr-P3HT- CF_3SO_3Na-DCH18C6 blend (sample KSC13); right: reference device based on rr-P3HT (sample KSC12).

The subthreshold slope S is smaller for the devices containing ions (see Figure 4.12). This would indicate a smaller trap density at the semiconductor/dielectric interface for the ion-containing devices. However, when the injection of charge carriers is improved due to the influence of ions, the channel also forms “easier” and therefore the lower S might be a result of the lower injection barrier.

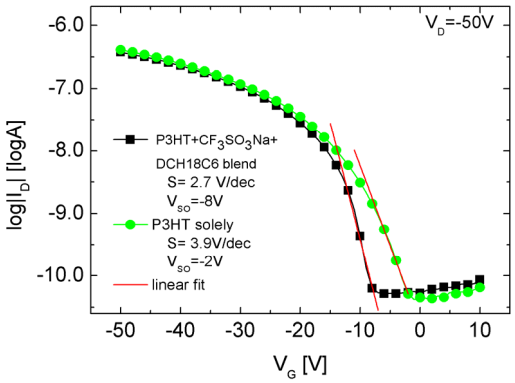

Figure 4.12: Semilogarithmic transfer curves V_D=-50V and extracted subthreshold slopes of a device based on rr-P3HT-CF_3SO_3Na-DCH18C6 blend (squares, sample KSC13) and areference device based on rr-P3HT solely (circles, sample KSC12).

Regarding the on/off-current ratio, it is in the same range for both devices. Table 4.1 summarizes the most important OFET parameters for both samples.

Table 4.1: Comparison of device parameters of a typical OFET based on P3HT-CF_3SO_3Na-DCH18C6 and a reference OFET based on rr-P3HT solely; V_{so}, V_{th}, and S were extracted from the transfer curves at V_D= - 50 V; μ_{lin} and μ_{sat} were calculated with equation (1.7) and (1.8);(L = 25 µm, W = 2.85 mm).

Parameter	P3HT-CF_3SO_3Na-DCH18C6 blend (sample KSC13)	P3HT solely (sample KSC12)
On/off- current ratio	$7.1x10^3$	$9.1x10^3$
Vso [V]	-8	-2
Vth [V]	-9	-7
S [V/dec]	2.7	3.9
μ_{sat} [cm^2/Vs], (V_G=-40V, V_D=-50V)	$2.0x10^{-4}$	$2.4x10^{-4}$
μ_{lin} [cm^2/Vs], (V_G=-40V, V_D=-10V)	$8.0x10^{-5}$	$1.2x10^{-4}$

4.4.1 Gate and Drain Bias Influence on the Performance of Ion-Containing OFETs

The influence of drain and gate bias stress on the device performance of an ion-containing OFET was separately investigated by performing corresponding bias stress measurements. Before and after the bias stress was applied, a transfer curve at V_D = -40 V was recorded. Figure 4.13 depicts the corresponding linear and semilogarithmic transfer curves (forward and reverse sweep) of a typical device with L = 10 µm.

First the influence of drain bias stress was investigated by applying V_D = -30 V and V_G = 0 V for 1 h. An increase of the on-current ($\Delta I_D \approx$ 240 nA, ~30 %) accompanied by an increase of hysteresis could be observed, which can be ascribed to the formation of a charge double layer and/or electrochemical doping at the electrode/semiconductor interface, hence resulting in a reduction of the injection/ejection barrier. This is also confirmed by the shift of the switch-on voltage V_{so} to more positive values (from -4 V to 2 V). The top scheme of Figure 4.14 illustrates the described behavior. The off-current is not much influenced by drain bias stress.

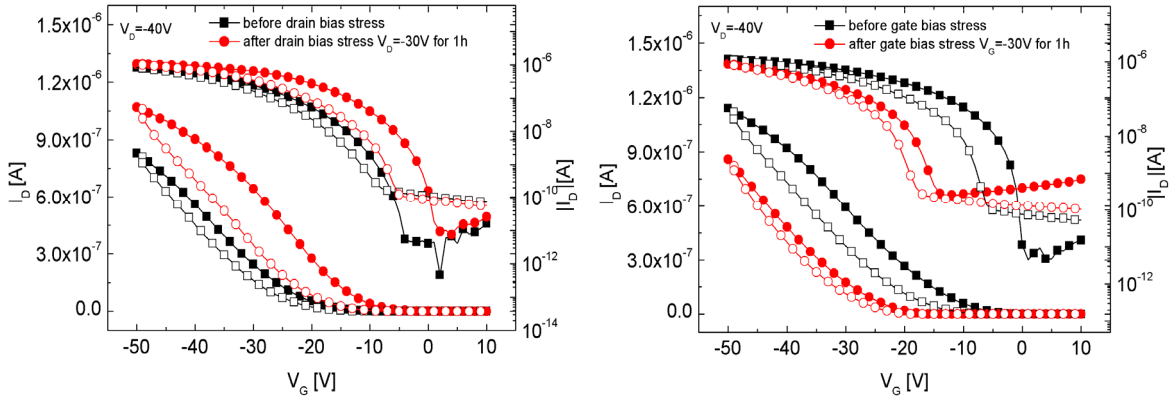

Figure 4.13: Transfer curves (linear and semi-logarithmic) at V_D = -40V of an OFET (L ~ 10 µm, W ~ 2.85 mm) based on rr-P3HT-CF_3SO_3Na-DCH18C6 before and after drain (left) and gate (right) bias stress; closed symbols: forward sweep; open symbols: reverse sweep.

In contrast the gate bias influence, where V_G = -30V and V_D = 0 V was applied for 1 h, results in a significant increase of the off-current (see Figure 4.13, right). The reasons for that is probably the release of positive charge carriers due to positive Na^+ ions attracted to the semiconductor/dielectric interface by the negative gate voltage. Moreover the switch-on voltage is significantly shifted to more negative values (V_{so} = -15 V) and the on-current is reduced ($\Delta I_D \approx$ 280 nA, ~30 %). Attracted Na^+ ions located at the semiconductor/dielectric interface after gate bias stress, can screen the gate field, which would explain the shift of V_{so} to more negative voltages (see Figure 4.14).

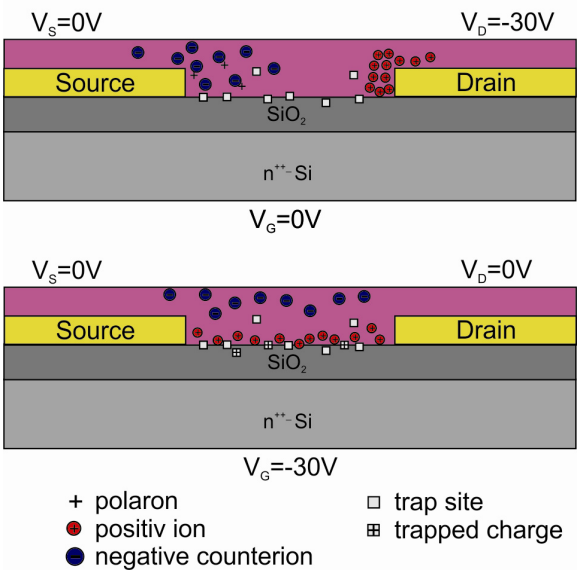

Figure 4.14: Scheme of possible explanation of ion movement in an OFET based on rr-P3HT-CF_3SO_3Na-DCH18C6 under bias stress.

4.5 Influence of Ions during Switching of Source/Drain Electrodes

For further investigations of the ion motion within the semiconductor the source/drain voltages were switched. More precisely, for a constant gate voltage (V_G = -30 V) the source/drain potential was changed from -40 V to 0 V, while at the same time switching the voltage applied at the source contact from 0 V to -40 V, now becoming the "new" drain electrode. Figure 4.15 schematically illustrates this voltage switching, where the function of source/drain electrodes are exchanged.

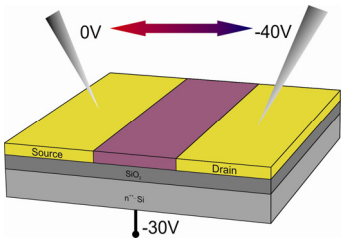

Figure 4.15: Scheme of OFET with applied voltages during the voltage switching.

The corresponding results are depicted in Figure 4.16: First a decrease of I_D can be observed that turns into an increase, according to the results of previous time measurements (see Figure 4.7). At the point, where the voltage is switched and the drain electrode becoming the new source and vice versa, a rapid decrease of I_D is observed that is followed by an increase. This decrease of I_D after switching was also seen for another ion-containing OFET on a sample from another series, where for two times the switching was performed (see Figure 4.17). A possible explanation can be that positive ions are first accumulated at the drain contact and after switching the injection is hindered by them, resulting in the lower observed current values. Another proposal was made by Bäcklund et al, who observed a similar behavior in OFETs containing ions.[49] They attributed the slower increase of the channel current to the ions which are modulating the latter and are responsible that the pinch-off is much faster than the doping due to diffusion/drift of ions. On the contrary, for reference devices based on rr-P3HT solely this decreased current and the slow increase was not observed (Figure 4.18). The corresponding gate current for both samples show peaks, possibly due to self-healing leakage currents or charging of the capacitance (see Figure 4.16, right).

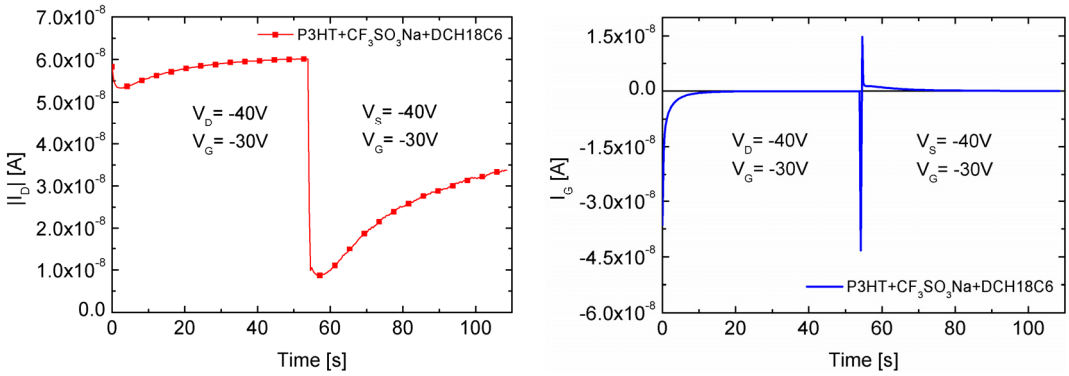

Figure 4.16: Source-to-drain channel current (left) and gate current (right) during switching of the source/ drain voltages of an OFET based on rr-P3HT- CF_3SO_3Na-DCH18C6 (L=25µm, W=2.85mm; KSC20).

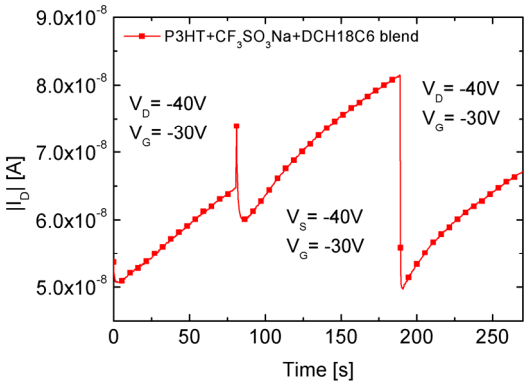

Figure 4.17: Source-to-drain channel current during two times switching of the source/ drain voltage of an OFET based on rr-P3HT- CF_3SO_3Na-DCH18C6 (L=25µm, W=2.85mm, KSC33).

Before and after switching the channel current is decreasing with time for the reference device, which can be attributed to charge carrier trapping. The current did not reach the original value measured before switching (after 160 s), which could be verified by extending the measurement time to longer periods (not shown). By looking at the time measurements for the ion-containing devices, such an offset can also be suspected (see Figure 4.16 and Figure 4.17) and therefore following investigations were done.

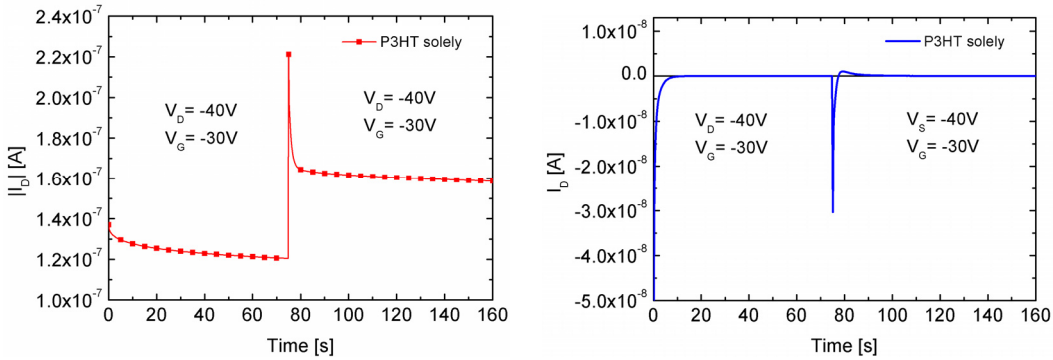

Figure 4.18: Source-to-drain channel current (left) and gate current (right) during switching of the source/ drain voltages of an OFET based on rr-P3HT solely (L=25µm, W=2.85mm; KSC21).

Single transfer curves were measured with the voltages at the source and drain contacts consecutively switched. Figure 4.19 depicts the transfer curves of a device with L = 10 µm (left) and L = 25 µm (right), where after switching a higher on-current was recorded. This observed asymmetry is significantly larger for shorter channels, indicating that the effect is most probably related with the contact, as contact effects are more relevant for shorter channel lengths. Moreover the influence of bias stress was also investigated using different measurement recipes, where also preliminary measurements were taken into account. Independent on the measurements performed before switching, sometimes a higher or lower channel current after switching the voltage was observed for various devices (not shown here). This showed that the observed asymmetry is independent to the device history, yielding a possible conclusion that it is rather a geometric effect e.g. different shape of the electrodes.

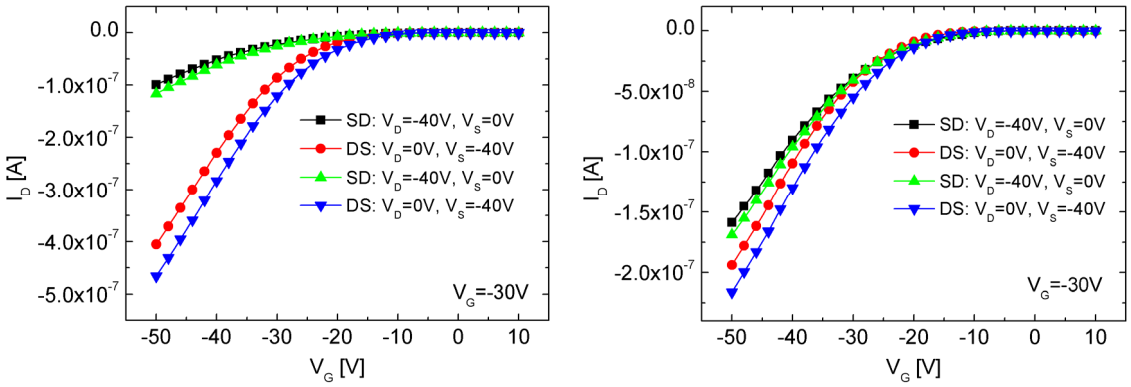

Figure 4.19: Consecutively recorded transfer curves of an ion-containing OFET L = 10 µm (left) and L = 25 µm (right) for different source/drain voltage configurations (sample KSC33; W=2.85mm).

The same measurements were performed with reference devices based on rr-P3HT solely. Figure 4.20 shows that the asymmetric behavior did not appear for long channel lengths (here 25µm) and was only slightly seen for 10µm channel length, which do not support the idea that the reason are

from geometric nature and that asymmetric contacts are the reason for the asymmetry. The pronounced asymmetric behavior was only seen for devices based on rr-P3HT-CF_3SO_3Na-DCH18C6 blend.

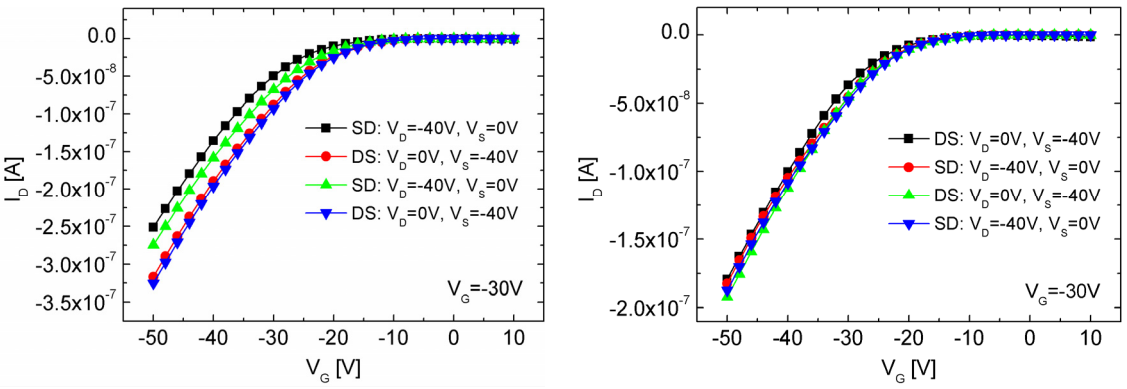

Figure 4.20: Transfer curves of an OFET based on rr-P3HT solely with L = 10 µm (left) and L = 25 µm (right) for different source/drain voltage configurations (sample KSC34, W=2.85mm).

Considering the AFM image shown in Figure 4.3, it can, however not be excluded that a non-uniform phase separation of rr-P3HT with CF_3SO_3Na-DCH18C6 is responsible for the pronounced asymmetry. If different phases are located near the contacts a change of the measured channel current could be observed with switching. This would also explain the equal distribution of the sometimes higher or lower measured channel currents after switching for several of OFETs. Nevertheless the asymmetric behavior is subject for future studies. Regarding also the slight asymmetry for the reference devices SEM or even TEM investigations can be useful to investigate the contact between electrode and semiconductor in more detail.

4.6 Summary and Conclusions

Basically, it was found that OFETs based on rr-P3HT-CF_3SO_3Na-DCH18C6 blend show similar device performance as reference devices based on rr-P3HT solely, regarding device parameters such as on-current, field-effect mobility and on/off-current ratio. This was also observed for OFETs based on rr-P3HT-DCH18C6 blend. The presence of ions could be clearly approved by several effects, namely larger hysteresis, lower switch-on voltage after drain bias stress and lower subthreshold slope and an increase of source-to-drain channel current with time. These effects are mainly ascribed to the formation of electric double layers at the semiconductor/electrode interface and/or electrochemical doping, the former resulting in lower injection and ejection barriers and thus a reduction of the corresponding contact resistances. Moreover, the ion containing OFETs exhibit a larger trap density due to a possible phase separation between the rr-P3HT with sodium triflate and DCH18C6, resulting in more negative switch-on voltages. Furthermore experiments for the ion-containing devices were performed, where the function of the source and drain electrodes were exchanged by switching the source/drain voltages, which led to a decrease of the source-to-drain channel current, followed by a slow I_D increase, being ascribed to the redistribution of ions within the organic semiconductor. Moreover by switching the voltage of source and drain an asymmetric behavior was observed which was more pronounced for OFETs with the rr-P3HT-CF_3SO_3Na-DCH18C6 blend films. One possible explanation found was that the non-uniform phase separations influence the injection at the electrodes, but for a detailed understanding of this effect further investigations are required.

5 OFETs with Polymer Electrolyte Dielectric Materials

Besides the investigation of ions within the organic semiconductors, this chapter deals with the effects of ions within the dielectric material. Regarding applications for ion sensing, top-gate/bottom-contact OFETs based on polyvinyl alcohol (PVA) and a novel ion-sensitive dielectric material were fabricated on n^{++}-Si/SiO_2 wafer substrates. The device architecture is based on the presented SensFET concept by Klug et al., where an additional functionalized sensitive dielectric layer is applied for the detection of low concentrations of ammonia.[53,25] The novel dielectric material used within this thesis consists of a copolymer based on dimethylester and norbornene units functionalized with dibenzo-18-crown-6 (DCH18C6). An example, where crown-ether functionalized polymer brushes with a selectivity towards potassium ions were successfully applied in quartz crystal microbalance sensors, was shown by Schüwer et al.[86]

In this chapter, OFETs with deliberately added ions within the functionalized DCH18C6-based polymer are thoroughly investigated in comparison to devices without ions as well as to reference devices based on a dielectric polymer containing dimethylester units solely. In particular sodium triflate was added to the solution of the DCH18C6-based polymer in order to study the effects of ions. Since PVA was used as intermediate dielectric layer to prevent the semiconducting layer from dissolution, the ion conducting properties of PVA can be also utilized for OFETs with added ions. The effects of ions within PVA were already in detail investigated by us and others, including hysteresis effects, electric double layer formation and electrochemical doping. [53,54,87] Moreover, the applied dielectrics were also studied in capacitor structures, including capacitors based on different PVA grades (Mowiol 5-88, 4-98 and 6-98).

5.1 Materials and Solution Preparation

As mentioned, the applied sensitive dielectric material is a norbornene based copolymer, consisting of 5 mol% of sensitive material copolymerized with non-sensitive reference material (endo,exo-bicyclo[2.2.1]hept-2-ene-5,6-dicarboxylic acid dimethylester). The sensitive monomer is a norbornene with a functionalized side chain, namely dibenzo-18-crown-6 (DCH18C6), whereas the reference material (1b) is the homopolymer of the non-sensitive monomer. The corresponding chemical structures are depicted in Figure 5.1. Both polymers were synthesized by the group of Prof. Slugovc[88] by means of ring opening metathesis polymerization (ROMP). For simplification the polymer with the functionalized crown ether side chain will be referred to as DCH18C6-based polymer (1a). The number average molecular weight M_n and the polydispersity index PDI were

determined to be: M_n=7820 g/mol, PDI=1.817 for the DCH18C6-based polymer and M_n=48730 g/mol, PDI=1.08 for the reference polymer.

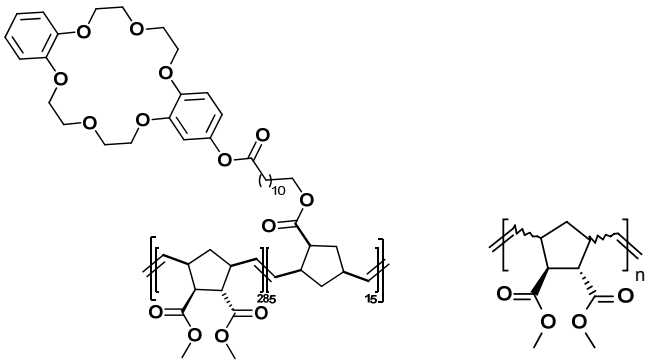

Figure 5.1: Chemical structure of the DCH18C6-based polymer (1a, left) and reference polymer (1b, right).

Figure 5.2 (left) shows the DCH18C6-based material with its olive-green appearance. Solutions of the DCH18C6-based polymer and the reference polymer were prepared with a concentration of 60 mg/ml in spectrally clean $CHCl_3$ under argon atmosphere. This rather high concentration was chosen to yield thick enough layers for low gate leakage currents. In addition, blend solutions of the polymer with sodium triflate were prepared as follows: Sodium triflate and the DCH18C6-based polymer were weighed in a vial in a mass ratio of ~ 50:1 (DCH18C6-based polymer: sodium triflate) and dissolved in $CHCl_3$, obtaining a solution of 60 mg/ml with respect to the DCH18C6-based polymer. This mass ratio corresponds to a mol ratio of ca. 1:1 and ensures that one mol of sodium triflate corresponds to ~ 4 units of DCH18C6. For comparison also a blend solution of the reference polymer with sodium triflate was prepared as well with a similar mass ratio. All four solutions were stirred overnight and are depicted in Figure 5.2. As predicted, the sodium triflate was hardly dissolved for the reference solution even after heating to 50°C for 10 min, which was ascribed to the absence of crown ether. The other mixtures showed were good solubility in $CHCl_3$.

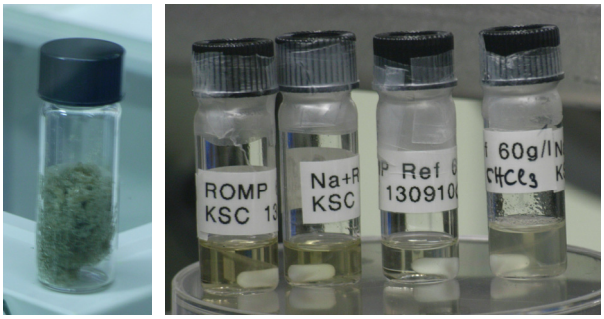

Figure 5.2: DCH18C6-based polymer (left) and corresponding 60 mg/ml solution in $CHCl_3$ without and with sodium triflate (first two solutions; right); solutions of reference polymer without and with sodium triflate (last two solutions, right).

5.2 Capacitors based on Different Polyvinyl Alcohol (PVA) Grades and Novel Functionalized Polymer with DCH18C6

Within the frame of this thesis also three different grades of polyvinyl alcohol (PVA), namely Mowiol 5-88, 4-98 and 6-98, were characterized in capacitor structures on glass substrate. PVA was used as an intermediate dielectric layer for OFETs, which are described in chapter 5.3, to prevent a re-dissolution of rr-P3HT film by $CHCl_3$, since the DCH18C6-based polymer (1a) is also dissolved in $CHCl_3$. Capacitors based on DCH18C6-based polymer (1a) with and without sodium triflate and as well as the reference polymer (1b) were also fabricated and investigated in detail.

5.2.1 Device Fabrication

As substrate 1" x 1" glass pieces covered with indium tin oxid (ITO) were used. Two conducting ITO stripes, exhibiting a sheet resistance of 15 ohm/sq, were structured by etching. The stripes were masked with an adhesive tape and tin powder was applied to enhance the etching reaction in a 37 % HCL acid. Afterwards the standard cleaning procedure described in chapter 2.1.1 was applied and the substrates were transferred into the glove box to perform a dehydration bake at 120°C for 1h in high vacuum. The dialyzed PVA hydrogels of Mowiol 5-88 (9 wt %), 4-98 (8.3 wt%) and 6-98 (8.3 wt%) were prepared as described in chapter 2.2.2, and spin-cast with 1500 rpm for 60 s on the glass substrates. The prepared films were dried first at 60°C for 30 min and then at 110-120°C for 3 h or overnight in high vacuum ($p \sim 3x10^{-5}$ mbar). The films of the DCH18C6-based polymer (1a) and reference polymer (1b) were similarly prepared, except that the films were dried on the hotplate at 60°C for 15 min in argon. The corresponding film thicknesses were measured with AFM and are listed in Table 2.1. For the top electrode 90 – 100 nm silver (Ag) was thermally evaporated through a comp-shape mask with a deposition rate of ~ 8 Å/s ($p \sim 10^{-6}$ mbar). Then the devices were transferred to another glove box and conductive silver was applied to obtain good contact to the ITO and silver electrodes. Figure 5.3 shows the capacitor device architecture (left) and the corresponding device (right) from a typical sample with 8 capacitors (middle).

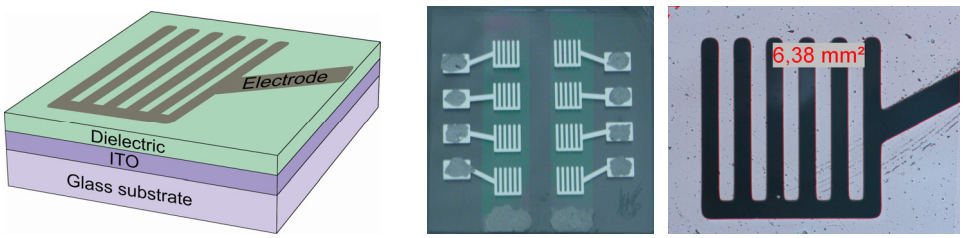

Figure 5.3: ITO/dielectric/Ag-capacitor architecture (left) and corresponding sample (CAP1) with 12 capacitors based on the DCH18C6-based polymer (1a) (middle); single device with Ag comb-shaped electrode exhibiting an effective area of A = 6.38 mm² (right).

In order to investigate the film of the novel sensitive polymer, AFM images were recorded. Figure 5.4 shows the topographic image of the DCH18C6-based polymer layer of a fabricated capacitor. The film exhibits a rather smooth surface and the surface roughness was determined to $R_q \sim 0.5$ nm. AFM investigations were carried out under ambient conditions and therefore were performed after the electrical characterization.

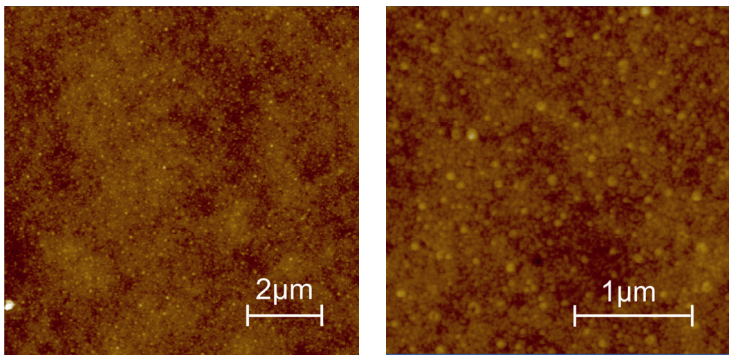

Figure 5.4: Topographic AFM image of the DCH18C6-based polymer (1a) film (d = 860 nm, $R_q \sim 0.5$ nm) of the capacitor; scan size: 10 µm (left) and 3 µm (right); color code from black to white corresponds to a z-data range of 10 nm.

5.2.2 Device Characteristics

5.2.2.1 Frequency Dependence

The first measurement performed was a frequency sweep as described in chapter 2.4.1.1. The absolute impedance |Z| and the phase angle Θ were recorded in dependence of the frequency at a test signal amplitude of 1 V_{RMS}. The measured values of |Z| and Θ for all 5 different dielectric materials are depicted in Figure 5.5 for a frequency range of 100 Hz to 100 kHz. The frequency dependence of the impedance for capacitors is in accordance with the equation of the capacitive reactance $X_C \propto 1/\omega C$. As known, ideal capacitors exhibit a phase angle of -90° and resistors 0°. Figure 5.5 shows that the capacitors based on DCH18C6-based polymer and the reference polymer show almost ideal behavior whereas the PVA capacitors have a larger ohmic contribution. This ohmic contribution can be possibly ascribed to mobile ions, resulting from residual acetat content (see chapter 2.2.2).

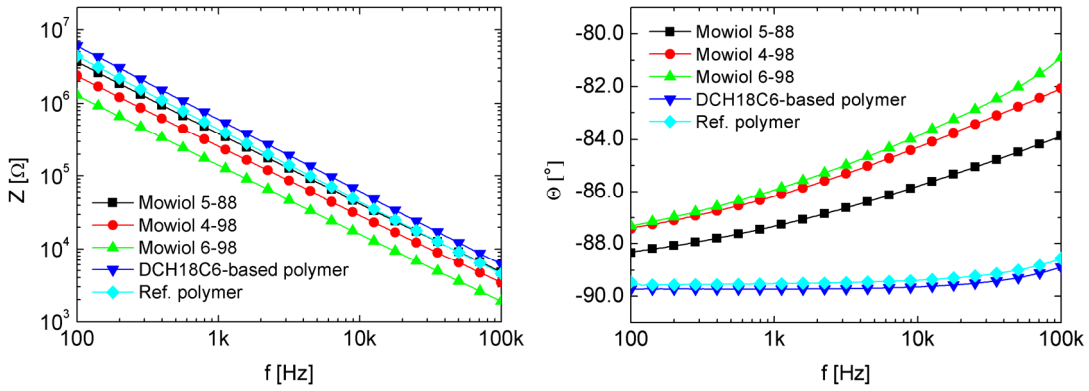

Figure 5.5: Absolute impedance |Z| and phase angle Θ as a function of frequency of typical ITO/dielectric/Ag – capacitors.

For calculating the corresponding capacitance and resistance values an equivalent circuit model was used. Rather small capacitance values lead to high capacitive reactance X_c values and therefore the parallel resistance R_p becomes more significant and a parallel circuit model was chosen.

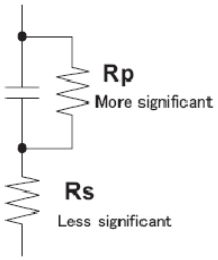

Figure 5.6: Equivalent parallel circuit model for small capacitances (taken from [89]).

A parallel circuit can be described by following equations (ω: angular frequency of applied test signal):

$$\frac{1}{Z} = \frac{1}{R_p} + \frac{1}{X_c} = \frac{1}{R_p} + j\omega C_p \tag{6.1}$$

$$\frac{1}{Z} = \frac{1}{|Z|} + e^{-j\theta} = \frac{1}{|Z|}(\cos\theta - \mathrm{j}\sin\theta) \tag{6.2}$$

By comparison of the coefficient of equation 6.1 and 6.2 the parallel capacitance and parallel resistance are obtained as:

$$C_p = -\frac{1}{\omega\,|Z|}\sin\theta \tag{6.3}$$

$$R_p = \frac{|Z|}{\cos\theta} \tag{6.4}$$

Figure 5.7 depicts the calculated parallel capacitance and parallel resistance from the recorded |Z| and Θ values in dependence of the frequency. The capacitance is constant for the DCH18C6-polymer and the reference polymer. As expected, for all capacitors based on the 5 tested dielectric materials the parallel resistance is decreasing with increasing frequency, becoming more conductive at higher frequencies. The capacitors based on PVAs exhibit lower R_p values and also a C_p-frequency dependence could be observed in comparison to the novel dielectric materials. This can most likely ascribed to mobile ions within PVA due to residual acetate content. The difference in capacitance and resistance values of the different grades of PVA can be explained by the difference in the corresponding film thickness.

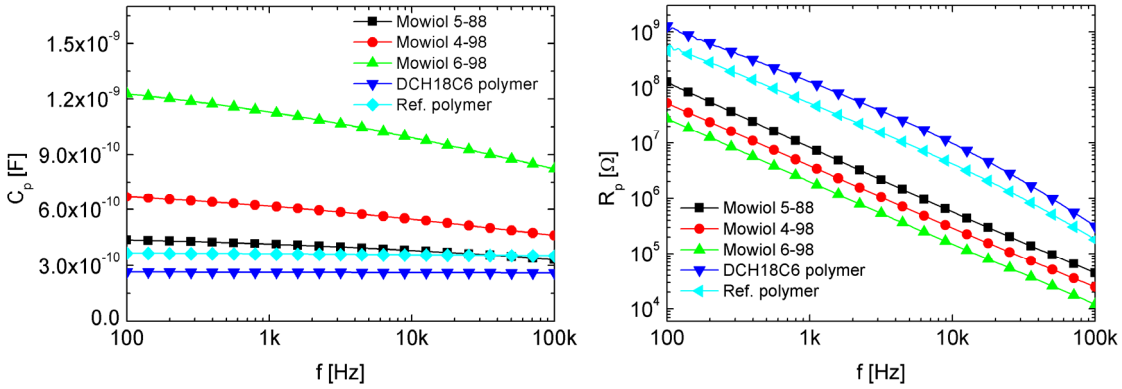

Figure 5.7: Parallel capacitance and resistance as a function of frequency of typical ITO/dielectric/ Ag – capacitors.

The relative permittivity ε_r of the used dielectric materials was calculated with eq. (6.5) with C_p being the capacitance at 1 kHz, d the layer thickness, A the capacitor area and ε_0 the vacuum permittivity. The film thickness was measured with AFM and the capacitor area was determined with using an opticale microscope (see Figure 5.3, right).The averaged relative permittivities of several devices are listed in Table 5.1.

$$\varepsilon_r = \frac{C_p \cdot d}{\varepsilon_0 \cdot A} \tag{6.5}$$

The values obtained for the PVAs are in accordance with literature values which are between 6 and 10.[90,91] The relative lower value for the partially hydrolyzed PVA (Mowiol 5-88) probably results from the lower content of OH-groups[72,g], leading to a less polar material. In contrast, the DCH18C6-based polymer and the reference polymer exhibit a relative permeability ε_r value of 4.2 at a frequency of 1 kHz and are therefore comparable to former results in our group.[25] Contrary to the expectations the film thicknesses for the polymers with larger number average molecular weight were thinner. This is obvious for the reference polymer (M_n = 48730 g/mol) in comparison

[g] Fully hydrolyzed PVA exhibit more OH-groups (and less acetat- ($OCOCH_3$-) groups).

to the DCH18C6-based polymer (M_n = 7820 g/mol) and by comparing Mowiol 6-98 with the other PVA grades (M_n listed in Table 2.1). However the reason for that could not be clearly identified.

Table 5.1: Average relative permittivity (calculated according to equation 6.5 and averaged over 4 devices of one sample) and layer thickness of different PVA grades and new polymer dielectrics

Dielectric	*d* [nm]	ε_r at 1kHz
Mowiol 5-88	1000	7.7
Mowiol 4-98	830	9.3
Mowiol 6-98	470	10.4
DCH18C6-based polymer (1a)	860	4.2
Reference polymer (1b)	580	4.2

5.2.2.2 DC Bias Dependence

In order to investigate the operational stability of the capacitors, a DC bias sweep was performed as described in chapter 2.4.1.1. The impedance and the phase angle were recorded at a test signal frequency of 1 kHz and 1 V_{RMS} by sweeping the superimposed DC bias from -40 V to 40 V starting from 0 V. The corresponding parallel capacitance and resistance were calculated with eq. (6.3) and eq. (6.4). In Figure 5.8 the corresponding values are presented for the capacitors based on PVA and Figure 5.9 shows the corresponding capacitance and resistance for the DCH18C6-based polymer (1a) and reference polymer (1b).

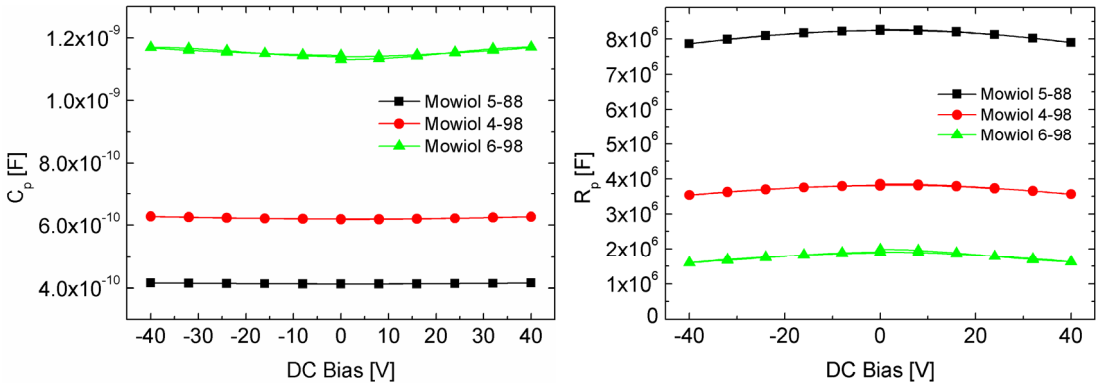

Figure 5.8: Parallel capacitance C_p and resistance R_p as a function of DC bias of capacitors based on various PVA grades (C_p and R_p calculated from impedance and phase angle).

The capacitors based on the different PVA grades show a rather stable performance and no significant hysteresis between forward and reverse sweep could be observed. Only a slight DC bias dependence occurred which can be again ascribed to mobile Na^+ ions within the layers, resulting from residual actetat content. Against one's expectations this dependence was more pronounced for

capacitors based on Mowiol 6-98, for which a similar ion content was assumed. However, this can be most likely explained by the thinner layer thickness of Mowiol 6-98 films (d~470nm) in comparison to the other capacitors and therefore the effective electric field strength is larger, causing the stronger DC bias dependence.

For capacitors based on the DCH18C6-polymer (1a) and the reference polymer (1b) no significant DC bias dependence of the capacitance was observed, whereas the resistance of the reference polymer revealed distinct voltage dependence. Not all devices measured showed a stable behavior. Moreover, for devices with incorporated ions no stable operation under DC bias application could be obtained. This is reflected in the bias dependence of the parallel resistance (see Figure 5.9, right) and may be ascribed to a non homogeneous layer due to the added salt. The DC bias dependence of the capacitors based on the reference polymer can be most likely explained by the thin layer (580 nm) and therefore higher electric field strength in comparison to the other capacitors and can also result from mobile ions contained in the pristine material. Nevertheless this investigation showed that the application of the presented dielectrics in capacitor architecture reveal functioning devices with satisfying relative permittivity values for the applications in OFETs.

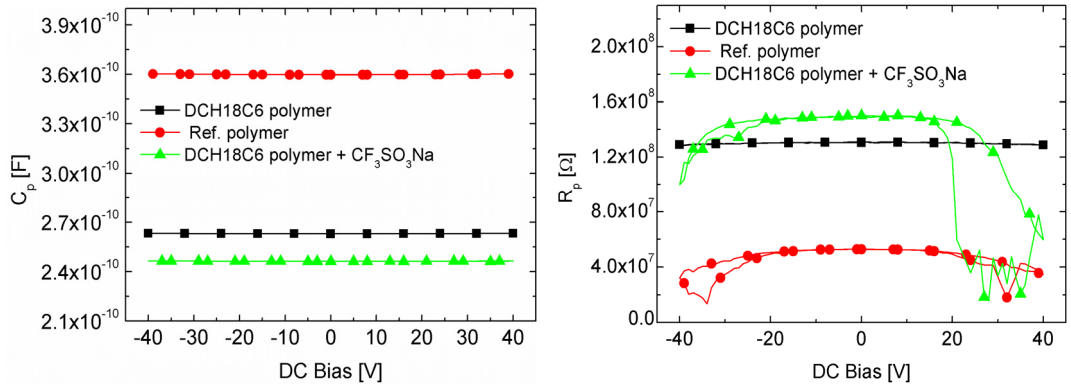

Figure 5.9: Parallel capacitance C_p and resistance R_p as a function of DC bias of capacitors based on DCH18C6-polymer and reference polymer (C_p and R_p calculated from recorded impedance and phase angle).

5.3 TG/BC OFETs with Electrolyte Dielectrics Applicable for Ion Sensing

TG/BC OFETs based on the novel ion sensitive dielectric material functionalized with DCH18C6 (polymer (1a)) and OFETs based on the reference polymer were fabricated on n^{++}-Si/SiO_2. Since rr-P3HT and the DCH18C6-based polymer are soluble in organic solvents such as toluene and $CHCl_3$, an intermediate dielectric layer had to be applied to prevent the rr-P3HT layer from being dissolved. In particular water-based PVA (Mowiol 5-88) was chosen as intermediate layer due to its resistance and impermeability to most organic solvents and ion conducting properties.[72,90] The device architecture is shown in Figure 5.10. In order to investigate the behavior of ions within the dielectric, ions sodium triflate was added to the DCH18C6-based polymer film by adding sodium triflate to the solution (see section 5.1). For comparison devices based on the DCH18C6-based polymer without added ions and on the reference polymer without crown ether side groups were applied as dielectric layers. As top gate a meander-shaped silver electrode was chosen to enable direct contact between an analyte and the ion-conducting dielectric, when in later investigations an electrolyte would be drop-cast on the device (see Figure 5.10).

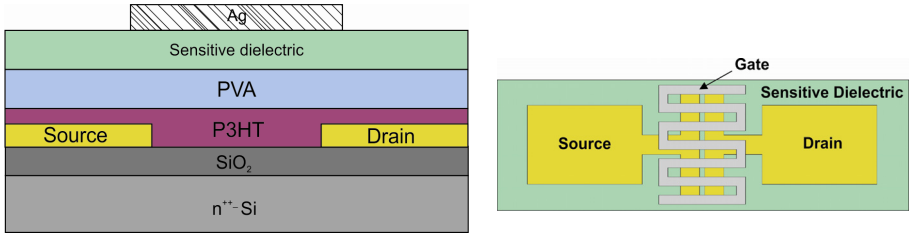

Figure 5.10: Cross section (left) and top view (right) of the device architecture of a TG/BC OFET based on electrolyte dielectric materials.

5.3.1 Device Fabrication

As substrate n^{++}-Si/SiO_2 with photolithographically structured source/drain electrodes was chosen and the samples were fabricated according to the explanation in chapter 2.3, including dehydration bake, deposition of rr-P3HT (2 mg/ml, toluene) and application of the PVA layer. As gate dielectric the PVA grade Mowiol 5-88 with a concentration of 9 wt% was spin-cast onto the sample and dried at 60°C for 30 min and 3 h at 110°C in high vacuum. Then the prepared DCH18C6-based polymer solution with and without ions as well as the solution of the reference polymer was spin-cast with 1500 rpm for 40 s and dried on the hotplate for 15 min at 60°C. Finally two 100 nm thick silver meander-shaped top gate electrodes covering 6 devices were thermally evaporated ($p < 10^{-6}$ mbar) and the sample was attached to a cooper plate with conductive silver. Figure 5.11 shows a typical sample and a single device.

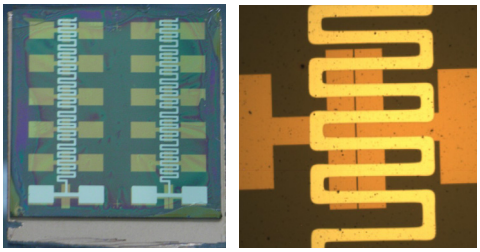

Figure 5.11: Sample with 12 TG/BG OFETs based on DCH18C6 functionalized dielectric layer with two common meander-shaped top gate electrodes (left) and single device (L ~ 25 µm, W ~ 2.85 mm).

Figure 5.12 shows the AFM-height image of the dielectric double layer, PVA + DCH18C6-based polymer, in an OFET device, exhibiting a very smooth surface. The surface roughness was obtained to R_q ~ 0.5 nm and the double layer has a thickness of d = 1320 nm. For the OFETs based on the reference polymer a layer thickness of d = 1470 nm and R_q ~ 0.5 nm was determined. AFM investigations were carried out under ambient conditions and therefore were performed after the electrical characterization.

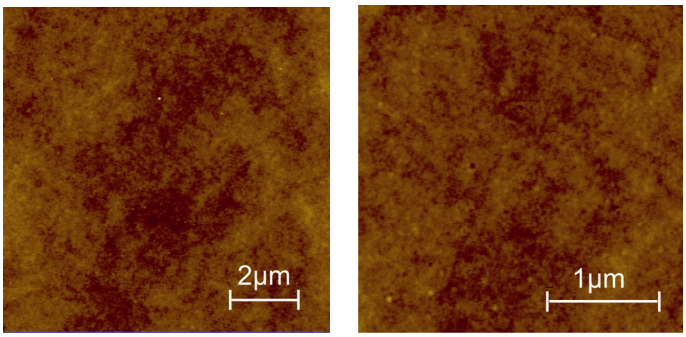

Figure 5.12: Topographic AFM image of the dielectric double layer PVA + DCH18C6-based polymer (1a) film (d = 1320 nm, R_q ~ 0.5 nm) of a typical OFET (KSC29); scan size: 10 µm (left) and 3 µm (right); color code from black to white corresponds to a z-data range of 10 nm

5.3.2 Comparison of TG/BC OFETs based on DCH18C6-Polymer – CF_3SO_3Na with Devices based on DCH18C6-Polymer and Reference Polymer

Figure 5.13 depicts the transfer and output characteristics of typical OFETs based on DCH18C6-polymer with added CF_3SO_3Na (top) and DCH18C6-polymer solely (middle) in comparison to the OFET based on the reference polymer (bottom). The OFETs with the deliberately added ions within the dielectric layer exhibits a significantly larger on-current in comparison to the other devices, namely 800% larger than for OFETs based on DCH18C6-polymer solely. This pronounced larger on-current can be ascribed to the ions within the dielectric layer, forming an electric double layer (EDL, see section 1.2.5) and for leading to electrochemical doping at the PVA/semiconductor interface. This is also in accordance with the results presented by Klug et al.[25] The added ions (Na^+), originating from the sodium salt, are assumed to be mobile due to the crown ether units on the polymer chain of the novel dielectric material and the counterions are possibly less mobile due to their size. Most likely these Na^+ ions diffuse into the PVA layer and the semiconductor. Moreover, in the output characteristics of OFETs with the added ions, the source-to-drain current did not saturate at high voltages due to ions moving near the drain contact and reducing the depletion width for $|V_D|>|V_G|$. In comparison to the transfer curves the I_D values in the output characteristics are larger at the same working point. Here high gate voltages are longer applied and the effects due to ions are most likely stronger. By comparing the on-current of the device based on DCH18C6-polymer solely with the one based on the reference polymer, smaller I_D values are observed for the former. This lower on-currents for the device based on DCH18C6-polymer solely are a sign for charge-trapping behavior, which is also confirmed by the larger hysteresis in the output characteristics, where the channel current is decreasing for the reverse sweep and the larger subthreshold slope, indicating a larger interfacial trap density (see Table 5.2). In contrast, the hysteresis observed for devices based on the reference polymer exhibit larger drain currents for the reverse sweep, which can possibly ascribed to ions within PVA. On the other hand the drain currents are decreasing for the reverse sweeps in the output characteristics due to charge carrier trapping. Regarding the hysteresis for devices with deliberately ions a hysteresis occurred, where the channel current is increasing for the reverse sweep for the transfer and the output characteristics, resulting from the added mobile ions. Charge carrier trapping might also happen for the ion-containing device, but is covered by the effects resulting from ions. Although PVA is used as intermediate layer and ions are also present for devices without deliberated added ions, corresponding effects are not as dominant as for the OFETs based on polymer-DCH18C6 + CF_3SO_3Na. The maximum leakage currents of the devices are in the range of ~ 30 nA.

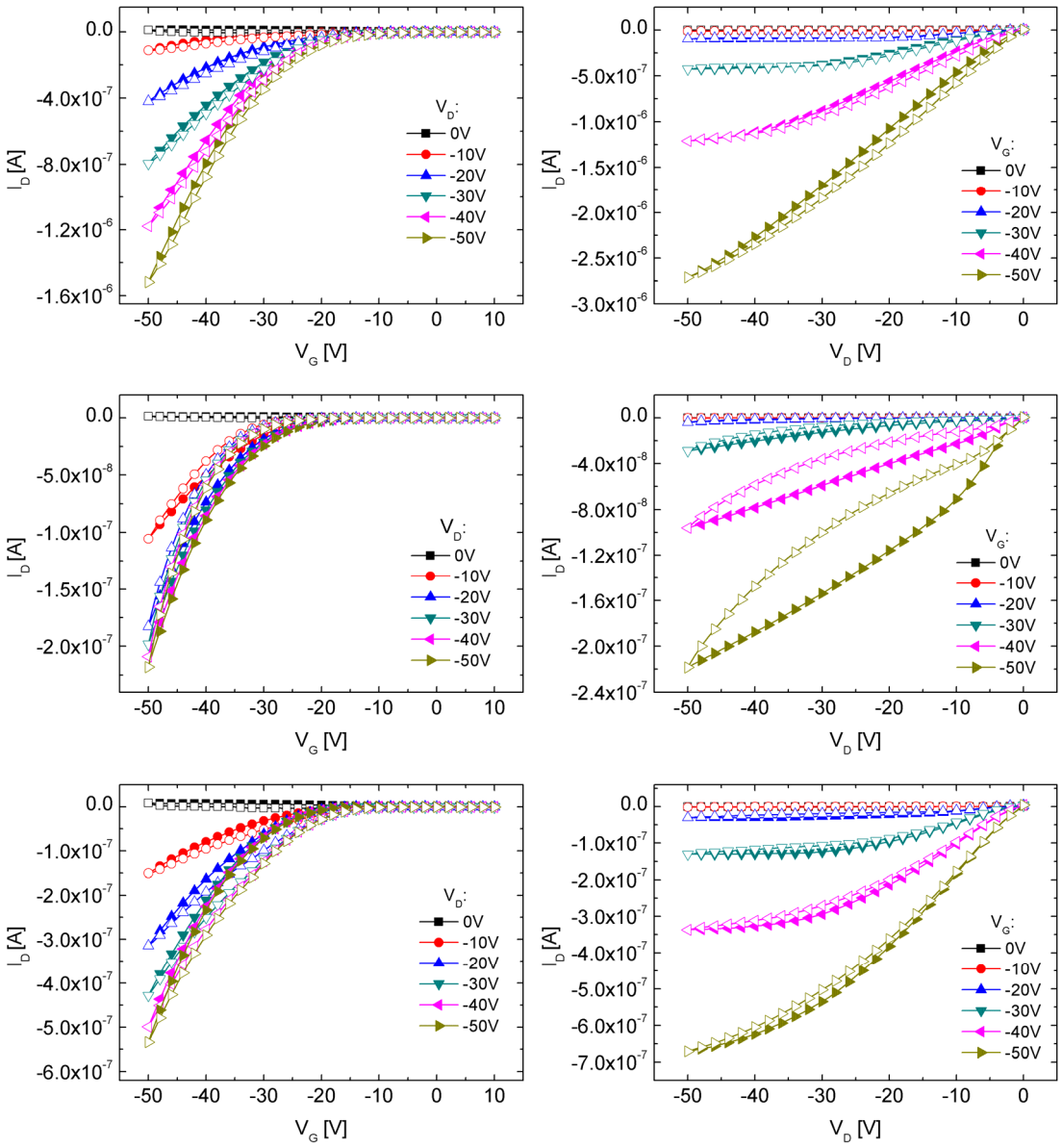

Figure 5.13: Transfer (left) and output (right) characteristics of rr-P3HT based OFETs (L ~ 25 µm, W ~ 2.85 mm); top: device with DCH18C6-polymer + CF_3SO_3Na (sample KSC38); middle: device with DCH18C6-polymer (sample KSC29); bottom: device with reference polymer (sample KSC26); closed symbols: forward sweep; open symbols: reverse sweep.

The extracted device parameters are depicted in Table 5.2. The highest mobility values in the saturation regime were obtained for the OFET based on DCH18C6-polymer with ions. For the linear regime they exhibited similar field-effect mobilities. The threshold voltage and switch-on voltage exhibited negative values but, were shifted to more positive values for ion containing devices after the measurement of all devices on a sample due to bias stress, applied through the common gate. Moreover, the higher trap density at the interface for OFETs based on polymer-DCH18C6 solely, obvious when regarding the decreasing current for the reverse sweep for the output characteristics, is also reflected in the larger subthreshold slope in comparison to the

other devices. Again, the effect of traps in the ion-containing device might be covered by the dominant ionic effects.

Table 5.2: Comparison of device parameters typical OFETs based on DCH18C6 polymer+CF_3SO_3Na, DCH18C6-polymer solely and a reference OFET (L ~ 25 µm, W ~ 2.85 mm); V_{so}, V_{th}, and S were extracted from the transfer curves at V_D= - 50 V; μ_{lin} and μ_{sat} were calculated with equation (1.7) and (1.8); C_i was calculated assuming a dual layer dielectric with relative permittivity values from Table 5.1 and corresponding layer thickness (d=730 nm for each of the layers for devices based on DCH18C6-polymer, and d=660 nm for devices based on the reference polymer, respectively).

Parameter	DCH18C6-based polymer+CF_3SO_3Na	DCH18C6-based polymer	Reference polymer
On/off- current ratio	$1.9x10^3$	$1.6x10^4$	$3.3x10^3$
Vso [V]	-3	-2	-14
Vth [V]	-9	-16	-16
S [V/dec]	2.1	6.1	2.5
C_i [nF/cm^2]	3.6	3.6	3.3
μ_{sat} [cm^2/Vs], (V_G=-30, V_D=-50V)	$5.4x10^{-3}$	$0.7x10^{-3}$	$2.2x10^{-3}$
μ_{lin} [cm^2/Vs], (V_G=-40, V_D=-10V)	$1.3x10^{-3}$	$1.1x10^{-3}$	$1.6x10^{-3}$

5.3.2.1 Operational Stability

For further investigations of the effects of ions various bias stress measurements were performed. First the channel currents were measured at a certain fixed working point (V_G=-30V, V_D=-40V) for 200 s. In Figure 5.14 and Figure 5.17 the corresponding source-to-drain channel currents are shown (black squared curve).

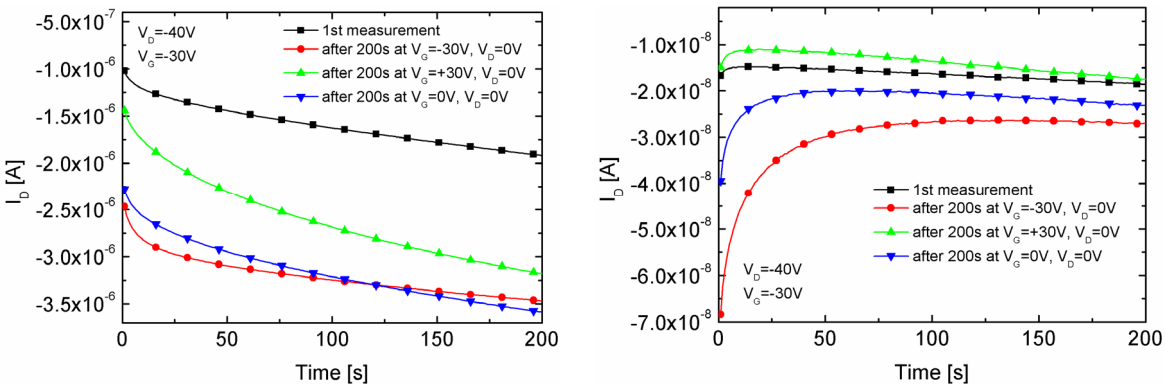

Figure 5.14: Source-to-drain channel currents at V_D=-40 V and V_G=-30 V as a function of time of OFET based on DCH18C6 polymer + CF_3SO_3Na (left) and DCH18C6-polymer solely (right) (L ~ 25 µm, W ~ 2.85 mm).

The channel current is increasing for all three devices due to mobile ions within the dielectric layers. The increase is more pronounced for the OFETs based on the DCH18C6 polymer + sodium triflate. This is depicted in Figure 5.15:, where normalized channel currents are compared. The channel currents were normalized to the currents measured after 50 s to avoid an influence of charging and leakage current in the beginning of the measurement to the relative current increase. The OFETs based on the DCH18C6-polymer with the incorporated ions showed the largest relative increase. This confirms that as of course expected the highest amount of ion is formed within the DCH18C6-polymer with added sodium triflate. As already mentioned the current is increasing because of the high electric fields at the semiconductor/dielectric interface due to the formed EDLs and possible electrochemical doping.

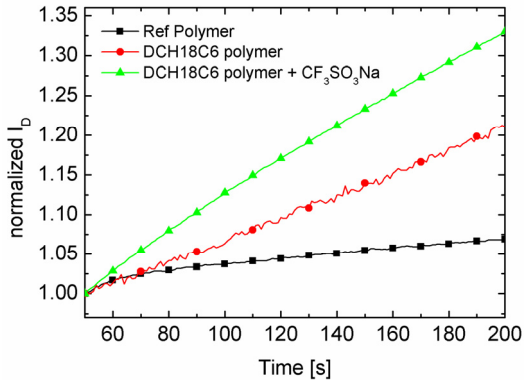

Figure 5.15: Normalized source-to-drain currents at V_D=-40 V and V_G=-30 V as a function of time.

A possible explanation of the corresponding ion arrangement for the corresponding bias stress condition is shown in Figure 5.16 left. For simplification the two dielectric layers are combined to one layer. Moreover, the mobile Na^+ ions may also be able to diffuse into the P3HT layer near the negative drain contact, reducing the contact resistance and influencing the pinch off region. The larger increase of the channel currents obtained for the devices based on the DCH18C6-polymer in comparison to the reference can be possibly ascribed to the movement of the ions, resulting from residual acetate content, into the DCH18C6 polymer, being also mobile within the latter due to the additional crown ether group. The fact that the devices with deliberately added ions showed an increase lower than expected is due to the fact that all devices had been stressed already during recording of the transfer and output characteristics of all devices.

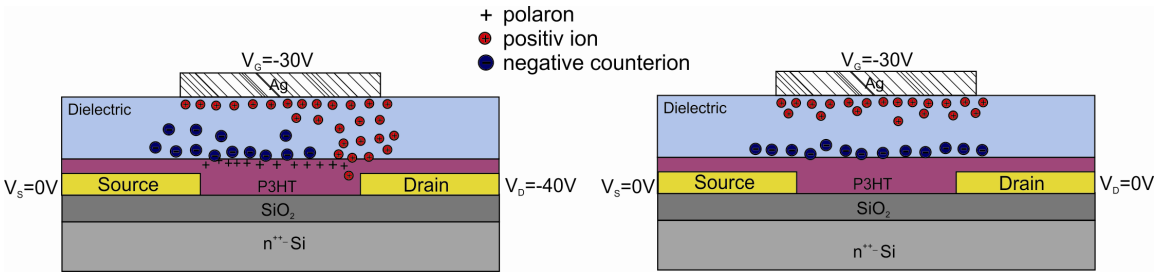

Figure 5.16: Possible arrangement of ions under different bias stress conditions.

To investigate the behavior of ions in more detail channel currents where recorded at fixed drain and gate voltages (described above) after various bias stress conditions for 200 s. Figure 5.14 depicts the corresponding graphs for the DCH18C6-polymer with and without ions. The increase of channel current for the 1st measurement was already discussed above. The second measurement was performed after applying -30 V at the top gate for 200 s, resulting in a significant increased channel current. Upon gate bias stress positive ions move to the negative charged electrode and the less mobile counterions leave a negative space charge, yielding to the already described formation of EDLs (see Figure 5.16, right). Due to the enhanced gate field the drain current is larger after the gate bias stress (beginning of red curves), which is more pronounced for the devices based on polymer-DCH18C6. The drain current is increasing with time for OFETs with deliberately added ions whereas the channel current of devices based on polymer-DCH18C6 decreases with time for the measurements after the gate bias stress application. This decrease can be most likely ascribed to the higher trap density for the device based on DCH18C6-polymer solely. Moreover the I_D values are two orders of magnitude smaller with the DCH18C6-polymer without ions, so that trapping effects are much more pronounced, which corresponds to the larger hysteresis in the output characteristics and also leakage currents have a larger effect.

Subsequently a positive gate bias stress ($V_G = +30$ V) was applied and the recorded drain current exhibited smaller values in the beginning (green curve) in comparison to the previous measurement. In detail the positive ions are pushed to the semiconductor/dielectric interface, where they hinder the formation of a conducting channel but since ions are assumed to rearrange rapidly, this explains the larger increase of the current with time compared to the black curve.

The application of $V_G = 0$ V and $V_D = 0$ V yielded apparently only a relaxation of the ions due to electrostatic forces. This results in slightly smaller values in comparison to the values at which the green curve stopped. For the device without deliberately added ions all corresponding recorded $I_D(t)$ curves reveal charge carrier trapping behavior. The higher trap density within this device therefore covers the ionic effects resulting from PVA.

Similar measurements were performed for a typical OFET based on the reference polymer as dielectric layer (see Figure 5.17). Qualitatively the results are similar to the one obtained for the device based on DCH18C6 polymer with ions, except that the effects are less significant.

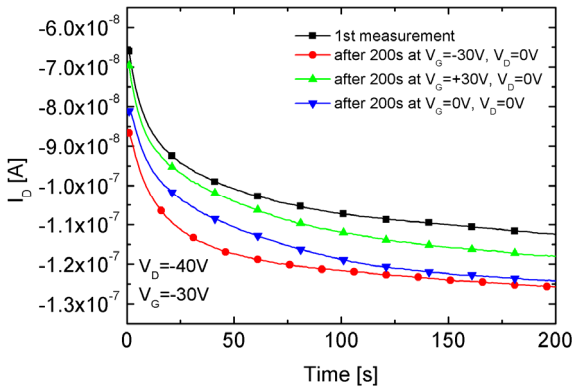

Figure 5.17: Source-to-drain channel currents at V_D = -40 V and V_G = -30 V as a function of time of OFET based on reference polymer (L ~ 25 µm, W ~ 2.85 mm).

Before and after these bias stress measurements, transfer characteristics were recorded. Figure 5.18 and Figure 5.19 depict the corresponding linear and semilogarithmic transfer curves at V_D = -50 V. For the device based on polymer-DCH18C6 + CF_3SO_3Na a significant increase of the on-current is observed due to ions and their corresponding effects mentioned before. Moreover, the switch-on voltage is shifted to more positive values and the off-current is significantly increased, which can be ascribed to mentioned ionic effects. Obviously the transfer curve before bias stress exhibited a positive V_{so} in comparison to the value depicted in Table 5.2, which is ascribed to the bias stress applied through the common gate. A slight shift of the switch-on voltage as well as an increased off-current was also observed for devices based on polymer-DCH18C6 solely, since ions are also present in the PVA layer but was not as pronounced as for devices with deliberately added ions. For the OFETs based on the reference polymer similar characteristics before and after the applied bias stress were observed.

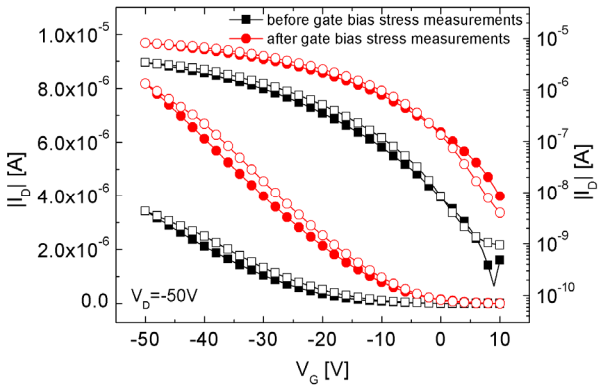

Figure 5.18: Transfer curve (linear and semi-logarithmic) at V_D = -50 V of OFET (L ~ 25 µm, W ~ 2.85 mm) based on DCH18C6-polymer + CF_3SO_3Na before and after gate bias stress measurements; closed symbols: forward sweep; open symbols: reverse sweep.

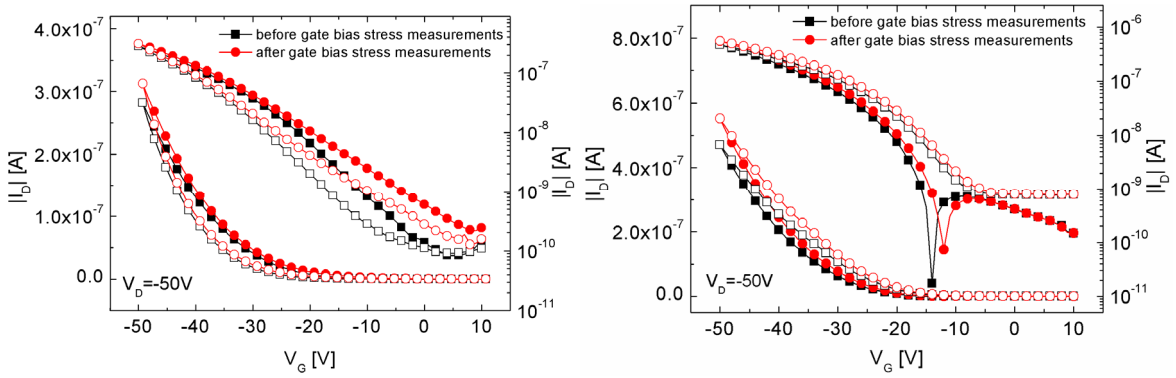

Figure 5.19: Transfer curves (linear and semi-logarithmic) at V_D = -50 V of OFETs (L ~ 25 µm, W ~ 2.85 mm) based on DCH18C6 solely (left) and reference polymer (right) before and after gate bias stress measurements; closed symbols: forward sweep; open symbols: reverse sweep.

Furthermore, in order to study the behavior of ions within the dielectric under varying the gate voltages and the effect of drain and gate bias stress the following measurements were performed. Transfer curves at V_D= - 40 V were recorded after various gate and drain bias stress conditions for 200 s, similar to the bias stress conditions above.[h] Figure 5.20 depicts the corresponding graphs. In accordance to the results above, a significantly increased on-current could be observed for the OFETs based on DCH18C6 polymer + sodium triflate (see Figure 5.20, top) after gate bias stress, which was not so pronounced for OFETs without deliberately added ions. Moreover the off-current slightly increased for both samples based on DCH18C6-polymer, which can be seen in the semilogarithmic transfer curves and can be ascribed to high electric field (EDLs) and/or electrochemical doping at the semiconductor/dielectric interface. Due to previously performed measurements an already positive switch-on voltage was observed for the first measured transfer curve and is increasing under gate bias stress for the device based on DCH18C6 solely. A distinct decrease of on-current after applying V_G = +30 V occurred for both samples based on DCH18C6 polymer, corresponding to the results above. In contrast to the first measurement series above now also a drain bias stress was applied. For both signs of applied drain bias, an increase of the on-current is shown in Figure 5.20 for the ion-containing OFETs (top), which can be however rather ascribed to the gate voltage influence during the transfer measurement than to the drain bias stress. The ions can also diffuse into the rr-P3HT layer near the electrodes causing effects discussed in detail in chapter 4. In contrast, the OFETs based on the reference polymer did not yield any altered behavior after bias stress. In general this measurement showed that the effects such as increased on/off-currents, switch-on voltage shift are more pronounced for the devices with DCH18C6 polymer + sodium triflate and can therefore clearly ascribed to mobile ions.

[h] The measurement time of one single transfer curve is approximetly 30 s.

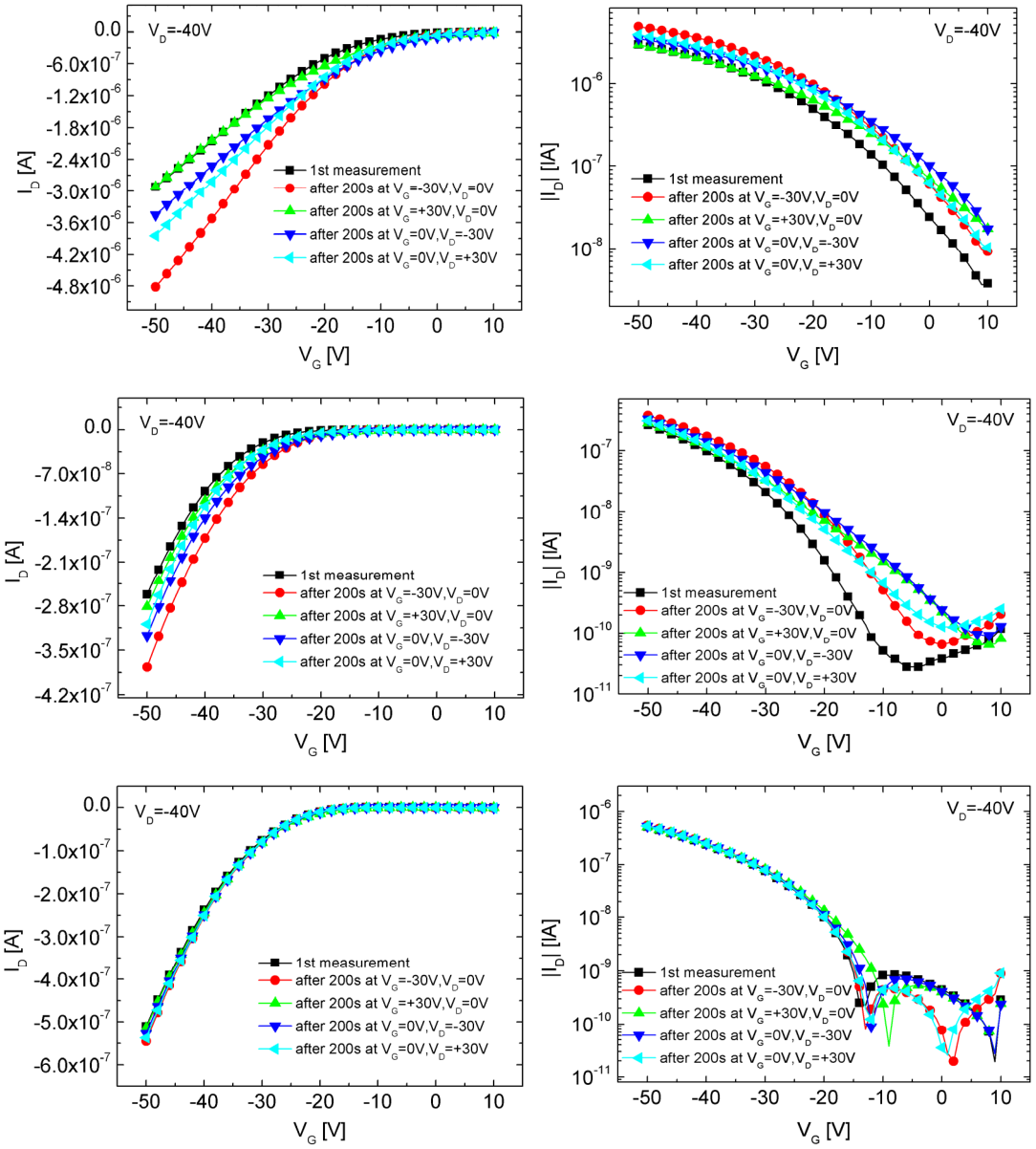

Figure 5.20: Linear (left) and semilogarithmic (right) transfer curves after various bias stress conditions for rr-P3HT OFETs (L ~ 25 µm, W ~ 2.85 mm); top: device with DCH18C6-polymer+CF_3SO_3Na (sample KSC38); middle: device based on DCH18C6-polymer solely (sample KSC29); bottom: device with reference polymer (sample KSC26).

5.3.2.2 Dual-Gate OFET Issues

Considering the device architecture and the applied voltages during operation as well as the possible leakage currents e.g. between the top-gate (TG) and the bottom-gate (BG), the highly n-doped Si substrate, which is used as bottom-gate, should not be disregarded. It cannot be excluded that due to the top-gate field and/or high leakage currents between the TG and BG an electrical potential arises at the BG, since the Si is highly n-doped and therefore highly conducting.

In order to investigate this in more detail transfer characteristics of rr-P3HT TG/BC OFETs with PVA as dielectric layer[i] were recorded first with floating bottom-gate and then applying $V_{BG} = 0$ V during top-gate operation (see corresponding scheme in Figure 5.21).

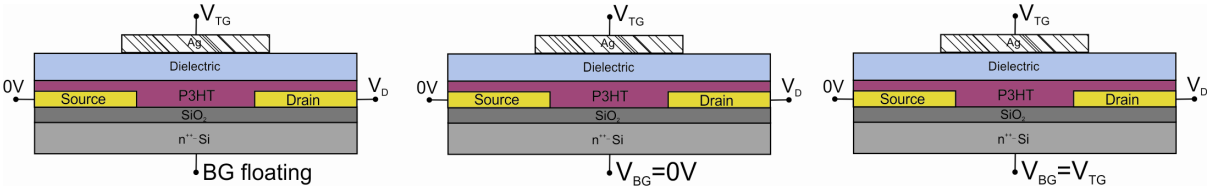

Figure 5.21: Schemes of different applied BG biasing conditions.

Figure 5.22 shows the corresponding transfer curves. A significant decreased on-current could be observed when 0 V is applied to the bottom gate, namely from -8.3×10^{-6} nA to -2.2×10^{-6} nA (at $V_D = -50$ V, $V_G = -50$ V). This indicates that when the bottom gate is floating most likely a negative potential arises which possibly can induce a second conducting channel at the rr-P3HT/SiO_2 interface, increasing the source-to-drain channel current.

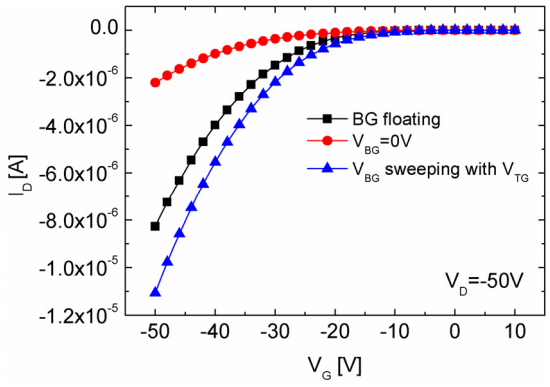

Figure 5.22: Linear transfer curves rr-P3HT OFET with PVA as dielectric layer (sample KSC9, L ~ 25 µm, W ~ 2.85 mm) for different bias condition of the bottom-gate.

To investigate this proposed dual channel behavior, the bottom-gate was also swept parallel to the TG from 10 V to -50 V and back. Figure 5.22 shows the corresponding transfer curve at $V_D = -50$ V, where an increased channel current, which is also slightly larger in comparison to the

[i] The fabrication of these devices was similar to the one depicted in chapter 5.3.1, except that the application of the additional novel polymer layer was skipped.

operation with floating bottom-gate, was observed. This might be explained by the formation of a second conducting channel, yielding a dual channel OFET, which also supports the assumption that during floating bottom-gate operation when sweeping the TG a corresponding electrical potential arises at n^{++}-Si. However also the leakage currents between the top- and the bottom-gate must be considered, which were rather high for devices based on PVA. This high leakage current might most probably be responsible for the setting of an electrical potential at the BG.

In comparison to that similar measurements were performed for a double layer OFET, in particular a rr-P3HT TG/BC OFET based on polymer-DCH18C6 and PVA (sample KSC29, see chapter 5.3). The leakage current between the TG and the BG was rather small for this device and was measured to ~ 5 nA. In accordance with the measurements above, transfer characteristics were recorded with BG floating and by applying a voltage of $V_{BG} = 0$ V. Again a significant decreased on-current was observed for $V_{BG} = 0$ V (see Figure 5.23).

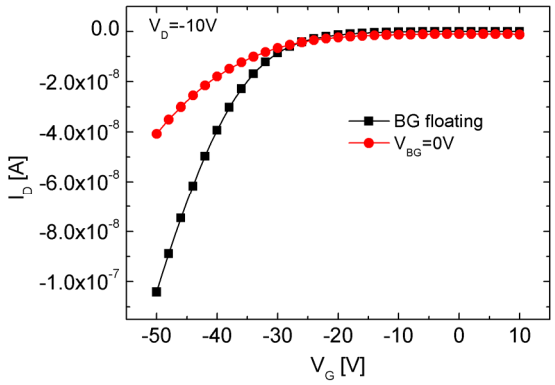

Figure 5.23: Linear transfer curves rr-P3HT OFET with PVA as dielectric layer (sample KSC29, L ~ 25 µm, W ~ 2.85 mm) for different bias condition of the bottom-gate.

Basically during the operation of a TG OFET the electrical potential at the n^{++}-Si is not known. In order to understand this issue in more detail, further investigations have to be done, including the fabrication and characterization of TG OFETs on e.g. glass substrates.

5.3.3 Influence of Water and a Sodium Triflate Solution on Dielectrics based on DCH18C6-functionalized Polymer

Based on the results above the next step regarding the investigations of the novel gate dielectric polymer functionalized with DCH18C6 as sensitive layer included the direct exposure of the polymer to an analyte. Since the polymer is functionalized with dibenzo-18-crown-6 also a selectivity to certain cations was expected, in particular considering also literature reports.[86] For these first investigations a capacitor device architecture was chosen. In particular ITO/dielectric/Ag-capacitors based on DCH18C6-polymer were tested. The fabrication process and electrical characterization is presented in chapter 5.2. Figure 5.24 schematically illustrates a possible interaction of a sensitive dielectric functionalized with DCH18C6 with an ion-containing analyte, including the diffusion of ions into the dielectric layer and the formation of a complex between the cations and the crown ether units on the polymer chain.

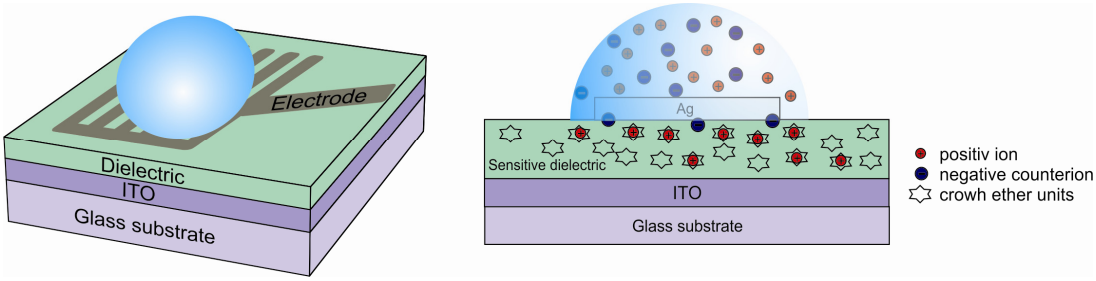

Figure 5.24: Schematic illustration of a possible interaction of a sensitive dielectric polymer with an ion-containing analyte.

Corresponding to OFETs with deliberately added ions within the dielectric layer, a solution of sodium triflate with a concentration of 0.5 mol/l in deionized water was drop-cast (5 µl) onto one capacitor during the measurement of the impedance $|Z|$ and the phase angle θ of a test signal amplitude of 1 kHz and V_{RMS}=1 V. Since silver electrodes were used for the top electrode and a direct exposure of these electrodes to the solution cannot be avoided due to the architecture, oxidation processes were observed, enhanced by the application of a voltage (see Figure 5.25, (a), (b)). This resulted in degradation of the devices.

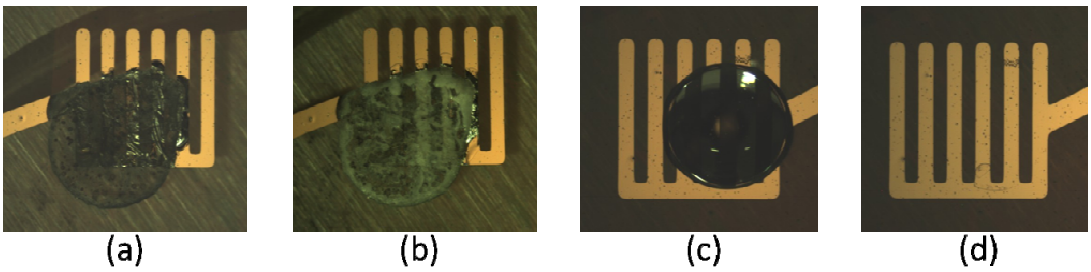

Figure 5.25: ITO/dielectric/Ag – capacitor directly after drop-casting of 0.5 mol/l solution (a) and after one week (b); Capacitor with DI H_2O droped on top of it (c) and after evaporation of the water droplet (d).

As a consequence, for further studies capacitors with gold (Au) top electrodes were fabricated. The fabrication process was similar to the one depicted above except that 70 nm Au was thermally evaporated with a deposition rate of 2 Å/s instead of 90 nm Ag. The electrical characterization of the capacitors based on polymer-DCH18C6 with Au top electrode in comparison to devices with Ag electrodes revealed a larger ohmic contribution, which is obvious by lower phase angles θ and lower parallel resistance R_p (see Figure 5.26). This can be most likely ascribed to the diffusion of gold particles into the dielectric layer being responsible for the larger ohmic contribution.

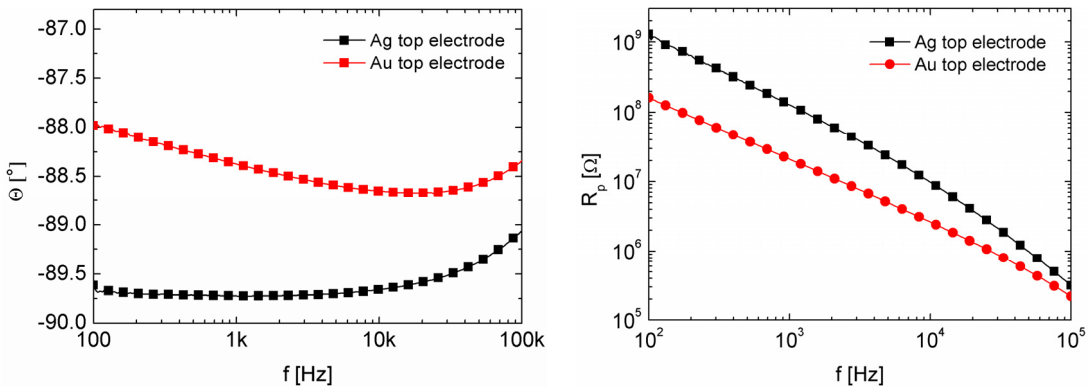

Figure 5.26: Phase angle Θ (left) and parallel resistance R_p (right) as a function of frequency of typical capacitor based on the polymer-DCH18C6 with Au and Ag top electrodes.

The polymer layer was not dissolved or delaminated by water as can be seen in Figure 5.25 (c), (d). This was also confirmed by AFM investigations (not shown).

The ITO/dielectric/Au – capacitors were also exposed to sodium triflate dissolved in deionized water with a concentration of 0.05 mol/l. The impedance |Z| and the phase angle θ were recorded at a test signal amplitude of 1 V_{RMS} and 1 kHz during drop-casting the solution with ions and deionized water (DI H_2O). Figure 5.27 depicts the calculated parallel resistance and capacitance values as a function of time during the analyte exposure. Qualitatively a more pronounced effect was observed with the CF_3SO_3Na solution so that it is suggested that ions have the larger influence. In particular the R_p values are strongly reduced as the conductivity of the dielectric is increased. This is also found with DI H_2O most likely due to residual ions within the water.

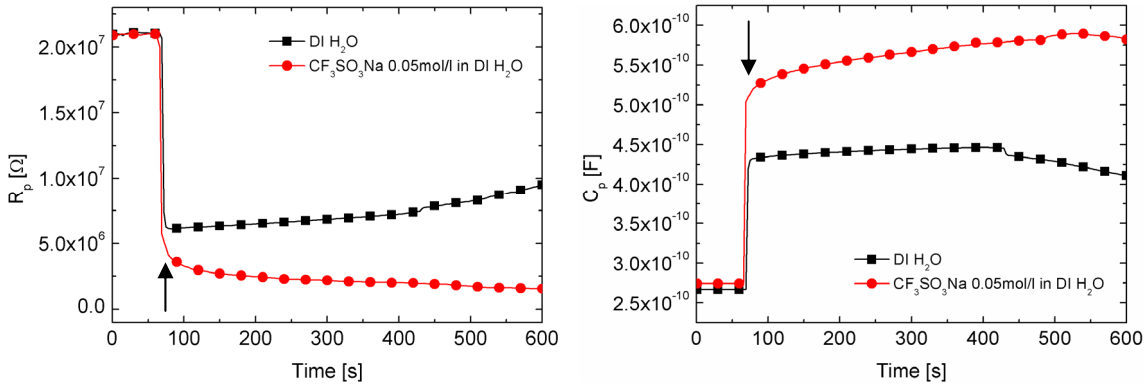

Figure 5.27: Parallel resistance (left) and capacitance (right) as a function of time during drop-casting of DI H_2O with and without sodium triflate (0.05 mol/l) (at a test signal 1 V_{RMS} 1 kHz); different devices on the same sample were used for each analyte exposure; arrows indicate the onset of exposure to the ion-containing solution.

Regarding possible applications in OFETs, the operational stability of the capacitors during the drop-casting of the solution was tested by sweeping a superimposed DC bias at a test signal amplitude at 1 V_{RMS} and a frequency of 1 kHz, as done in chapter 5.2.2. During this measurement the device exposed to sodium triflate solution was completely destroyed due to a strong chemical reaction at the Au electrode and the dielectric layer. Even for the exposure to DI H_2O a reaction could be observed (see Figure 5.28). This shows that the applied voltages were too high for such applications. Since the dielectric layer is very thin (800nm) very large electric fields are present, which destroys the device by application of water. The micrograph in Figure 5.28 exhibits brown spots which look like burned regions due to Joule's heat.

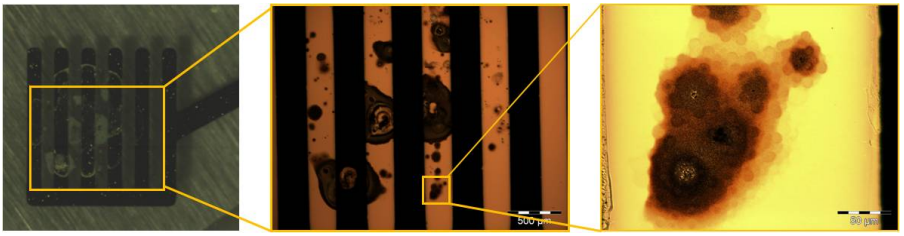

Figure 5.28: ITO/dielectric/Au – capacitor after performed DC bias measurement during DI H_2O exposure (left); micrographs show different section of affected regions with different magnifications (middle, right).

In order to apply the ion-sensing concept for OFETs, these problems first have to overcome. This includes that the applied voltages have to be decreased. The reduction of applied voltages is accompanied by the development of low-voltage OFETs. The direct contact of the analyte with the electrode should be avoided also in order to enable the application of rather cheap electrode materials such as silver. This could be achieved by another electrode design and encapsulation of the electrodes. Moreover to investigate the sensitivity and selectivity of the functionalized polymer standard ion solution should be used in order to reduce the influence of other ions present.

In conclusion, although several difficulties have to overcome in order to achieve a fully developed sensor device for ion-detection, the presented OFET concept is very promising, considering the results of the OFETs based on the polymer-DCH18C6 with deliberately added ions.

5.4 Summary and Conclusions

In this chapter the effect of ions within the dielectric layer were investigated, when polymer electrolyte dielectrics including polyvinyl alcohol and a novel norbornene-based polymer functionalized with dibenzo-18-crown-6 as well as its reference polymer were applied in TG/BC OFETs. Moreover, the electrical characterization of capacitors based on various PVA grades (Mowiol 5-88, 4-98 and 6-98) and the novel dielectric materials revealed a stable operation upon DC bias for all materials and the obtained dielectric constant can be depicted in Table 5.1. rr-P3HT based TG/BC OFETs with deliberately added ions within the functionalized DCH18C6-based polymer exhibited significant larger on-currents namely up to 800% large in comparison to devices based on DCH18C6-polymer solely and to OFETs with the reference polymer as dielectric layer. These higher on-currents can be ascribed to the formation of an electric double layer (EDL) at the semiconductor/dielectric interface due to ions, leading to high electric fields and to electrochemical doping. Moreover, various bias stress measurements yielded source-to-drain channel current drifts for all devices, since PVA was used as intermediate layer, which exhibits ions from residual acetate content. In contrast to the reference devices, the OFET based on DCH18C6-polymer + sodium triflate showed a significant higher on/off-currents and switch-on voltage shift to more positive values after the performed bias stress measurements which can be explained by the formed EDLs and electrochemical doping at the semiconductor/dielectric interface. Consequently after studying the effects of ions within the gate dielectric, first experiments concerning sensing applications were carried out. In particular, capacitors based on the novel dielectric polymer functionalized with DCH18C6 were exposed to a 0.05 mol/l sodium triflate solution and deionized water. First results demonstrated that the top electrodes and the dielectric layer are affected by the solution, in particular when a DC bias is applied. Besides the investigations of ions within the dielectric, the influence of the highly n-doped Si as substrate regarding a possible dual gate operation was investigated.

6 Flexible OFETs with Inkjet-Printed Source/Drain Electrodes

This chapter deals with the implementation of inkjet-printing as a low-cost fabrication technique for bottom-gate (BG) and top-gate (TG) OFETs as first steps on the way to an all-solution processed inkjet-printed low voltage OFET sensor. The corresponding work included the optimization of inkjet-printing of electrodes on various substrates. Based on the results in chapter 4 and 5, BG/BC rr-P3HT based OFETs with silver (Ag) inkjet-printed source/drain (S/D) electrodes on n^{++}-Si/SiO_2 substrates were thoroughly compared with corresponding devices based on evaporated chromium/gold (Cr/Au) S/D electrodes, structured with photolithography. Moreover also TG/BC OFETs including PVA as gate dielectric with inkjet-printed silver S/D electrodes were fabricated and electrically characterized, exhibiting low voltage operation. Besides that the inkjet-printing process was also optimized for flexible substrates such as PET films (Mylar®), PEN films (Teonex®) and PI films (Kapton®). Accordingly, flexible TG/BC OFETs with inkjet-printed S/D electrodes were fabricated and characterized. As PVA was chosen as gate dielectric, ionic drifts are also studied within this chapter. Moreover, the faced challenges associated with the fabrication process will be discussed in detail. Parts of the presented data within this chapter can also be found in a publication ("*Organic field-effect transistors applicable for gas and ion detection*", A. Klug, K. Schmoltner, E. J. W. List).

6.1 Inkjet Printing of Electrodes and Process Optimization

Besides using n^{++}-Si/SiO_2 substrates (oxide thickness: 200 nm, dimensions: ~1 inch x 1 inch) S/D electrodes were also inkjet-printed on flexible substrates such as Kapton® (film thickness d=128µm), Mylar® (d=350µm) and Teonex® (d=125µm) films.[92] Kapton® films are based on polyimide, Mylar® foils are made of polyester and Teonex® is a polyethylene naphtalate film. A standard cleaning process was applied as described in chapter 2.1.2, where in principle all following fabrication steps are mentioned. For the S/D electrodes a silver nanoparticle (NP) ink (CABOT CCI 300)[65], which is optimized for piezoelectric inkjet-printing, was used. The inkjet printing was carried out with an ITI XY MDS Printer with Apollo II printhead support kit with a multi-nozzle (Spectra SE-128 AA) system and a resolution of 400 dpi and 800 dpi. In principle the S/D structure is the same as for the photolithographically structured devices with varying channel lengths, which are given by the restricted printing resolution (e.g. from L ~ 32 µm to 127 µm for 800 dpi). The final obtained channel length further depend on the wetting of the surface by the conductive ink, substrate temperature and substrate surface energy. Optimization of the inkjet printing process means to synchronize the ink properties, ink-substrate interaction and the printer

capabilities. With static advancing contact angle measurements the surface energy of the used substrates was evaluated with a Krüss DSA100 contact angle meter by using deionized water (DI H_2O). In general the contact angle of a liquid droplet is defined as the angle between the liquid/vapour interface and the solid surface and is determined by Young's equation. The corresponding contact angles will be presented in Table 6.1 and are a measure for the hydrophilicity.

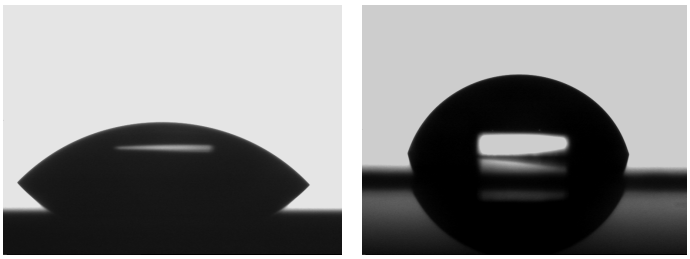

Figure 6.1: DI H_2O droplet on n^{++}-Si/SiO_2 (left) and Teonex® substrate (right).

The optimization process of inkjet-printing included surface treatments such as HMDS (hexamethyldisilazane) application on the n^{++}-Si/SiO_2 substrates to reduce the surface energy by replacing hydroxyl groups on the SiO_2 surface by polar methyl groups.[93] Another surface modifaction method especially applied for the flexible films constitutes plasma activation. By exposing the films to oxygen plasma for different partial pressures and durations, a hydrophilic surface is obtained. Besides surface treatments, studies of temperature variation (40°C, 60°C, 90°C, 120°C) of the substrate during printing were done.

First reasonable results for inkjet-printed silver S/D electrodes on n^{++}-Si/SiO_2 substrate were obtained by printing with a resolution of 800 dpi and a substrate temperature of 120°C. After printing, the ink was sintered at 200°C for 30 min, yielding conductive silver S/D electrodes with channel lengths depicted in Table 6.1. The corresponding silver S/D electrodes are depicted in Figure 6.2. These structured substrates were further used for BG/BC OFETs based on rr-P3HT. The thickness of the electrodes was measured with a profilometer (DekTak) and was determined to ~ 800 nm (see Figure 6.3). This is rather high in comparison to the 50 nm evaporated Au electrode, structured with photolithography. Hence the printing resolution was reduced to 400 dpi, leading to smaller thickness of the electrodes (d ~ 300 nm), but due to the restricted resolution also larger channel lengths L were obtained (seeTable 6.1). Both devices exhibit a very rough surface, which also have to be considered for applications in OFETs, possibly leading to a point effect, enhancing the charge carrier injection. Moreover a reduction of the substrate temperature during printing to 90°C led to smoother electrode surfaces.

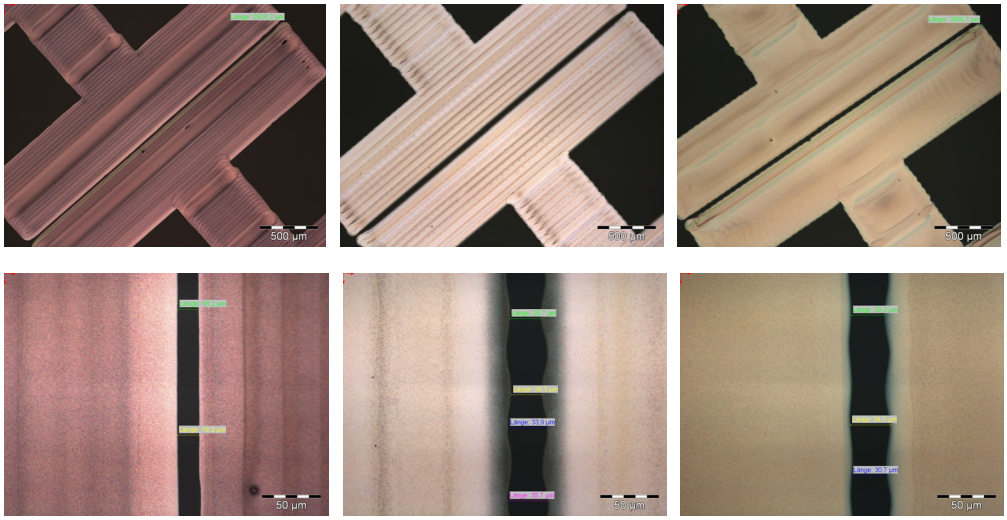

Figure 6.2: Inkjet-printed silver source/drain electrodes printed with 800 dpi (left) and 400dpi (middle) at 120°C substrate temperature and 400 dpi at 90°C substrate temperature on $n^{++}Si/SiO_2$.

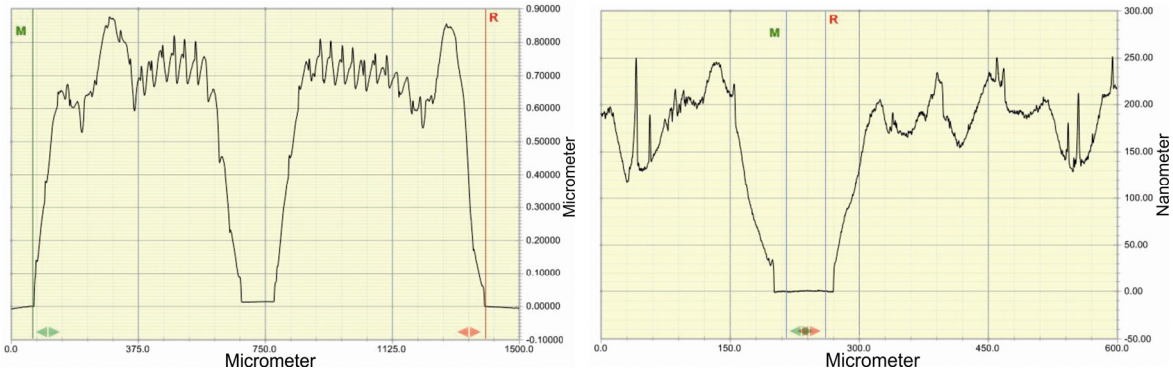

Figure 6.3: Height profiles of the inkjet-printed silver source/drain electrodes with 800 dpi (left) and 400 dpi (right) at a substrate temperature of 120°C on $n^{++}Si/SiO_2$.

Table 6.1: Printing and substrate parameter, including contact angle, obtained with sessile drop method with Krüss DSA100 contact angle meter and achieved S/D dimensions for different substrates.

	Contact angle [°]	Substrate Temperature [°C]	Resolution [dpi]	Channel length L [µm]	Channel width W [mm]
IP7	50	120	800	~20, ~46, ~70, ~107	2.92
IP14	50	90	400	~30, ~95, ~160	3.11
Kap3	69	120	800	~55, ~90, ~120, ~150	2.92
Myl1	77	120	800	~50, ~80, ~120, ~150	2.87
Teo2	74	60	400	~60, ~90, ~150,	3.09

In contrast, flexible films exhibit rather low surface energies obvious in their large contact angles (see Table 6.1), thus the optimization of the inkjet-printing was challenging. Printing with a resolution of 400 dpi on Kapton® and Mylar® was not possible because printed pots were not connected to a layer, which is depicted in Figure 6.4.

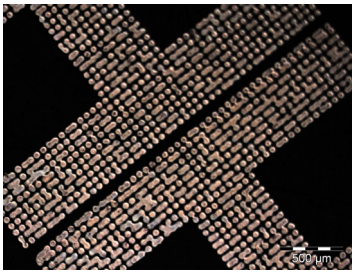

Figure 6.4: Example of non-optimized inkjet-printing of S/D electrodes on Mylar® by using a printing resolution of 400dpi; nonuniform layer obtained.

For Mylar® and Kapton® films S/D electrodes were printed with 800 dpi at 120°C substrate temperature, obtaining a uniform silver layer with dimensions depicted in Table 6.1. Figure 6.5 shows that the inkjet-printed S/D electrodes had a rough surface and in turn exhibited large thicknesses, which resulted in other problems for applications in TG OFETs discussed later.

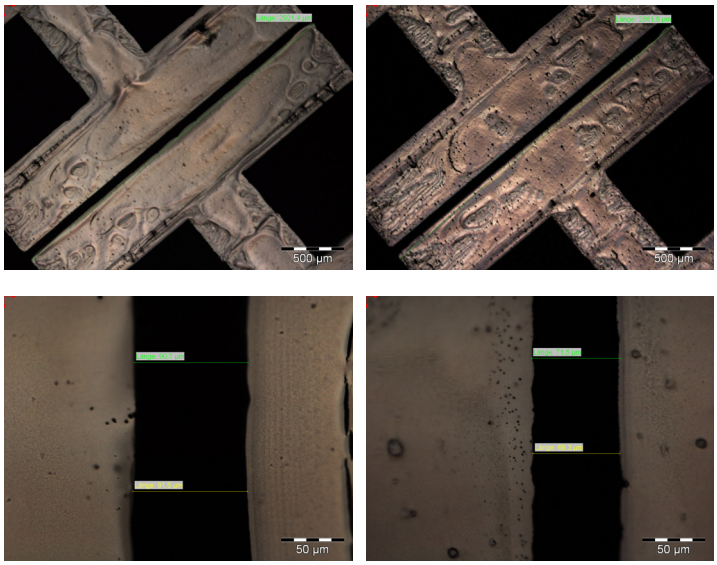

Figure 6.5: Inkjet-printed Ag source/drain electrodes printed with 800 dpi at 120°C substrate temperature on Kapton® (left) and Mylar® (middle) films.

The obtained thick and rough S/D electrodes induced further investigations of the surface of Kapton® and Mylar® films by AFM. Figure 6.6 shows topographic and amplitude error images, where buckles with heights of up to 1.3 µm for Mylar® and 800 nm for Kapton® films within the 80 µm x 80 µm image can be observed. Regarding scratches fewer were observed for the Kapton® films. The RMS-roughness in a 5 µm x 5 µm image was ~ 4 nm for Mylar® and ~1nm for

Kapton® films. Nevertheless the roughness for larger areas of these films and the corresponding problems discussed below led to further attempts to improve the inkjet printing process on PEN films, such as Teonex®, exhibiting very smooth surfaces and temperature stability during heating processes.[94]

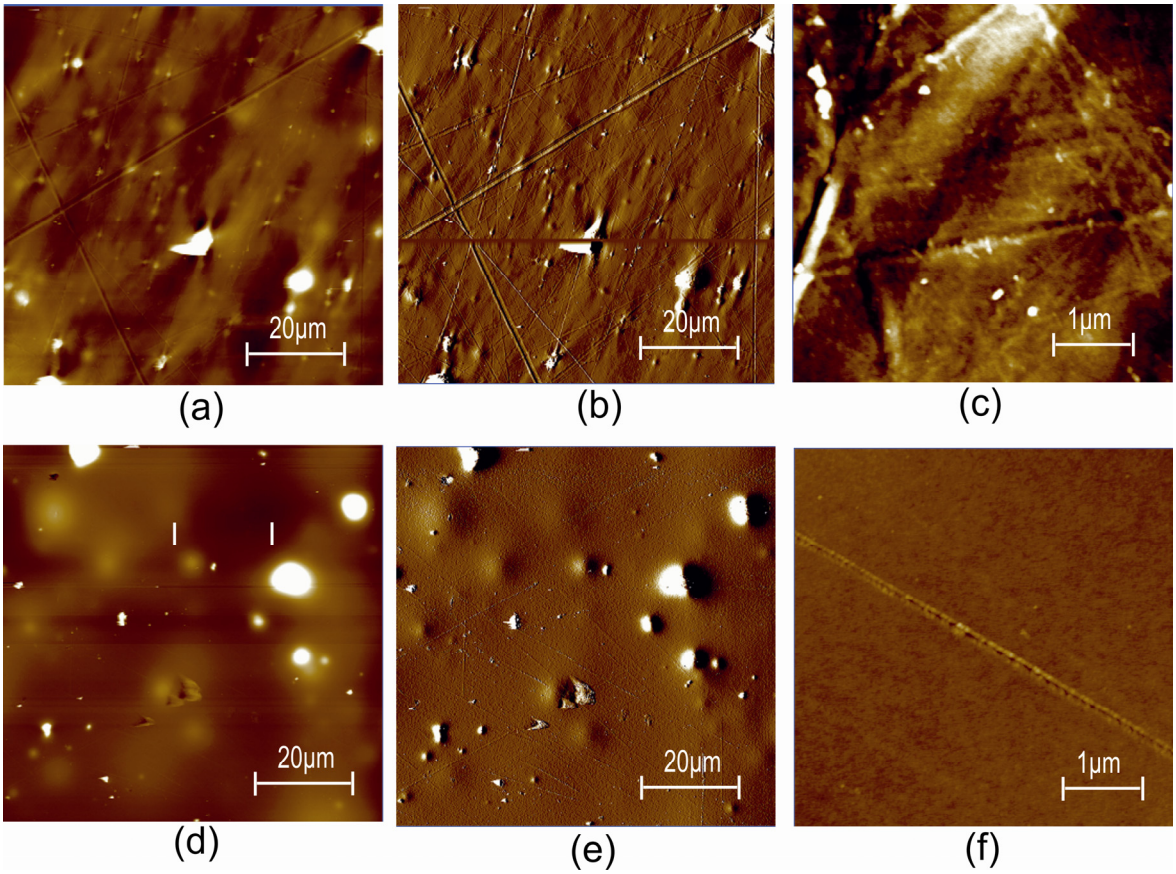

Figure 6.6: AFM-height images of Mylar® films (top: a, c) and Kapton® (bottom: d, f) and corresponding amplitude error images (b, e); scan sizes: 80 µm (left and middle) and 5 µm (right); color code from black to white corresponds to a z-data range of 500nm, 150mV and 25nm, respectively.

Moreover, in order to reduce the electrode thickness on PEN films the printing resolution was decreased to 400 dpi and the corresponding ink was diluted to 25% with ethanol. For dilutions of about 50% silver NP ink and ethanol, very strongly changed behavior of the ink was observed and reasonable inkjet-printing was not possible. In Figure 6.5 (right) the S/D electrodes printed at 60°C substrate temperature at 400 dpi are shown. To obtain such well-structured S/D electrodes, the voltage applied to the piezoelectric unit was also adapted.[j] The surface of the electrodes is smoother but still exhibits a thickness of 600 nm (Figure 6.8).

[j] The adaption of voltage applied to the piezoelectric unit corresponds to a volume change of the ejected drop.

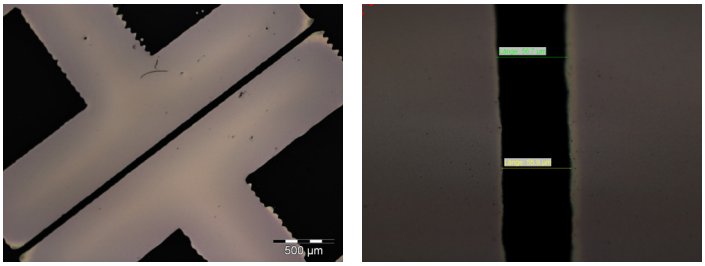

Figure 6.7: Inkjet-printed Ag source/drain electrodes printed with 400 dpi at 60°C surface temperature on Teonex® film.

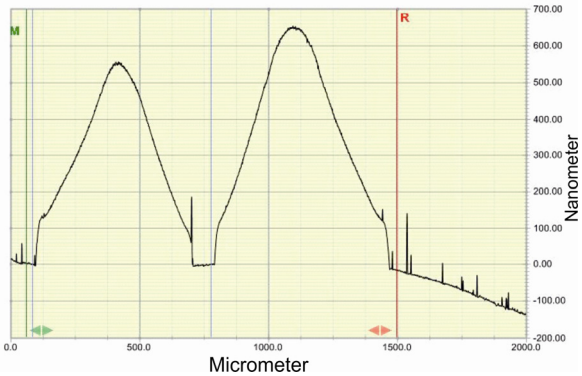

Figure 6.8: Height profile of the inkjet-printed silver source/drain electrodes (400dpi, substrate temperature: 60°C) on Teonex® films.

Figure 6.9 shows various substrates with structured silver source/drain electrodes, which were further used for BG/BC and TG/BC OFETs.

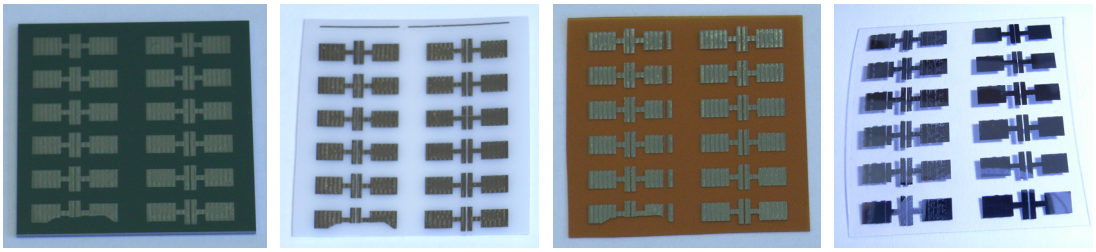

Figure 6.9: From left to right: 12 inkjet-printed silver source/drain electrodes on $n^{++}Si/SiO_2$, Mylar®, Kapton® and Teonex®; one device is not fully printed due to fixation of the substrate during printing; for the left devices on Kapton® certain lines were not printed due to nozzle clogging.

6.2 Comparison of BG/BC OFETs with Evaporated Gold S/D Electrodes with BG/BC OFETs based on Silver Inkjet-Printed S/D Electrodes

To investigate the first results of inkjet-printed silver (Ag) S/D electrodes, rr-P3HT based BG/BC OFETs were fabricated on n^{++}-Si/SiO_2 and compared in detail with devices based on evaporated chromium/gold (Cr/Au) S/D electrodes. For this comparison a typical sample (IP7) with inkjet-printed S/D electrodes (800 dpi) was used, exhibiting channel lengths of L ~ 20 µm, ~ 46 µm, ~ 70 µm and ~ 107 µm (see Table 6.1). The Au S/D electrodes for the reference sample (KSC7) were photolithographcally structured (see chapter 2.1.1), yielding channel dimensions of L ~ 2.5 µm, ~ 10 µm, ~ 25 µm ~ 50 µm and W ~ 2.85 mm. In the following, devices with ~ 50 µm channel lengths will be compared. After evaluation of the devices with the optical microscope both samples were transferred into the glove box to perform a dehydration bake. No additional cleaning step was applied after inkjet-printing. The following device fabrication of BG/BC OFETs is already described in chapter 2.3, including spin-casting (1500 rpm, 40 s) of rr-P3HT solution (2mg/ml in $CHCl_3$) and dehydration bake at 120°C for 1h in high vacuum. Figure 6.10 depicts a typical OFET with inkjet-printed Ag S/D electrodes (left) and a device with Au S/D electrodes (right).

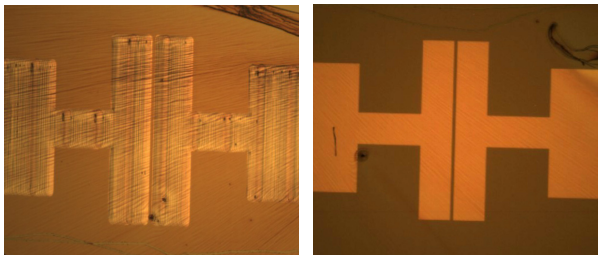

Figure 6.10: Typical BG/BC OFETs with silver inkjet-printed S/D electrodes (left) and with evaporated Au S/D electrodes (right).

The electrical characterization was carried out under inert conditions. Figure 6.11 shows the transfer and output characteristics of a typical rr-P3HT-based OFET with inkjet-printed S/D electrodes (IP7, left) in comparison with a device based on Au electrodes (KSC7, right). Basically, both OFETs revealed similar device performance in terms of on-current, off-current, and mobility. However, the slightly larger maximum channel current I_D in the transfer characteristics of the OFET with inkjet-printed S/D electrodes can be ascribed to the larger channel width and slightly smaller channel length. As shown in Figure 6.2, the obtained channels of OFETs based on inkjet-printed processes did not exhibit as smooth and accurate channel structures as photolithographically structured devices. Compared to the transfer curves, the I_D values in the output characteristics are smaller at the same working point, which is ascribed to charger carrier trapping. Here high negative gate voltages have more time to affect the channel. Moreover, the observed hysteresis, where the drain current is decreasing for the reverse sweep, can also be

ascribed to charge carrier trapping. This hysteresis is more pronounced for OFETs with inkjet-printed S/D electrodes, which can possibly be explained by a less clean surface due to handling of the devices in air during inkjet-printing, resulting in more traps at the semiconductor/dielectric interface.

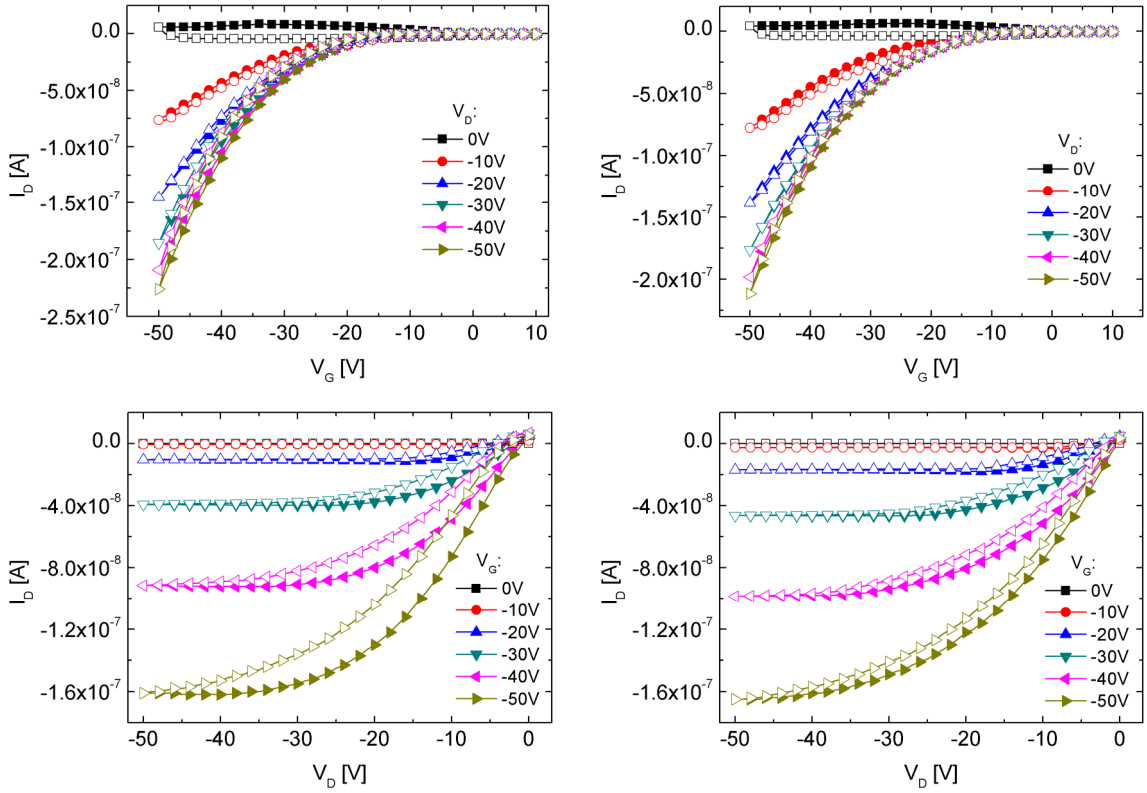

Figure 6.11: Transfer (top) and output (bottom) characteristics of rr-P3HT based OFETs; left: device with inkjet-printed Ag S/D electrodes (sample IP7; L ~ ~46 µm, W ~ 2.92 mm); right: device with evaporated Au S/D electrodes (sample KSC7; L ~ ~50 µm, W ~ 2.85 mm); closed symbols: forward sweep; open symbols: reverse sweep.

The higher trap density of the inkjet-printed OFET is also reflected in the calculated device parameters, such as switch-on voltage V_{so} and threshold voltage V_{th} (see Table 6.2). Since different materials (Ag/Au) are used for the S/D electrodes, a difference in charge injection would be expected due to the different work functions of the metals (Φ_{Ag}=4.3 eV, Φ_{Au}=5.1 eV). However, for this device series the difference of the surface roughness of the two types of electrodes is more dominant. Figure 6.3 shows the rough surface, exhibiting several peaks, where point effect can may enhance the charge carrier injection.

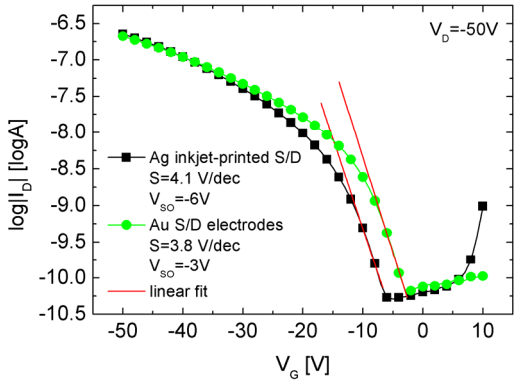

Figure 6.12: Semilogarithmic transfer curves of device with OFET based on inkjet-printed Ag S/D electrodes (black squares) and OFETs with Au S/D electrodes (green circles), including fits to determine the subthreshold slope.

The on/off-current ratios, field-effect mobilities and subthreshold slopes were in the same range for both devices (see Table 6.2.). Figure 6.13 depicts the field-effect mobility for the linear regime (left) and the saturation regime (right) for devices of each channel length of a sample with inkjet-printed S/D electrodes, exhibiting qualitatively similar behavior for all channel lengths. The field-effect mobilities of the linear regime exhibit higher values at high gate voltages for devices with larger channel lengths, which is ascribed to the neglection of the contact resistance R_p in eq. (1.7) and eq.(1.8). In shorter channels the influence of R_p is larger an therefore seemingly lower the μ_{FE} values are obtained in such devices when applying in eq. (1.7) and eq.(1.8) for the determination of the field-effect mobility.

Table 6.2: Comparison of device parameters of a typical OFET with silver inkjet-printed S/D electrodes (L~46µm, W~2.97mm) with OFETs based on Cr/Au S/D electrodes (L~50µm, W~2.85mm); V_{so}, V_{th}, and S were extracted from the transfer curves at V_D= - 50 V; μ_{lin} and μ_{sat} were calculated with equation (1.7) and (1.8).

Parameter	Ag-S/D electrodes (sample IP7)	Cr/Au-S/D electrodes (sample KSC7)
On/off- current ratio	2.5×10^3	2.8×10^3
V_{so} [V]	-6	-3
V_{th} [V]	-14	-8
S [V/dec]	4.1	3.8
μ_{sat} [cm^2/Vs], (V_G=-40V, V_D=-50V)	3.9×10^{-4}	3.1×10^{-4}
μ_{lin} [cm^2/Vs], (V_G=-40V, V_D=-10V)	3.1×10^{-4}	2.9×10^{-4}

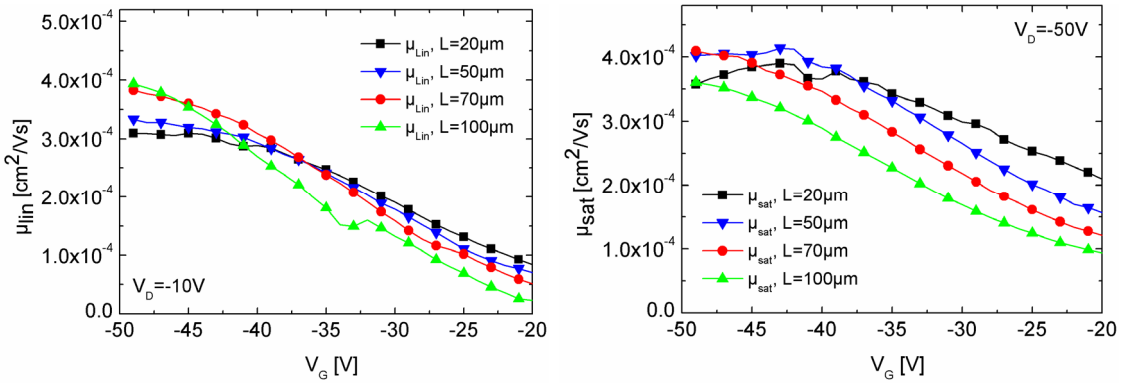

Figure 6.13: Field-effect mobility in the linear (left) and saturation (right) regime of OFET with inkjet-printed S/D electrodes (IP7, W ~ 2.92 mm).

The corresponding field-effect mobilities for such devices with evaporated Au S/D electrodes are depicted in Figure 6.14, showing also the channel length dependence, where lower mobility values for OFETs with smaller channel lengths are obtained due to the increasing influence of the contact resistance with decreasing channel length. The fact that in the saturation regime the device with the shortest channel length (L = 2.5 μm) exhibited the largest mobility, can be ascribed to short channel effects, where the gradual channel approximation is no longer valid.[29] Moreover, for increasing negative gate voltages, saturation of the mobility is observed, which can be ascribed to the fact that charge carriers are attracted to the semiconductor/dielectric interface, where the trap density is high (mobility degradation).

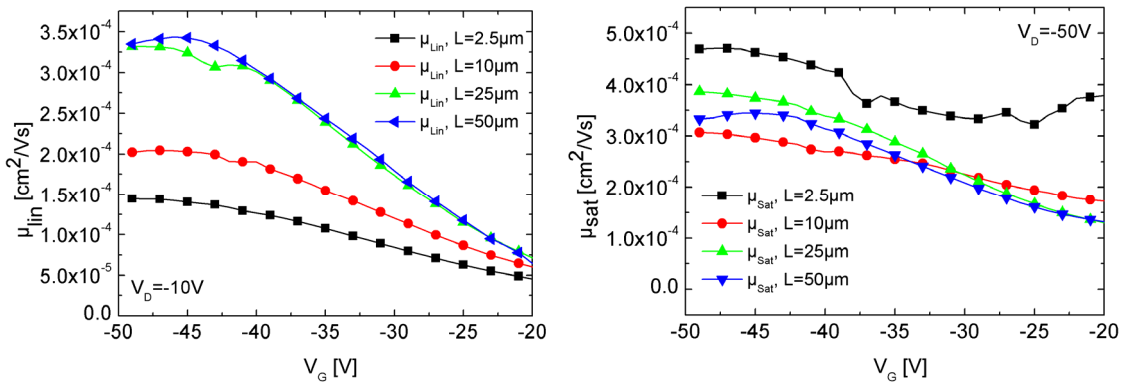

Figure 6.14: Field-effect mobilityin the linear (left) and saturation (right) regime of OFET with evaporated Cr/Au S/D electrodes (KSC7, W ~ 2.85 mm).

Figure 6.15 depicts the transfer curves of devices based on inkjet-printed Ag S/D electrodes and on Au S/D electrodes with varying channel lengths on linear and semilogarithmic scale. For short channels both devices show a significant increase in on-current and the switch-on voltage is slightly shifted to more positive direction, which is more pronounced for the devices with Au S/D electrodes. This shift can be ascribed to short channel effects, where the channel currents enter the

space charge limited current (SCLC) regime.[25] Moreover the higher channel currents are accompanied by a slightly larger hysteresis.

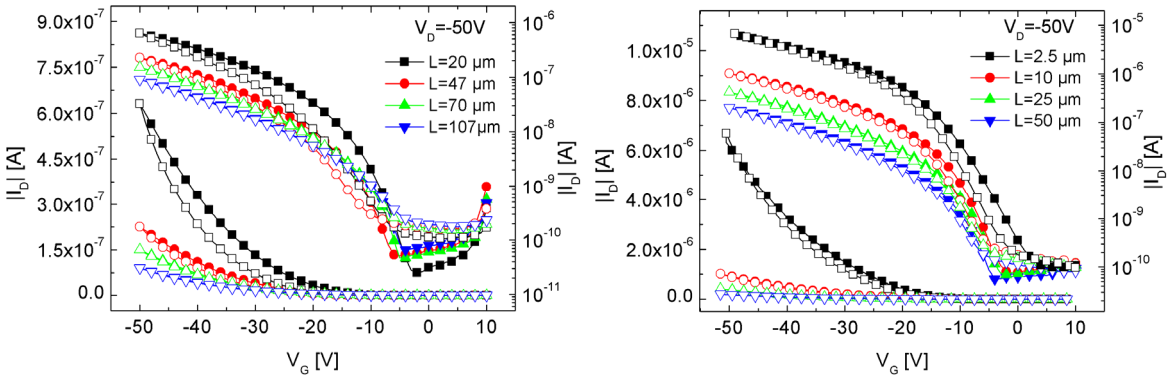

Figure 6.15: Transfer curves (linear and semi-logarithmic) at V_D = -50V of OFETs based on inkjet-printed S/D electrodes (left) and evaporated Cr/Au electrodes with varying channel lengths L; closed symbols: forward sweep; open symbols: reverse sweep.

6.2.1 TLM – Transfer Line Method

In order to investigate the influence of contact resistance the transfer line method (TLM) was applied. With this method the separate extraction of the parasitic contact resistance R_p and channel resistance R_{ch} is possible. The device resistance R_{on} is determined by the sum of R_p and R_{ch}. The channel resistance is assumed to be linearly dependent on the channel length L, whereas the contact resistance is independent of L. Figure 6.16 shows the device resistance $R_{on}W$ $(= V_D \cdot W/I_D)$ as a function of the channel length for devices with evaporated Au S/D electrodes. The corresponding extrapolated linear fits cross at $L_0 \sim 2.3$ µm and $(R_pW)_0 \sim 1.7\text{x}10^6$ Ωcm (Figure 6.16, right), being in accordance with values shown within the thesis of Arno Meingast.[95] L_0 is regarded as the length of an additional transition layer between gold and the semiconductor and $(R_pW)_0$ is the gate-voltage independent part of the contact resistance, corresponding to the injection barrier formed by the organic semiconductor and electrode. R_p W, which is the sum of the gate voltage independent part $(R_pW)_0$ and the gate voltage dependent part the contact resistance. It is obtained at the intersection of the linear fits at zero channel length and is plotted in Figure 6.17 as a function of gate voltage. It shows that the parasitic contact resistance is decreasing with increasing gate voltage because of the fact that charge carriers are more easily injected as the gate voltage is increased.

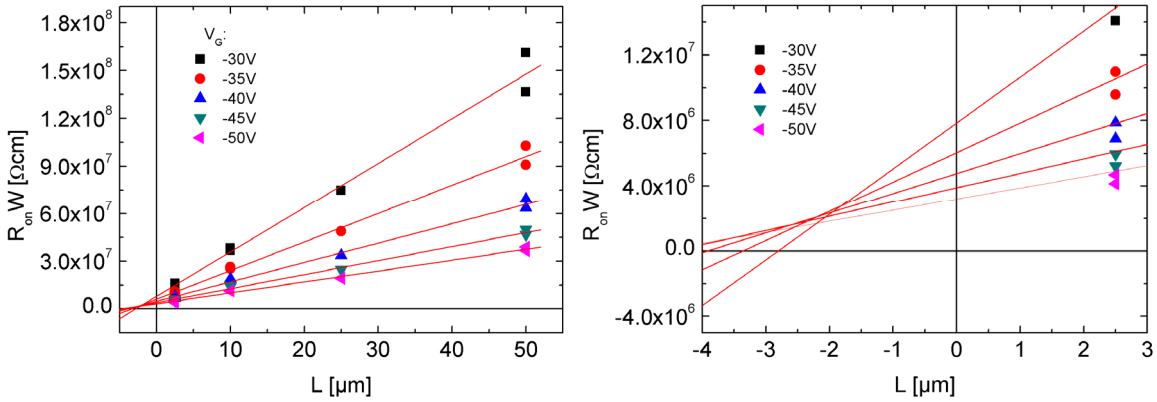

Figure 6.16: Plot of width-normalized device resistance R_{on} as a function of channel length L for OFETs with Au S/D electrodes (left) and zoomed section (right).

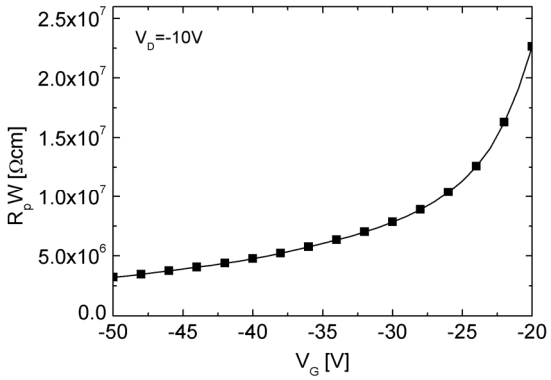

Figure 6.17: Width-normalized parasitic contact resistance R_p as a function of gate voltage V_G.

The TLM was also performed for rr-P3HT based OFETs with inkjet-printed Ag S/D electrodes, where a physically meaningless negative contact resistance was obtained which however indicates that the contact resistance is rather small. This can probably be explained by the very rough surface of the inkjet-printed S/D electrodes, leading to very high electric field strengths (point effect). Moreover the shortest channel length for these samples is ~20 µm and the channels are not as accurate as for photolithographically structured devices, resulting in a larger error. Therefore the results of the TLM for devices with inkjet-printed S/D electrodes are not shown.

6.3 Low Voltage TG/BC OFETs based on rr-P3HT with Inkjet-Printed Silver S/D Electrodes

Aside from BG OFETs, also TG OFETs with inkjet-printed silver S/D electrodes with PVA as gate dielectric were fabricated. In this chapter the results of rr-P3HT based TG/BC OFETs on a typical substrate IP14 (see chapter 6.1) will be presented. The Ag S/D electrodes were printed with a resolution of 400 dpi at 90°C (see Table 6.1), yielding channel length between ~30 µm and ~160 µm and an electrode thickness of ~300 nm. The corresponding fabrication steps, including the deposition of the organic semiconductor (rr-P3HT, 2mg/ml toluene) and of PVA are already described in chapter 2.3. The PVA film was spin-cast (~ 1500 rpm, 60 s) from dialysed hydrogel (Mowiol 4-98, 8.3°wt%, $d_i \approx 800$ nm) and dried in high vacuum at 120°C overnight. Afterwards 100 nm thick silver top-gate meander-shaped electrodes were evaporated through a shadow mask. Figure 6.18 illustrates a typical device on n^{++}-Si/SiO_2 and the complete sample exhibiting 12 devices. The corresponding dielectric characterization of Mowiol 4-98 ($\varepsilon_r \sim 9$) was described in chapter 5.2.

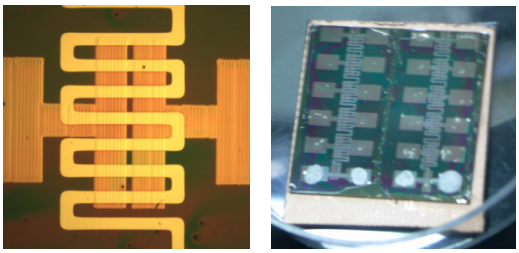

Figure 6.18: TG/BC OFET based on rr-P3HT and PVA with inkjet-printed silver source/drain electrodes (thickness: ~ 300 nm, 400 dpi) on n^{++}Si/SiO_2 (L ~ 95 µm, W ~ 3 mm) (left) and complete sample (right).

Figure 6.19 shows the transfer characteristics of such an OFET (L ~30 µm, W ~ 3 mm), exhibiting reasonable performance and low-voltage operation. The high off-currents (I_D at $V_G = 0$ V) and consequently low on-/off-current ratios can be ascribed to the rather thick and rough source/drain-electrode structures and to ions within PVA. Similar as in chapter 5, where PVA was used as an intermediate layer for TG OFETs the source-to-drain channel current was larger in the reverse sweep of each transfer curve, being a sign for the presence of mobile ions within PVA. Therefore the existence of a positive switch-on voltage values can be attributed to the mobile ions due to reasons above mentioned. The corresponding maximum gate leakage current of the device shown is about 10 nA, whereas other devices on the sample exhibited larger leakage currents due to the very thick and rough electrodes. However these results were rather promising on the way to all solution processed OFETs.

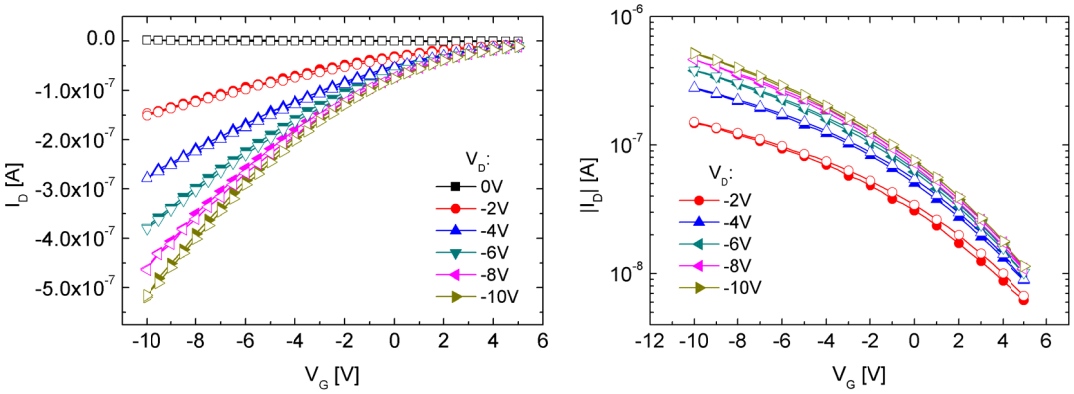

Figure 6.19: Transfer characteristics of a typical TG OFET (IP14) with inkjet-printed SD electrodes (L ~ 30 µm, W ~ 3 mm) (left) and corresponding semilogarithmic transfer curves (right); closed symbols: forward sweep; open symbols: reverse sweep.

6.4 Flexible TG/BC OFETs based on rr-P3HT with Inkjet-Printed Silver S/D Electrodes

Based on the results above flexible TG/BC OFETs based on rr-P3HT with inkjet-printed silver S/D electrodes were fabricated and thoroughly investigated. For these experiments Mylar® (Myl1), Kapton® (Kap3) and Teonex® (Teo2) were used as substrates. The following device fabrication was similar to the one for TG/BC OFETs on n^{++}-Si/SiO_2 (see chapter 6.4). Figure 6.20 shows the completed samples on various substrates.

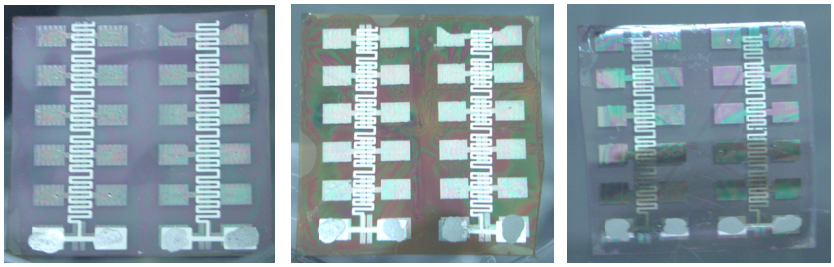

Figure 6.20: TG/BC OFETs based on rr-P3HT and PVA with inkjet-printed silver source/drain electrodes on Mylar® (Myl4), Kapton® (Kap3) (thickness: ~ 800 nm, 800 dpi) and Teonex® (Teo2) (thickness:~ 600 nm, 400 dpi).

The devices on these substrates were not functioning properly. Most of them were shorted between the TG and the S/D contacts. The inkjet-printed S/D electrodes on Mylar® and Kapton® had a thickness ~800 nm, being too high and leading to shorts across the ~800 nm thick PVA layer. Due to the rather thick electrodes, probably also not much organic semiconductor material was within the channel. Moreover, the AFM investigations (see Figure 6.6) of the surface of the substrates revealed very rough surfaces, which are also not desired in OFET applications. Therefore a Teonex® film was applied, where the S/D electrodes were printed with a reduced resolution of 400 dpi compared to the S/D electrodes for Mylar® and Kapton®. The profilometer measurements

showed that the obtained electrodes were much smoother, exhibiting a thickness of 600 nm high (see Figure 6.8). The investigation of OFETs based on these substrates yielded again shorts across the gate dielectric.

In order to avoid them a thicker PVA layer was applied. As substrate also a Mylar® film with inkjet-printed S/D electrodes (thickness ~ 800 nm, 800 dpi) was used. To ensure that the organic semiconductor is thick enough to enable field-effect behavior a 5 mg/ml rr-P3HT solution (toluene) was prepared and spin-cast. The fabrication process is similar to the one depicted above, except that the solid content of the PVA solution (Mowiol 4-98) was increased from 8 wt% to 15 wt% by evaporation of water. The PVA film was spin-cast (1500 rpm, 60 s) from dialysed hydrogel (15 wt%) and dried in high vacuum at 100°C for 3 h. Afterwards 100 nm thick silver top-gate meander-shaped electrodes were evaporated through a shadow mask.

The electrical characterization showed that the application of a thicker PVA and rr-P3HT layer led to functioning devices. Figure 6.21 depicts the transfer characteristics of such a device with channel length L ~ 50 µm and W ~ 2.87 mm, showing still a rather low performance in terms of high off-currents and consequently very low on/off-current ratios. It most probably originates on the one hand from the thicker rr-P3HT layer, leading to a higher bulk current, and on the other hand from the formation of EDLs and/or electrochemical doping at the semiconductor/dielectric interface due to residual ions within PVA, which is also more pronounced because of the thicker PVA layer.

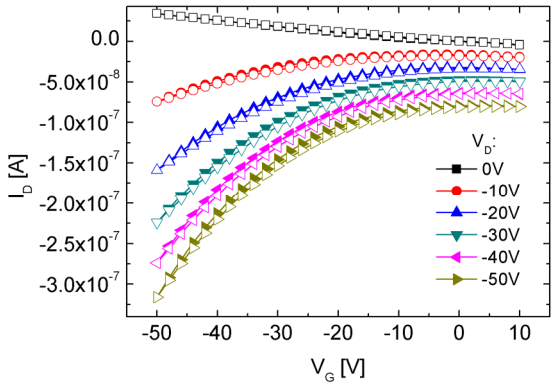

Figure 6.21: Transfer characteristics of a typical flexible TG OFET with inkjet-printed SD electrodes on Mylar® (L ~ 50 µm, W ~ 2.87 mm); closed symbols: forward sweep; open symbols: reverse sweep.

6.4.1 Operational Stability and Ionic Drifts

In order to investigate the operational stability and the drifts of the channel currents of flexible OFETs with inkjet-printed S/D electrodes, bias stress measurement at a certain working point (V_D = -40 V, V_G = -30 V) were performed as a function of time. A distinct increase of the channel current upon bias stress was observed, being ascribed to mobile ions in the polymer gate dielectric. This result supports the findings concerning investigations of effects of mobile ions presented in chapter 5.

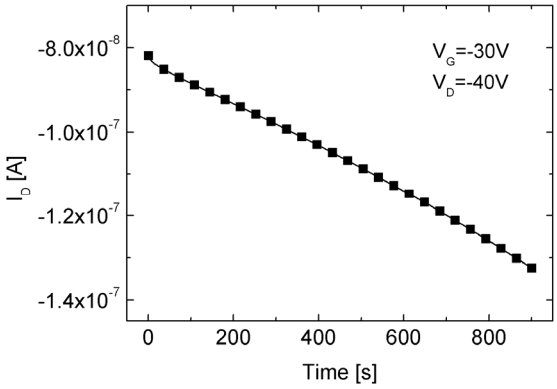

Figure 6.22: Source-to-drain channel current I_D at fixed gate and drain voltages as a function of time of a typical device on Mylar® (L ~ 50 µm, W ~ 2.85 mm).

6.4.2 Flexibility Tests

Furthermore, the device performance of flexible OFETs was also investigated before, during and after bending the sample. Figure 6.23 illustrates the sample in planar and bent state contacted with probe needles on the probe station under inert atmosphere.

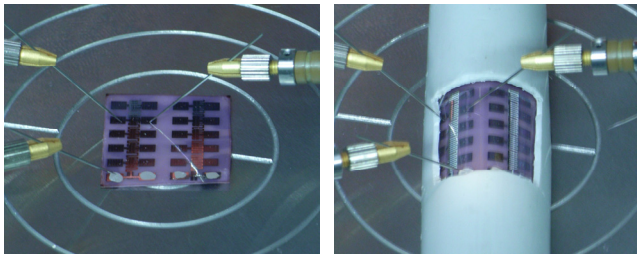

Figure 6.23: Sample picture in planar and bent state with one device under test.

The devices were also functioning in the bent state and after bending, showing only slight change in the corresponding transfer curves (see Figure 6.24). The small increase of on-current for the planar state measurement after bending can be ascribed to bias stress, since several measurements were started before this transfer curve was recorded.

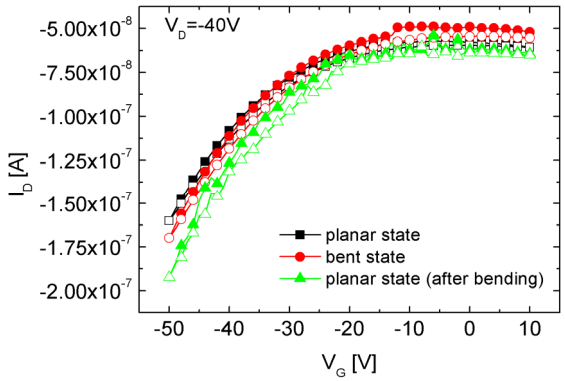

Figure 6.24: Transfer curves at V_D = -40 V measured in planar state, bent state and after bending (L ~ 50 µm, W ~ 2.87 mm); closed symbols: forward sweep; open symbols: reverse sweep.

6.5 Summary and Conclusions

Inkjet-printing with a silver nanoparticle ink was successfully implemented for structuring source/drain electrodes on a variety of substrates, including n^{++}-Si/SiO_2, Mylar®, Kapton® and Teonex® (see Figure 6.2, Figure 6.5 and Table 6.1). BG OFETs based on rr-P3HT with Ag inkjet-printed S/D electrodes (400 dpi, substrate temperature: 90°C) showed similar device performance as devices based on evaporated Cr/Au S/D electrodes, regarding device parameters such as on-current, field-effect mobility ($\mu_{lin} \sim 3x10^4$ cm^2/Vs at V_G = -40 V) and on/off-current ratio. Moreover, first promising results were obtained with TG/BC OFETs including inkjet-printed Ag S/D electrodes on n^{++}-Si/SiO_2 operating at low voltage regimes up to 10 V. Besides being realized on rigid substrates, TG OFETs with inkjet-printed S/D electrodes were also fabricated on flexible substrates such as Mylar® films, which yielded first functioning devices also during bending the sample. In addition, source-to-drain channel current drifts were also investigated for this flexible TG/BC OFET, showing a distinct increase of channel current with time, which was ascribed to mobile ions in the applied gate dielectric. Although the presented devices leave room for improvement, the results showed first promising results on the way to all solution processed inkjet-printed OFETs.

7 Summary and Conclusions

Aside from other target applications, organic field-effect transistors (OFETs) offer a great deal of promise as sensor elements, since organic compounds can be tailored, enhancing the sensitivity and selectivity with respect to an analyte, and are furthermore solution processable, which enables the fabrication of low-cost smart (disposable) sensor tags. In this work the main focus was set on the investigation of OFETs as transducers for ions.

At first, however, novel organic semiconductors were evaluated in a bottom-gate/bottom-contact (BG/BC) OFET architecture on n^{++}-Si/SiO_2 substrates. It was found that OFETs based on novel conjugated polymers with carbazole units and dendrimers PYGCAP and PYGTPA are not very appropriate for applications in OFETs (chemical structures shown in Figure 3.1 and Figure 3.5), since only dendrimer PYGTPA revealed a distinct field-effect, but with a rather low device performance (see Figure 3.7), which is most likely ascribed to an improper or even non-existing alignment of the material.

In order to evaluate a new sensor concept for ion sensing based on a top-gate architecture with an ion-sensitive dielectric, at first BG/BC OFETs including deliberately added ions within regioregular poly(3-hexylthiophene) (rr-P3HT) were fabricated. In detail, rr-P3HT was blended with dibenzo-18-crown-6 (DCH18C6) as ion conductor and sodium trifluoromethanesulfonate (CF_3SO_3Na) as salt. Basically, it was found that OFETs based on such a rr-P3HT-CF_3SO_3Na-DCH18C6 blend show similar device performance as reference devices based on rr-P3HT solely, regarding device parameters like on-current, field-effect mobility and on/off-current ratio (see Figure 4.6 and Table 4.1). This was also observed for OFETs based on a rr-P3HT-DCH18C6 blend without added salt (see Figure 4.4). The presence of ions could be clearly approved by several effects, namely larger hysteresis, a more positive switch-on voltage after drain bias stress, a lower subthreshold slope and an increase of the source-to-drain channel current with time. These effects are mainly ascribed to the formation of electric double layers at the semiconductor/electrode interface and/or electrochemical doping, resulting in lower injection and ejection barriers and thus a reduction of the corresponding contact resistances. Moreover, it was found that the ion-containing OFETs exhibit a larger trap density due to a phase separation between rr-P3HT, sodium triflate and DCH18C6, resulting in more negative switch-on voltages compared to the reference devices. Furthermore experiments were performed, where the function of the source and drain electrodes were exchanged by switching the source/drain voltages, which led to a significant decrease of the source-to-drain channel current, followed by a slow I_D increase, being also ascribed to the redistribution of ions within the organic semiconducting layer (see Figure 4.16).

Based on these results the influence of ions was also thoroughly studied within the dielectric layer, when polymer electrolyte dielectrics including polyvinyl alcohol and a novel norbornene-based polymer functionalized with dibenzo-18-crown-6 (DCH18C6) as well as its reference polymer were applied in top-gate/bottom-contact (TG/BC) OFETs (chemical structures in Figure 5.1). Capacitors based on these novel dielectric materials and on various polyvinyl alcohol grades (PVA) (Mowiol 5-88, 4-98 and 6-98) revealed a stable operation upon DC bias application (for obtained relative permittivity see Table 5.1). rr-P3HT based TG/BC OFETs with deliberately added ions within the functionalized DCH18C6-based polymer exhibited significant larger on-currents up to 800% in comparison to devices based on the DCH18C6-polymer solely and devices based on the reference polymer (see Figure 5.13), which can be clearly ascribed to ions, leading to the formation of electric double layers (EDLs) at the various interfaces and/or to electrochemical doping. Moreover, various bias stress measurements yielded significant source-to-drain channel current drifts for OFETs with deliberately added ions within the dielectric layer, which was also observed but less pronounced for the reference devices. After these bias stress measurements again a shift to more positive switch-on voltages was more pronounced for the device based on DCH18C6-polymer with ions, being ascribed to ionic effects (see Figure 5.18). Consequently, after studying the effects of ions within the gate dielectric, first experiments, where an ion-containing solution was drop-cast onto the dielectric in a capacitor structure, demonstrated that the top electrodes and the dielectric layer are affected by the solution, in particular when a DC bias is applied (see Figure 5.28). Moreover, the influence of the highly n-doped Si as substrate regarding a possible dual gate operation was investigated (see Figure 5.22).

As first steps on the way to an all-solution processed inkjet-printed low voltage OFET sensor device, inkjet-printing with a silver nanoparticle ink was successfully implemented as a low-cost fabrication technique for structuring source/drain electrodes on a variety of substrates, including n^{++}-Si/SiO_2, Mylar®, Kapton® and Teonex® (see Figure 6.2, Figure 6.5 and Table 6.1). Accordingly, BG OFETs based on rr-P3HT with Ag inkjet-printed S/D electrodes showed similar device performance as devices based on evaporated Cr/Au S/D electrodes, regarding device parameters such as on-current, field-effect mobility and on/off-current ratio. Moreover, first promising results were obtained with rr-P3HT based TG/BC OFETs including PVA and inkjet-printed Ag S/D electrodes on n^{++}-Si/SiO_2, operating at low voltages up to 10 V (see Figure 6.19). Besides being realized on rigid substrates, TG OFETs with inkjet-printed S/D electrodes were also fabricated on flexible substrates such as Mylar® films, which yielded first functioning devices also during bending the sample (Figure 6.24). In addition, source-to-drain channel current drifts were also investigated for these flexible TG/BC OFETs, showing a distinct increase of the channel current with time due to mobile ions within the gate dielectric, being in accordance with the results shown in chapter 5.

To sum up, although the presented devices leave room for improvement, the results of this work have clearly demonstrated the effects of ions and the corresponding underlying mechanisms found in organic field-effect transistors, emphasizing the immense potential of OFETs as sensing elements for ion detection.

Bibliography

[1] F. Bettelheim, W. H. Brown, M. K. Campbell, S. O. Farrell, *Introduction to General, Organic and Biochemistry*, Edition 9, Cengage Learning Services **2009**.

[2] D. R. Gamota, P. Brazis, K. Kalyansundaram, *Printed Organic and Molecular Electronics*, Kuwer Academic Publisher, Massachusetts **2004**.

[3] R. G. Kepler, *Phys. Rev.* **1960**, *119*,1126.

[4] M. Pope, H. Kallman, P. Magnante, *J. Chem. Phys*. **1963**, *38*, 2042.

[5] H. Shirakawa, E. J. Louis, A. MacDiarmid, C. Chiang, A. J. Heeger, *J. Chem. Soc,. Chem. Comm.* **1977**, *16*, 578.

[6] K. Müllen, U. Scherf, *Organic Light Emitting Devices – Synthesis, Properties, and Applications*, Wiley-VCH Weinheim **2006.**

[7] G. Horowitz, *Adv. Mater*. **1998**, *10*, 365.

[8] C. D. Dimitrakopoulos, P. R. L. Malenfant, *Adv. Mater*. **2002**, *14* (2), 99.

[9] P. Matyba, K. Maturova, M. Kemerink, N. D. Robinson, L. Edman, *Nat. Mat.* **2009,** *8*, 672.

[10] S. Günes, H. Neugebauer, N. S. Sariciftci, *Chem. Rev*. **2007**, *107* (4), 1324.

[11] M. Gaal, C. Gadermaier, H. Plank, E. Moderegger, A. Pogantsch, G. Leising, E. J. W. List, *Adv. Mater*. **2003**, *15*(14), 1165.

[12] http://www.ntu.ac.uk/cels/molecular_geometry/hybridization/Sp2_hybridization/index.html

[13] A. Klug, „*Organic field-effect transistors - fundamentals and technological aspects*“, Diploma Thesis, Graz University of Technology **2005**.

[14] http://de.wikibooks.org

[15] Z. Bao, J. Locklin, *Organic Field-Effect Transistors*, CRC Press **2007**.

[16] V. C. Sundar, J. Zaumseil, Podzorov, E. Menard, R. L. Willett, T. Someya, M. E. Gershenson, J. A. Rogers, *Science* **2004**, *303*, 1644.

[17] G. E. Le Comber, W. E. Spear, *Phys. Rev. Lett.* **1970**, *25*, 509.

[18] G. Horowitz, H. E. Hajlaoui, R. Hajlaoui*, J. Appl. Phys*. **2000**, *87*, 4456.

[19] M. C. J. M. Vissenberg, M. Matters, *Phys. Rev. B* **1998**, *57*, 12964.

[20] J. A. Rogers, Z. Bao, K. Baldwin, A. Dodabalopur, B. Crone, V. R. Raju, V. Kuck, H. Katz, K. Amundson, J. Ewing, E. Drzaic, *PNAS* **2001**, *98*, 4835.

[21] G. H. Gelinck, H. Edzer, A. Huitema, E. van Veenendaal, E. Cantatore, L. Schrijnemakers, J. B. van der Putten, T. C. Geuns, M. Beenhakkers, J. B. Giesbers, *Nat. Mater.* **2004**, *3*,106.

[22] F. Eder, H. Klauk, M. Halik, U. Zschieschang, G. Schmid, C. Dehm, *Appl. Phys. Lett*. **2004**, *84*, 2673.

[23] www.polyic.com/en/press-images.php

[24] R. A. Street, A. Salleo, *Appl. Phys. Lett.* **2002**, *81*, 2887.

[25] A. Klug, „ *Organic Field-Effect Transistors – Process Development, Stability Issues and Sensor Applications*“, PhD Thesis, Graz University of Technology **2010**.

[26] G. Horowitz, R. Hajlaoui, H. Bouchriha, R. Bourguiga, M. Hajlaoui, *Adv. Mat.* **1998**, *10*, 923.

[27] M. Shur*, Physics of Semiconductor Devices,* Prentice Hall, Englewood Gliffs, NJ **1990**.

[28] S. M. Sze, *Physics of Semiconductor Devices*, Third Edition, John Wiley and Sons **2007**.

[29] G. Wurzinger, „*Influence of Air, Oxygen Moisture and Water on the Performance of Organic Field-Effect Transistors*“, Diploma Thesis, Graz University of Technology **2009.**

[30] J. Zaumseil, K. W. W. Baldwin, J. A. Rogers, *J. of Appl. Phys.* **2003**, *93* (10), 6117.

[31] J. T. Mabeck, G. G. Malliaras, *Anal. Bioanal. Chem.* **2006**, *384*, 343 and references therein.

[32] C. Bartic, G. Borgh, *Anal. Bioanal. Chem*. **2006**, *384*, 354 and references therein.

[33] L. Torsi, A. Dodabalapur, L. Sabbatini, P. G. Zambonin, *Sens. Actuators B* **2000**, *67*, 312.

[34] W. Hu, Y. Lui, Y. Xu, S. Liu, S. Zhou, D. Zhu, B. Xu, C. Bai, C. Wang, *Thin Solid Films* **2000**, *360*, 256.

[35] B. Crone, A. Dodabalapur,, A. Gelperin, L. Torsi, H. E. Katz, A. J. Lovinger, Z. Bao, *Appl. Phys. Lett.* **2001**, *78*(15), 2229.

[36] D. A. Bernards, R. M. Owens, G. G. Malliaras, *Organic Semiconductors in Sensor Applications*, Springer-Verlag Berlin Heidelberg **2008**.

[37] C. Bartic, A. Campitelli, K. Baert, J. Suls, *IEDM Tech. Dig.* **2000**, 411.

[38] P. Bergveld, *Sens. Act. B* **2003**, 88.

[39] J. Janata, *Principles of chemical sensors*, 2nd Edition, Springer, Dortrecht, Heidelberg, London, New York **2009**.

[40] D. Moss, J. Janata, J. J. Johnson, *Anal. Chem.* **1975**, *47* (13), 2238.

[41] C. Bartic, A. Campitelli, S. Borghs, *Appl. Phys. Lett.* **2003,** *82*, 3.

[42] A. Loi, I. Manunza, A. Bonfiglio, *Appl. Phys. Lett.* **2005**, *86*, 103512.

[43] K. Müller, W. Bär, K. Henkel, A. Jahnke, C. Schwiertz, D. Schmeißer, *TM* **2003**, *70*, 565.

[44] E. W. Paul, A. J. Ricco; M. S. Wrighton, J. Phys. Chem. 1985, 89, 1441.

[45] R. B. Dabke, G. D. Singh, A. Dhanabalan, R. Lal, R. Q. Contractor, *Anal. Chem*. **1997**, *69*, 724.

[46] Q. Pei, G. Yu, C. Zhang, Y. Yang and A. J. Heeger, *Science* **1995,** *269*, 1086.

[47] L. Edman, J. Swensen, D. Moses, A. J. Heeger, *Appl. Phys. Lett.* **2004**, *84* (19), 3774.

[48] J. Leger, M. Berggren, S. Carter, *Ionic Carriers in Organic Electronic Materials and Devices*, CRC Press **2010**.

[49] G. Bäcklund, H. G. O. Sandberg, R. Österbacka, H. Stubb, *Appl. Phys. Lett.* **2004**, *85* (17),3887.

[50] D. B. A. Rep, A. F. Morpurgo, W. G. Sloof, T. M. Klapwijk, *Appl. Phys. Lett.* **2002**, *93* (4), 2082.

[51] D. B. A. Rep, A. F. Morpurgo, T. M. Klapwijk, *Organic Electronics* **2003**, 201.

[52] L. Bürgi, H. Sirringhaus, R. H. Friend, *Appl. Phys. Lett.* **2002**, *80* (16), 2913.

[53] A. Klug, M. Denk, T. Bauer, M. Sandholzer, U. Scherf, C. Slugovc, E. J. W. List, (submitted for publication).

[54] M. Egginger, M. Irimia-Vladu, R. Schwödiauer, A. Tanda, I. Frischauf, S. Bauer, N. S. Sariciftci, *Adv. Mater* **2008**, *20*, 1018.

[55] M. J. Panzer, C. D. Frisbie, *Adv. Mater.* **2008**, *20*, 3177.

[56] J. Lee, L. G. Kaake, J. H. Cho, X.-Y. Zhu, T. P. Lodge, C. D. Frisbie, *J. Phys. Chem. C*. **2009**, *113*, 8972.

[57] J. D. Yuen, A. S. Dhoot, E. B. Namdas, N. E. Coates, M. Heeney, I. McCulloch, D. Moses, A. J. Heeger, J. Am. Chem. Soc. **2007**, *129*, 14367.

[58] www.microchemicals.de

[59] H. Sirringhaus, T. Kawas, R.-H. Friend, T. Shimoda, M. Inbasekaran, W. Wu, E.-P. Woo, *Science* **2000**, *290*, 2123.

[60] D. Tobjörk, N. J. Kaihovirta, T. Mäkelä, F. S. Pettersson, R. Österbacka, *Org. Electron*. **2008**, *9*, 931.

[61] H. Klauk, *Organic electronics – Materials, Manufacturing, and Applications*, Wiley-VCH, Weinheim **2006**.

[62] Z. Bao, *Nat. Mat.* **2004**, *3*, 137.

[63] S. Gamerith, A. Klug, H. Scheiber, U. Scherf, E. Moderegger, E. J W. List, *Adv. Funct. Mater.* **2007**, *17*, 3111.

[64] S. Magdassi, *The Chemistry of Inkjet Inks*, World Scientific Publishing, Singapore **2010.**

[65] www.cabot-corp.com/wcm/download/en-us/nb/CCI%20Data%20Sheet%207-12-07_PEM.pdf

[66] A. Blümel, A. Klug, S. Eder, U. Scherf, E. Moderegger, E. J. W. List, *Org. Electron.* **2007**, *8*, 389.

[67] www.plextronics.com

[68] H. Sirringhaus, N. Tessler, R. H. Friend, *Science* **1998**, *280*, 1741.

[69] H. Sirringhaus, P. J. Brown, R. H. Friend, M. M. Nielsen, K. Bechgaard, B. M. W. Langeveld-Voss, A. J. H. Spiering, R. A. J. Janssen, E. W. Meijer, P. Herwig, D. M. de Leeuw, *Nature* **1999***, 401*, 658.

[70] B. A. Mattis, P. C. Chang, V. Subramanian, *Mater. Res. Soc. Symp. Proc*. **2003**, 771.

[71] K. Kanai, T. Miyazaki, H. Suzuki, M. Inaba, Y. Ouchi, K. Seki, *Phys. Chem. Chem. Phys.* **2010**, *12*, 273.

[72] Mowiol PVA datasheet, Clariant GmbH, Sulzbach, Germany **1999**.

[73] www.spectrapor.com

[74] Fumio Sanda, *Department of Polymer Chemistry*, Kyoto University.

[75] K. Tamura, M. Shiotsuki, N. Kobayashi, T. Masuda, F. Sanda, *Polymer* **2009**, *50*, 4479.

[76] T. Sasano, K. Tamura, M. Shiotsuki, F. Sanda, T. Masuda, *Polymer Preprints* **2009,** *58* (2).

[77] T. Ashimine, T. Yasuda, M. Saito, H. Nakamura, T. Tsutsui, *Jap. J. Appl. Phys.* **2008**, *47*, 1760.

[78] K. Tamura, M. Shiotsuki, N. Kobayashi, T. Masuda, F. Sanda, *J. Polym. Sci., Part A: Polym. Chem.* **2009**, *47*, 3506.

[79] Klaus Müllen, *Max Planck Institute for Polymer Research*, Mainz, Germany.

[80] T. Qin, W. Wiedemair, S. Nau, S. Schuh, R. Trattnig, S. Sax, S. Winkler, A.Vollmer, N. Koch, M. Baumgarten, E.J.W. List, K. Müllen, "*Shape Persistent Dendrimers for the Application in Blue Light Emitting Diodes*", (submitted for publication).

[81] E. M. Eyring, D. P. Cobranchi, B. A. Garland, A. Gerhard, A. M. Highley, Yo-Hsin Huang, G. Konya, S. Petrucci, R. van Eldik, J. S. Bradshaw, R. M. Izatt, *Pure & Appl. Chem*. **1993**, *65*,451.

[82] E. Breitmaier, G. Jung, *Organische Chemie*, 5. Auflage, Georg Thieme Verlag, Stuttgart **2005**.

[83] L. Edman, M. Pauchard, D. Moses, A. J. Heeger*, J. Appl. Phys*. **2004**, *95* (8), 4356.

[84] C. Goldmann, C. Krellner, K. P., Pernstich, S. Haas, D. J. Gundlach, B. Batlogg, *J. Appl. Phys*. **2006**, *99*, 034507 and references therein.

[85] A. Schoonveld, „*Transistors based on ordered organic semiconducors*", PhD Thesis, University of Groningen, Netherlands **1999**.

[86] N. Schüwer, H.-A. Klok, *Adv. Mater*. **2010**, *22*, 3251.

[87] A. Klug, K. Schmoltner, E. J. List, *Proc. of SPIE* **2010**, *7779*, 77790G.

[88] Prof. Christoph Slugovc, *Institute for Chemistry and Technology of Materials*, Graz University of Technology Austria (ICTM).

[89] Agilent E4980 Manuel, 7th Edition.

[90] A. Facchetti, M.-H. Yoon, T. J. Marks, *Adv. Mater.* **2005**, *17*, 1705.

[91] X. Peng, G. Horowitz, D. Fichou, F. Garnier, *Appl. Phys. Lett*. **1990**, *57*, 2013.

[92] www.dupontteijinfilms.com

[93] D. J. Durian, C. Frank, *Phys. Rev. Lett.* **1987**, *59*, 555.

[94] http://www.teijindupontfilms.jp/english/pdf/teonex_q65fa.pdf

[95] A. Meingast, „*Development and Optimization of an Lithographic and Interface Related Process for Organic Field-Effect Transitors*“, Diploma Thesis, Graz University of Technology **2009**.